Zinc-iodide redox flow battery for next generation of solar energy storage

Monalisa Chakraborty

Tesi doctoral

Programa de doctorat en Ciència de Materials

Directors: Dra. Teresa Andreu Arbella, Dr. Sebastián Murcia López

Tutor: Prof. Jordi Arbiol

Departament de Química

Facultat de Ciències

2022

UAB

Universitat Autònoma
de Barcelona

Memòria presentada per aspirar al Grau de Doctor per

Monalisa Chakraborty

Vist i plau

Dra. Teresa Andreu Arbella   Dr. Sebastián Murcia López   Prof. Jordi Arbiol
(Directora)   (Director)   (Tutor)

Barcelona, September 2022

la **Dra. Teresa Andreu Arbella**, Professora Lectora del Departament de Ciència de Materials i Química Física de la Universitat de Barcelona,

El **Dr. Sebastián Murcia López**, Investigador consolidado, del Institut de Recerca en Energia de Catalunya,

i el **Dr. Jordi Arbiol Cobos**, Professor ICREA de Institut Català de Nanociència i Nanotecnologia,

CERTIFIQUEN:

Que **Monalisa Chakraborty** ha realitzat sota la seva direcció el treball d'investigació que s'exposa a la memòria titulada "Zinc-iodide redox flow battery for next generation of solar energy storage" per optar al grau de Doctor per la Universitat Autònoma de Barcelona.

Que el disseny dels experiments, síntesi de mostres, llur caracterització, l'anàlisi dels resultats, la redacció dels articles i d'aquesta memòria són fruit del treball d'investigació realitzat per **Monalisa Chakraborty**.

I perquè així consti, signen el present certificat,

Dra. Teresa Andreu Arbella   Dr. Sebastián Murcia López   Prof. Jordi Arbiol

Barcelona, September 2022

"Education is the most powerful weapon which you can use to change the World."

— Nelson Mandela, Nobel Prize in Chemistry 1993

"Without the love of research, mere knowledge and intelligence cannot make a scientist."

— Irène Joliot-Curie, Nobel Peace Prize 1935

"All our dreams can come true if we have the courage to pursue them."

— Walt Disney

I dedicate this thesis to my Lt. maternal and paternal Grandparents

Acknowledgments

There is a saying that I heard in my childhood from my Lt. Grandmother and my mother: ¨Education is the most valuable accessory that a person could wear throughout his/her life¨. The motivation to pursue doctoral research and become a Scientist was a dream, that I had seen several years back when I was finishing my Bachelor´s degree in India. Today with the completion of this thesis, I could say, yes, the dream came true. Being an instrumentation engineer by training, it was not an easy decision to change track and pursue research in applied chemistry. I could still remember those hard days and the struggle of learning Materials science, Physical chemistry in the first semester of my Master´s degree in Germany. I thank the Almighty for His great support during this whole journey of learning new things, despite several challenges, days after days with failed experiments in the lab, the courage of taking those challenges never stopped. And, when I overcome those, the satisfaction was indescribable. I want to thank all without whom I could not be able to reach my goals and might not have completed this doctoral thesis.

I would like to express sincere gratitude towards my thesis directors, Dra. Teresa Andreu and Dr. Sebastián Murcia López for welcoming me as their doctoral student, offering me this great opportunity, and especially, giving me enough freedom of scientific thinking, proposing new research ideas, and applying them. Teresa, words would not be enough to express how much impressed I am with your scientific insights and passion for science, moreover, you are an extremely nice person with positive thoughts. Sebastian, I am highly grateful to you. I could not even imagine my whole doctoral journey without you. This thesis is half yours. Besides being a wonderful scientist, you are a person of kind heart, and most especially, you had always welcomed my daily lab-related problems even though you were under an extreme workload. I owe a great debt to you both.

I would like to thank the head of the ESEH group, Prof. Joan Ramon Morante for giving me the opportunity to work and contribute to the group. I also want to say thank you to Prof. Jordi Arbiol, for becoming the tutor of my thesis.

I sincerely thank Prof. Jordi Martorell and Dr. Carles Ros from Organic Nanostructured Photovoltaics group at ICFO, Castelldefels for hosting me as a visiting researcher. Francisco, many thanks for the amazing collaboration with you. You are such a down-to-earth person and of course, a workaholic researcher! My thank goes to my collaborators: Ben, Dr. Maxim Guc, and Mohamed, for the collaborations and I am happy that these all are coming out as publications!

To my ex and current colleagues and friends of the ESEH group: Nina, Jordi J., Hemesh, Carles, Javier, Antonio, Kele, Kuba, Felix, Jordi H., José Miguel, Andreina, Viktoriia, Tandava, Marcelo, Marisa, Elias, Prakasha, Jordi G., Elena, Maximiliano, Ivan, Andrés, Paolo, Ting, Martí, it was a pleasure to work with you and, of course, to share the beautiful lunch hours, coffee breaks and fun-filled weekends. Andrés and Marisa, thank you for all the mental support I received from you both during my

stressful days. Many thanks to Viktoriia and Martí for helping me with the thesis book format. Martí, you are really a trouble-solver in our ESEH lab, thank you again for all the help you provided during the experiments.

To other colleagues at IREC, special thanks to Dra. Diouldé, Dr. Marc N., and Dr. Albert, for the great advice and support in the scientific instruments. Francesc Torregrosa, for helping me with all the bureaucratic issues.

I want to thank the DOC-FAM team, all the 21 fellows. Thank you for the beautiful moments we shared although it would be much more unless there was no covid.

My thank goes to the Indians at IREC group, for all the lovely meet-ups, food, and fun-filled volleys. My one and only Bengalee friend in Barcelona, Sushmita, I spent amazing moments with you and your family! Thanks to my good friend, Swapneel for the joyous moments I shared with you along with Kunal.

Kunal, *mere yaar*, thanks for being my closest friend, and one of my motivators all the time. I really enjoyed all those brainstorming scientific discussions and would like to continue afterward. You´re a highly motivated scientist, I must say.

My `Badalona and UPC family´: Zacharie, Lovely, Sergio, Marcel, Edgardo, Darek, and Isabella – thanks for the love and support, the tasty foods, beautiful beach hangouts, and karaoke nights in Badalona. You, all are amazing! I feel lucky to be one of the members of this family. Also, you, people are amazing cooks! Zacharie and Lovely, thank you for the affection you bestowed upon me.

A big shoutout to my friends from `Group of masizz´. Thanks for the mental support you all gave me throughout my journey in Europe and especially during extreme covid situations. The funny jokes you shared in the group, used to make me laugh on my stressful days!

I would like to express my gratitude to my beautiful family, for their unconditional love and support and for the trust that you put in me. To my mother, who does not get tired of speaking continuously over the phone and asking me the same question every day: what are you going to eat tonight? Thank you, Ma for the care! To my father, who is my role model, a highly skilled Engineer, and a wonderful, kind-hearted person with never failing attitude. To my sister, my best friend as well as the person I can rely on blindly. Without your constant support and encouragement, it was just not possible to finish two degrees in Europe. I owe a great debt to you. I hope one day I can make you proud. To my brother-in-law, a genius and extremely talented person I came across in my life so far! Thank you for the mental and financial support you and my sister provided me in my tough times. Lastly, the youngest member of my family: my little nephew, Atri, my *energy booster*, thank you for all the childish, stress-free moments I shared with you.

Lastly, I would like to acknowledge the Autonomous University of Barcelona for the academic support and tutoring in the framework of the doctorate programme in Materials Science.

Financial support

Index

Table of Contents

Preface

Abstract

The globally increasing demand of renewable energy sources into the electricity grid created the need to introduce large-scale energy storage systems (ESS) due to its intermittent nature. Thanks to the unique features of redox flow batteries (RFBs) of decoupling energy and power independently, theyare considered as an excellent option to be employed in medium-to-large-scale storage applications. Among the latest advances in alternative RFB technologies, zinc-iodide redox flow battery (ZIFB) exhibits a great potential for high energy density large-scale ESS to which the presence of highly abundant zinc added another valuable point towards cost optimisation. However, their practical use is still limited by poor cyclability, low current density, and capacity loss, mainly due to irreversible zinc plating/stripping, water migration during cycling, slow kinetics of the redox reactions, and iodine (I_2) precipitation.

In this context, the aim of this thesis is to design a ZIFB with the improvement on the anode and electrolyte chemistry, focusing mainly on lower current densities, suitable for the matching with the photovoltaic system thereafter. To achieve these objectives, the thesis is structured in seven main chapters. **Chapter 1** presents the general context, background and motivation of the research on RFB, basic introduction of RFBs, ZIFB and solar RFBs. **Chapter 2** describes the materials preparation, experimental set-up and methods applied in this thesis. The following chapters are focused on the main results obtained, which are divided into two parts. **Part I** is focused on the electrochemical performance improvements of ZIFB (**Chapters 3–5**). **Part II** (**Chapters 6** and **7**) is focused on the unbiased photocharge of RFBs, starting from vanadium redox flow battery (VRFB) to the ZIFB, optimised in **Part I**.

In **Chapter 3**, among exploration of different carbon-based anodes, graphite foil was found as the best optimised anode, exhibiting excellent battery overall efficiency (~80%) as a result of efficient Zn plating/stripping, to be used for further study in ZIFB. Our investigations stated that several factors greatly influence the efficient Zn metal plating/stripping, such as physical structure of anodes, electrolyte wettability, graphitic nature and electrical conductivity.

Chapter 4 and **5**, are devoted to the improvement of the electrolyte chemistry. A major issue in RFB cycling is water migration between half-cell electrolytes, which was resolved in **Chapter 4**. The experimental results of our proposed model of balancing the molar concentrations of electrolytes showed that ZIFB cycled with this tuned electrolyte suppressed 1/3 of water migration from catholyte to anolyte, as well as, showed an excellent discharge capacity and lowest cell ohmic resistance. Migration of large hydrated Zn^{2+} ions can be the root cause of water shuttle, which was suppressed (~50%) with the tuned electrolyte. **Chapter 5** focuses on the enhancing the cycle life of ZIFB by the introduction of NaCl as a supporting electrolyte. The presence of Cl^- ions boosted the ZIFB performance with 100 stable cycles and 77% capacity retention. Distinguishable improvements in the redox

reversibility of Zn/Zn^{2+} and I_3^-/I^- reactions have been achieved. From the speciation analyses, formation of the soluble $ZnCl_4$ compound is the key factor for the improvement of Zn/Zn^{2+} redox reversibility, which stabilised Zn^{2+} ions in the solution, facilitated a uniform and densely packed Zn metal deposition on the anode. At the cathode, the formation of soluble I_2Cl^- complex stabilised the battery by avoiding I_2 precipitation, participation of Na^+ and K^+ as main charge balance carriers passing through Nafion cation exchange membrane (CEM), restricts Zn^{2+} migration, thus, blocking the electrolyte crossover.

Part II (**Chapters 6** and **7**), is dedicated to the device-level study to reach unbiased photocharge of solar RFBs. **Chapter 6** is focused on the integration of the two most investigated systems: $Cu(In,Ga)Se_2$ photovoltaics (PV) and VRFB in a straightforward approach. Full unbiased photocharge (1 Sun condition) achieved high energy efficiency (77%), solar-to-charge (7.5%), and overall round-trip energy conversion efficiency (5%). Besides, evaluation on the influence of the PV operation region on the final efficiency of the solar VRFB is demonstrated. Taking into account the remaining yet important challenges from this above solar VRFB set-up, the integration was performed between the optimised ZIFB (from **Part I**) and an organic solar cell (OSC) made of environment-friendly photoabsorber materials in **Chapter 7**. Thanks to the stable charging voltage (~1.3 V) of OSC powered ZIFB unlike VRFB (charge voltage range: 1.4–1.7 V), and due to the intrinsic property of the photoabsorber materials with a tendency of increasing photocurrent with longer illumination hours, the ZIFB charged up to 22% solely powered by OSC.

Resumen

La creciente demanda mundial de fuentes de energía renovables en la red eléctrica ha creado la necesidad de introducir sistemas de almacenamiento de energía a gran escala (ESS) debido a su naturaleza intermitente. Gracias a las características únicas de las baterías de flujo redox (RFB) de desacoplamiento de energía y potencia, se consideran como la mejor opción para ser empleadas en aplicaciones de almacenamiento a mediana y gran escala. Entre los últimos avances en tecnologías alternativas de RFB, la batería de flujo redox de zinc-yoduro (ZIFB) exhibe un gran potencial para EES a gran escala con alta densidad de energía, a la que la presencia de zinc altamente abundante agrega otro punto valioso hacia la optimización de costes. Sin embargo, su uso práctico todavía está limitado por la mala ciclabilidad, la baja densidad de corriente y la pérdida de capacidad, principalmente debido a la deposición/redisolución irreversible de zinc, la migración de agua durante el ciclado, la cinética lenta de las reacciones redox y la precipitación de yodo (I_2).

En este contexto, el objetivo de esta tesis es diseñar una ZIFB con la mejora de la química del ánodo y el electrolito, centrándose principalmente en densidades de corriente más bajas, adecuadas para el acoplamiento con el sistema fotovoltaico posteriormente. Para lograr estos objetivos, la tesis se estructura en siete capítulos principales. El **Capítulo 1** presenta el contexto general, los antecedentes y la motivación de la investigación sobre RFB, la introducción básica de RFB, ZIFB y RFB solares. El **Capítulo 2** describe las preparaciones de los materiales, la configuración experimental y los métodos aplicados en esta tesis. Los siguientes capítulos se centran en los principales resultados obtenidos, que se dividen en dos partes. La **Parte I** se centra en las mejoras del rendimiento electroquímico de ZIFB (**Capítulos 3-5**). La **Parte II** (**Capítulos 6** y **7**) se centra en la fotocarga de las RFB, desde la batería de flujo redox de vanadio (VRFB) hasta la ZIFB, optimizada en la **Parte I.** En el **Capítulo 3**, donde se exploran diferentes ánodos de base carbonosa, se encontró la lámina de grafito como el ánodo mejor optimizado, exhibiendo una excelente eficiencia general de la batería (~80%) como resultado de una eficiente deposición/redisolución de Zn, que se utiliza para los estudios adicionales en ZIFB. Nuestras investigaciones mostraron que varios factores influyen en gran medida en la eficiente deposición/redisolución del Zn metálico, como la estructura física de los ánodos, la humectabilidad por los electrolitos, la naturaleza grafítica y la conductividad eléctrica. Los **Capítulos 4** y **5,** están dedicados a la mejora de los electrolitos. Un problema importante durante el ciclado de la RFB es la migración de agua entre electrolitos de cada semicelda, que se resolvió en el **Capítulo 4**. Los resultados experimentales de nuestro modelo propuesto de equilibrar las concentraciones molares de electrolitos, mostraron que el ciclado de la ZIFB con este electrolito ajustado suprimió en 1/3 la migración de agua de catolito a anolito, mostrando una excelente capacidad de descarga y menor resistencia óhmica de la celda. El transporte de los iones y agua revelaron que la migración de grandes iones

hidratados Zn^{2+} puede ser la causa principal del transporte de agua, que se suprimió (~50%) con el electrolito ajustado. El **Capítulo 5** se centra en la mejora de la vida útil del ciclo de ZIFB mediante la introducción de NaCl como electrolito soporte adicional. La presencia de iones Cl^- mejoró notablemente el rendimiento de la ZIFB con 100 ciclos estables y una capacidad de retención del 77%. Se han logrado mejoras en la reversibilidad redox de las reacciones Zn/Zn^{2+} e I_3^-/I^-. A partir de los análisis de especiación, la formación del compuesto soluble $ZnCl_4$ es el factor clave para la mejora de la reversibilidad redox Zn/Zn^{2+}, que estabilizó los iones Zn^{2+} en la solución, y facilitó una deposición de metal Zn uniforme y densamente empaquetada en el ánodo. En el cátodo, la formación del complejo I_2Cl^- soluble estabilizó la batería evitando la precipitación de I_2, la participación de Na^+ y K^+ como portadores principales del balance de carga que pasan a través de la membrana de intercambio catiónico de Nafion (CEM), restringiendo la migración de Zn^{2+}, bloqueando así el cruce de electrolitos.

La **Parte II** (**Capítulos 6** y **7**) está dedicada al estudio a nivel de dispositivo para alcanzar la fotocarga de las RFB solares. El **Capítulo 6** se centra en la integración de los dos sistemas más investigados: $Cu(In,Ga)Se_2$ fotovoltaico (PV) y VRFB en un enfoque directo. Se ha logrado la fotocarga completa (condición de 1 sol), lo que resulta en alta eficiencia de energía (77%), energía solar a carga (7.5%) y eficiencia global de conversión de energía (5%). Además, se demuestra la evaluación de la influencia de la región de operación fotovoltaica en la eficiencia final de la VRFB solar. Teniendo en cuenta los retos restantes pero importantes de la configuración anterior de VRFB solar, la integración se realizó entre la ZIFB optimizada (de la **Parte I**) y una celda solar orgánica (OSC) hecha de materiales fotoabsorbentes respetuosos con el medio ambiente, en el **Capítulo 7**. Gracias al voltaje de carga estable (~1.3 V) de la ZIFB alimentada por OSC, a diferencia de VRFB (rango de voltaje de carga: 1.4–1.7 V), y a la propiedad intrínseca de los materiales fotoabsorbentes con tendencia a aumentar la fotocorriente con horas de iluminación más largas, el ZIFB se cargó hasta un 22% alimentado únicamente por OSC.

Resum

La creixent demanda mundial de fonts d'energia renovables a la xarxa elèctrica va crear la necessitat d'introduir sistemes d'emmagatzematge d'energia a gran escala (ESS) atesa la seva naturalesa intermitent. Gràcies a les característiques úniques de les bateries de flux redox (RFB) de desacoblament d'energia i potència de forma independent, es consideren com la millor opció per ser emprades en aplicacions d'emmagatzematge a mitjana i gran escala. Entre els últims avenços en tecnologies alternatives de RFB, la bateria de flux redox de zinc-iodur (ZIFB) exhibeix un gran potencial per a EES a gran escala d'alta densitat d'energia a la qual la presència de zinc altament abundant agrega un altre punt valuós cap a l'optimització de costos. No obstant això, el seu ús pràctic encara està limitat per la mala ciclabilitat, la baixa densitat de corrent i la pèrdua de capacitat, principalment a causa de la deposició/redisolució irreversible de zinc, la migració d'aigua durant el ciclat, la cinètica lenta de les reaccions redox i la precipitació de iode (I_2).

En aquest context, l' objectiu d' aquesta tesi és dissenyar una ZIFB amb la millora de la química de l' ànode i l' electrolit, centrant-se principalment en densitats de corrent més baixes, adequades per a l' acoblament amb el sistema fotovoltaic posteriorment. Per assolir aquests objectius, la tesi s'estructura en set capítols principals. El **Capítol 1** presenta el context general, els antecedents i la motivació de la recerca sobre RFB, la introducció bàsica de RFB, ZIFB i RFB solars. El **Capítol 2** descriu les preparacions dels materials, la configuració experimental i els mètodes aplicats en aquesta tesi. Els capítols següents se centren en els principals resultats obtinguts en aquesta tesi, que es divideixen en dues parts. La **Part I** se centra en les millores del rendiment electroquímic de ZIFB (**Capítols 3-5**). La **Part II** (**Capítols 6** i **7**) se centra en la fotocàrrega de les RFB, des de la bateria de flux redox de vanadi (VRFB) fins a la ZIFB, optimitzada a la **Part I**.

En el **Capítol 3**, on s'exploren diferents ànodes de base carbonosa, es va trobar la làmina de grafit com l'ànode més ben optimitzat, exhibint una excel·lent eficiència general de la bateria (~ 80%) com a resultat d'una eficient deposició/redisolució de Zn, que s'utilitzarà per a estudis addicionals en ZIFB. Les nostres investigacions van mostrar que diversos factors influeixen en gran mesura en l'eficient deposició/redisolució del Zn metàl·lic, com l'estructura física dels ànodes, la humectabilitat pels electrolits, la naturalesa grafítica i la conductivitat elèctrica.

Els **Capítols 4** i **5**, estan dedicats a la millora dels electrolits. Un problema important durant el ciclat de la RFB és la migració d'aigua entre electrolits de cada semicel·la, que es va resoldre en el **Capítol 4**. Els resultats experimentals del nostre model proposat d'equilibrar les concentracions molars d'electrolits van mostrar que el ciclat de la ZIFB amb aquest electrolit ajustat va suprimir en 1/3 la migració d'aigua de catolit a anolit, així com va mostrar una excel·lent capacitat de descàrrega i menor resistència òhmica de la cel·la. El transport dels ions i aigua van mostrar que la migració de grans ions hidratats Zn^{2+} pot ser la causa principal del transport d'aigua,

que es va suprimir (50%) amb l'electrolit ajustat. El **Capítol 5** se centra en la millora de la vida útil del cicle de ZIFB mitjançant la introducció de NaCl com a electrolit suport addicional. La presència d'ions Cl⁻ va millorar notablement el rendiment de la ZIFB amb 100 cicles estables i una capacitat de retenció del 77%. S'han aconseguit millores en la reversibilitat redox de les reaccions Zn/Zn^{2+} i I_3^-/I^-. A partir de les anàlisis d'especiació, la formació del compost soluble $ZnCl_4$ és el factor clau per a la millora de la reversibilitat redox Zn/Zn^{2+}, que va estabilitzar els ions Zn^{2+} en la solució, va facilitar una deposició de metall Zn uniforme i densament empaquetada a l'ànode. Al càtode, la formació del complex I_2Cl^- soluble va estabilitzar la bateria evitant la precipitació d'I2, la participació de Na^+ i K^+ com a portadors principals del balanç de càrrega que passen a través de la membrana d'intercanvi catiònic de Nafion (CEM), restringint la migració de Zn^{2+}, bloquejant així l'encreuament d'electrolits.

La **Part II** (**Capítols 6** i **7**) està dedicada a l'estudi a nivell de dispositiu per assolir la fotocàrrega de les RFB solars. El **Capítol 6** se centra en la integració dels dos sistemes més investigats: $Cu(In,Ga)Se_2$ fotovoltaic (PV) i VRFB en un enfocament directe. S'ha aconseguit la fotocàrrega completa (5.0%), la qual cosa resulta en alta eficiència d'energia (77%), energia solar a càrrega (7.5%) i eficiència global de conversió d'energia (5.0%). A més, es demostra l'avaluació de la influència de la regió d'operació fotovoltaica en l'eficiència final de la VRFB solar. Tenint en compte els reptes restants però importants de la configuració anterior de VRFB solar, la integració es va realitzar entre la ZIFB optimitzada (de la **Part I**) i una cel·la solar orgànica (OSC) feta de materials fotoabsorbents respectuosos amb el medi ambient al **Capítol 7**. Gràcies al voltatge de càrrega estable (~ 1.3 V) de la ZIFB alimentada per OSC, a diferència de VRFB (rang de voltatge de càrrega: 1.4 – 1.7 V), i a la propietat intrínseca dels materials fotoabsorbents amb tendència a augmentar la fotocorrent amb hores d'il·luminació més llargues, el ZIFB es va carregar fins a un 22% alimentat únicament per OSC.

List of abbreviations

3CM	3-series cell module
4CM	4-series cell module
C paper	Carbon paper
CE	Coulombic efficiency
CEM	Cation exchange membrane
CIGS	Copper(Indium, Galium)Selenide
CV	Cyclic voltammetry
DSSC	Dye-sensitised solar cell
EDX	Energy dispersive X-ray spectroscopy
EE	Energy efficiency
EIS	Electrochemical impedance spectroscopy
EOD	Electro-osmotic drag
ESS	Energy storage system
FE-SEM	Field emission scanning electron microscope
FF	Fill factor
FTO	Fluorinated tin oxide
FWHM	Full-width-at-half-maximum
G foil	Graphite foil
GCE	Glassy carbon electrode
GF	Graphite felt
HER	Hydrogen evolution reaction
ICP-OES	Inductively coupled plasma optical emission spectroscopy
LSV	Linear scan voltammetry
MOF	Metal-organic framework
MSA	Methanesulfonic acid
OCV	Open circuit voltage
OER	Oxygen evolution reaction
OSC	Organic solar cell
PEC	Photoelectrochemical
PEIS	Potentiostatic electrochemical impedance spectroscopy
PV	Photovoltaic
RFB	Redox flow battery
SEM	Scanning electron microscopy
SHE	Standard hydrogen electrode
SOC	State-of-charge
SRFB	Solar redox flow battery
SZIFB	Solar zinc iodide flow battery

VE	Voltage efficiency
VRFB	Vanadium redox flow battery
XRD	X-ray diffraction
ZIFB	Zinc iodide flow battery

Chapter 1

Introduction

Ion exchange membrane

Redox flow battery

1
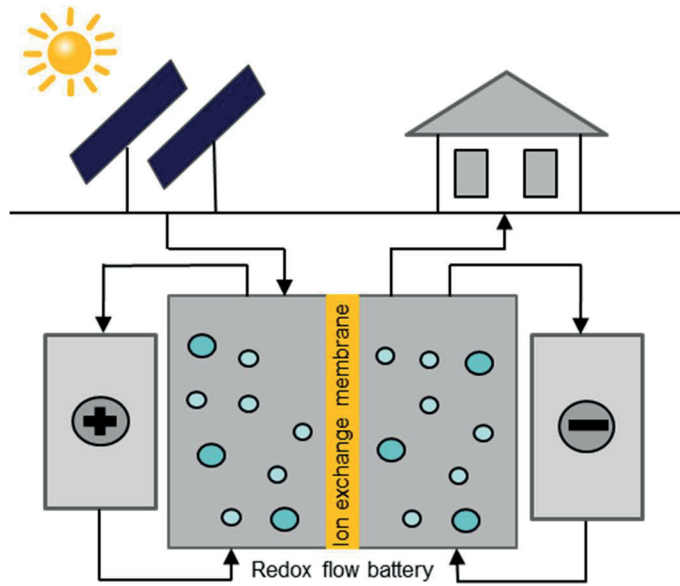
1.1 Research background and motivation

The current scenario of energy transition from fossil fuels to clean, renewable energies, is an attempt to confront climate change. The rapidly increasing global demand for electricity generation is to be doubled by 2050.[1] Despite the falling economies due to the effects Covid-19 pandemic, renewable energy sources such as solar and wind continued to grow rapidly and set a new record for global renewable generation capacity of 3064 GW at the end of 2021 (**figure 1.1**).[1,2] With the increase in new capacity in previous years, total global solar capacity has now outgrown wind energy capacity.[2] Although blooming but intermittent nature of solar energy requires stationary grid-scale energy storage systems for effective use of this sustainably generated energy.[3] Conventional rechargeable batteries offer a simple and efficient way to store electricity. However, the development to date has mostly emphasised on transportation systems and portable electronics, whereas metrics related to size and volume are less critical for grid-scale storage than in portable or transportation applications. Large-scale grid storage requires long-life, low-cost batteries, considering both cyclability, calendar life, round-trip efficiency and the ability to respond rapidly to changes in load or input.
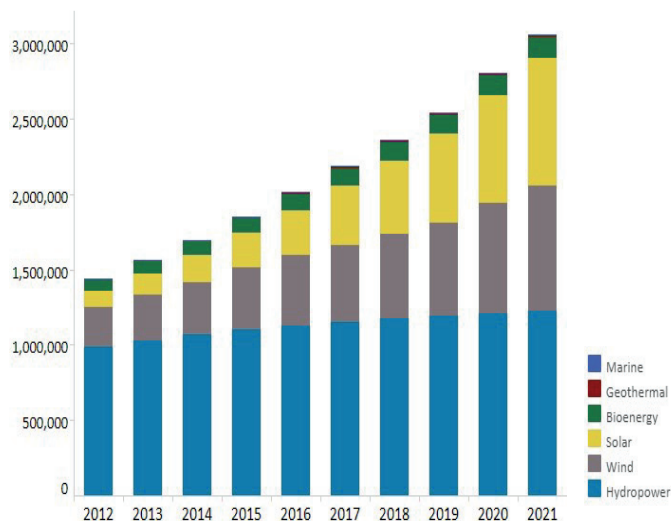
Figure 1.1. Renewable power capacity growth, data reported by International Renewable Energy Agency on April 2022.[2]

1.1.1 Redox flow battery (RFB): a promising choice for large-scale ESS

Among various energy storage technologies, redox flow batteries (RFBs) claim major promise to fulfil many of those above-mentioned (in **section 1.1.1**) requirements for large-scale grid storage system.[4] A RFB is an electrochemical energy storage device, which exploits redox processes of active species in solution in fluid form, stored in external tanks and introduced into the flow cell by pumping, where the electrochemical redox reactions take place.[5] **Figure 1.2** shows the power vs. duration diagram for different energy storage systems. Due to the independent nature of upscaling power and capacity, RFBs can provide a wide range of power and discharging times specially within the applications of grid support which has attracted interest in this topic to surge since the early 2000s, with gradually increasing numbers of highly cited publications (**figure 1.3**). These numbers of publications explain the several approaches focused on developing better RFBs. Besides, scalability, flexibility, high round-trip efficiency, long durability and faster response time are among the appealing features of RFB.[6,7]
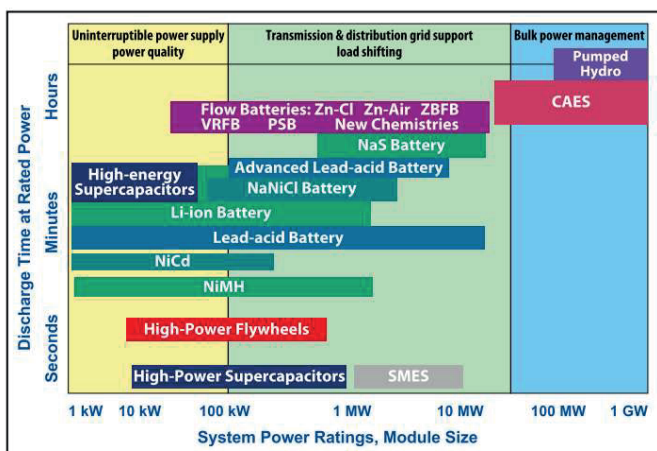
Figure 1.2. Positioning of various energy storage technologies in terms of power and duration.[8]

4
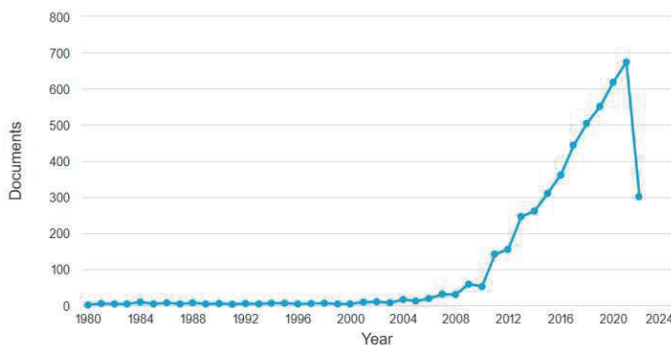
Figure 1.3. The number of publications in redox flow batteries research published per year. This Scopus search was carried out on the 19th May 2022.

Advantages and disadvantages of RFB with respect to other battery technologies

The separation of power and energy independently is the unique distinction of RFBs compared to the other electrochemical storage technologies. The energy is stored in the volume of the electrolyte, which can easily be decoupled from several KWh to 10´s of MWh by upscaling the tank size and electrolyte concentration, while power is a matter of the electrode size.[9] This contrasts with conventional batteries in which the energy is directly stored in the electrodes. RFBs are capable of rapid response that allows them to span from power quality to energy management services. Moreover, rapid refuelling is possible by electrolyte exchange when needed, and they require low maintenance. In addition, RFBs are not exposed to thermal runaway problem, unlike lithium-based batteries.[6,9,10]

The volumetric energy densities of RFBs are comparatively lower (15-25 Wh·L^{-1}) than other technologies such as Li-ion (250–650 Wh·L^{-1}), due to the solubility limitation of redox-active species and the stability potential window of the solvent, specially for the aqueous system which is constrained by hydrogen evolution (HER) and oxygen evolution reactions (OER).[11] This drawback makes RFBs unsuitable for mobile applications at present, but are good candidates for static or large-scale applications where metrics related to energy density are not that crucial.

1.2 The redox flow battery

1.2.1 General principles of redox flow batteries

Figure 1.4 depicts the typical working principle of single-cell RFB. The main components are an electrochemical cell and two reservoirs. The cell contains two electrodes, anode and cathode, and a separator. The electrolytes containing the redox-active species from the reservoirs are circulated between anode and cathode compartments, where the electrochemical reactions take place. During charging, positive electrolyte (catholyte) is oxidised and releases electron to the external circuit, which is being accepted by the negative electrolyte (anolyte) via the reduction

1

reaction, while the reverse process occurs in discharge. The general reactions can be written as:[9]

For the anode:

$$A^{n+} + xe^- \rightarrow A^{(n-x)+} \quad \text{charge}$$

$$A^{(n-x)+} \rightarrow A^{n+} + xe^- \quad \text{discharge} \qquad (1.1)$$

For the cathode:

$$B^{m+} - ye^- \rightarrow B^{(m+y)+} \quad \text{charge}$$

$$B^{(m+y)+} \rightarrow B^{m+} - ye^- \quad \text{discharge} \qquad (1.2)$$
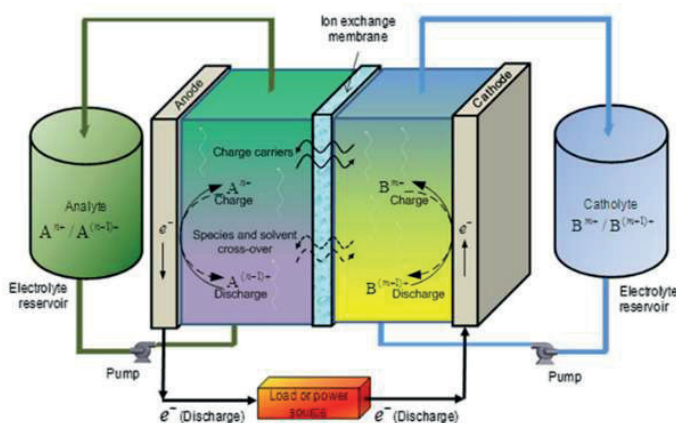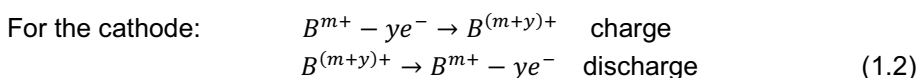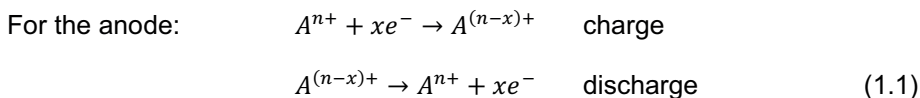
Figure 1.4. A schematic illustration of a redox flow battery.[9]

1.2.2   Evolution of RFB

Figure 1.5 represents a timeline of the development of flow batteries with various chemistries, aqueous, non-aqueous, hybrid and further development of solar RFBs. Early RFBs based on all-vanadium,[12] iron-chromium[13] and zinc-bromine[14] couples have been implemented commercially. During the 70s to 80s, there was an enormous effort in developing the redox flow battery technology. As a result, the National Aeronautics and Space Administration (NASA) invested in this technology. Fe/Cr RFBs were invented at the NASA Lewis Research Center in the 1970s.[15] Although promising several critical issues, including the poor electrochemical activity of the Cr^{2+}/Cr^{3+} redox couple, hydrogen evolution, a high working temperature and capacity decay by severe cross-contamination have hampered practical use[16]. RFBs using a Zn/Br couple were also first demonstrated in the 1970s.[17] Besides the formation of vigorous zinc dendrites, toxicity of bromine has hindered its penetration into the marketplace. Currently, the most widely studied aqueous RFB is the all-vanadium system (VRFB), developed in the 1980s by the group of M. Skyllas-Kazacos et al.[18]
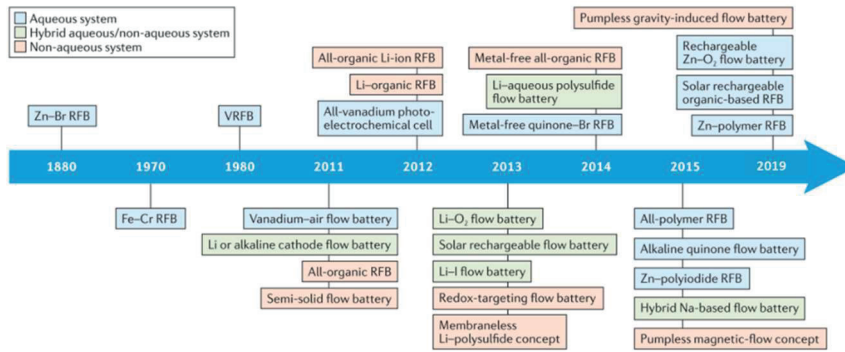
Figure 1.5. A timeline of the development of flow batteries.[16,19]

The selection of redox-active materials has an important role in the performance of the flow battery by influencing the reaction kinetics, viscosity of the electrolyte and the capacity and thus energy density of the system. Upon the recent development of RFBs, a wide range of metal-based redox couples dissolved in aqueous and non-aqueous electrolytes has been investigated. The non-aqueous electrolytes offer better electrochemical stability and a wider potential window[9] but by paying the price of higher viscosity as well as expensive electrolytes.[20] Aqueous electrolytes are widely used in RFB chemistries because of better safety, lower cost, and higher ionic conductivity. The most common inorganic (metal-based) redox pairs in aqueous media are summarised in **figure 1.6**. More recently, RFBs based on organic molecules have been reported[21–23] because of their low cost and high reversibility. However, the limited solubilies of active compounds and low cell voltage are the major drawbacks.[24] Thus, conventional RFBs based on inorganic redox couples are still much more promising than their organic counterparts.
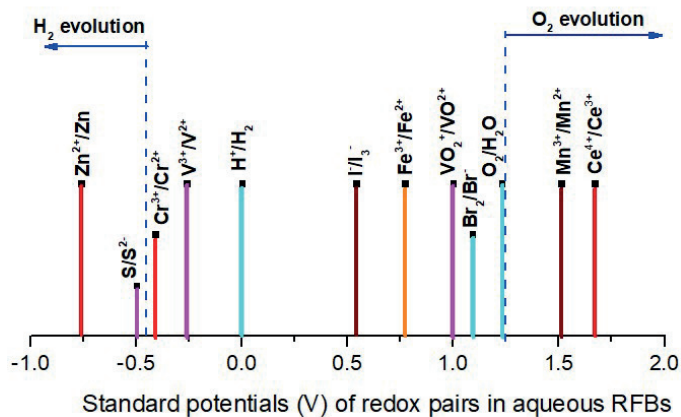
Figure 1.6. The standard redox potentials of various candidate redox pairs suitable for all-aqueous redox flow batteries.

1.3 Mostly investigated RFBs based on inorganic pairs

Concerning the major disadvantages of iron-chromium and zinc-bromine redox couples (as mentioned in **section 1.2.2**), sluggish reaction kinetics, poor electrochemical activity, severe cross-contamination, the all-vanadium RFB received great interest, being the most fruitfully commercialised.[9,12,25–28] The main benefit of vanadium chemistry over iron-chromium and zinc-bromide is to employ single metal ions of different oxidation states in both electrolytes, suppressing irreversible species crossover; hence, the cell capacity does not decrease with time, allowing for a longer lifespan.

All-vanadium

The all-vanadium system (**figure 1.7**) employs the V(II)/V(III) redox couple at the negative compartment and the V(IV)/V(V) at the positive, generally identified to exist in the form of VO^{2+} and VO_2^+ respectively. Electrochemical half-reactions of a VRFB are as follows:

Cathode:

$$VO_2^+ + 2H^+ + e^- \leftrightarrow VO^{2+} + H_2O \qquad \text{E}^0 = 1.0 \text{ V vs. SHE} \qquad (1.3)$$

Anode:

$$V^{2+} \leftrightarrow V^{3+} + e^- \qquad \text{E}^0 = 0.26 \text{ V vs. SHE} \qquad (1.4)$$

$$\leftarrow \text{charge} \quad \rightarrow \text{discharge}$$

The roundtrip energy efficiency was demonstrated to vary from 70% to 90% with an energy density of about 20-30 Wh·L^{-1}.[29]

While energy density is not a primary concern for stationary, grid-scale applications, nonetheless, the VRFB energy density is limited by the solubility of vanadium ions in the electrolyte solution[12] and precipitation can occur. The solubility limits depend upon both acid concentration and temperature.[30]
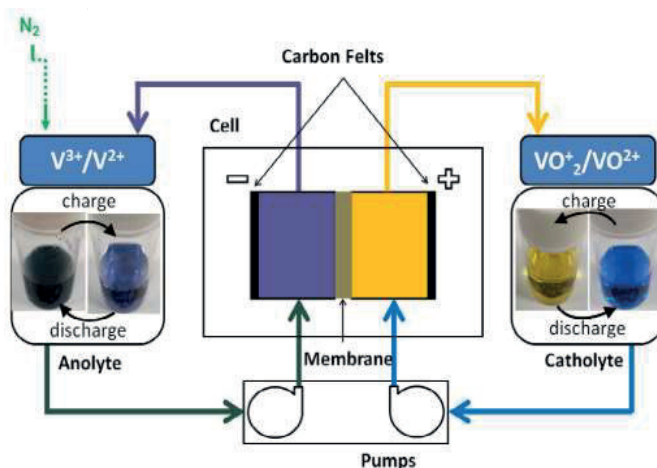
Figure 1.7. The schematic representation of VRFB illustrating the charge–discharge process.[31]

Alternatively, in the prospect of achieving high energy density and a cost-effective system, hybrid RFBs are well renowned. Unlike conventional RFBs where energy is stored in the electrolytes in the form of reduced and oxidised electroactive species, in hybrid RFBs, at least one of the electrode reactions involves a phase change (solid or gaseous).[24] Furthermore, hybrid RFBs are a group of inorganic-based RFBs which have appealing features of low-cost and high cell voltage.[32] Among them, zinc-based hybrid RFBs have long been the centre of attention in both primary and secondary batteries due to their attractive features like using earth-abundant zinc as active redox species, having higher energy content due to its large volumetric capacity (5.85 Ah·cm^{-3}) and negative electrode potentials in aqueous solutions (-0.76 V vs SHE in acidic and -1.26 V vs SHE in alkaline).[24]

1.3.1 Zinc-based hybrid RFBs

Aqueous Zn-based RFBs have become a promising ongoing research topic for large-scale energy storage applications in recent decades thanks to their negative electrode potential, faster kinetics, benign nature, high solubility and easy recyclability. The electro-plating and de-plating reaction of metallic Zn can take place in nearly acidic or alkaline media by the following reactions:[33]

$$Zn(s) \leftrightarrow Zn^{2+} + 2e^- \qquad \text{E}^0 = \text{-0.76 V vs. SHE} \qquad (1.5)$$

$$Zn(s) + 4OH^- \leftrightarrow Zn(OH)_4^{2-} + 2e^- \qquad \text{E}^0 = \text{-1.26 V vs. SHE} \qquad (1.6)$$

For most Zn-based hybrid RFBs, charge or electrical energy is stored mainly as the electrodeposit in the reduction process. Besides these above-mentioned reactions, the hydrogen evolution reaction (HER) is also thermodynamically favourable at the surface of Zn electrodes. However, a large hydrogen overpotential and suitable electrolyte composition of most Zn-based aqueous RFBs make the zinc deposition highly efficient (current efficiencies of over 90%). Hence, since the 1970s, various Zn-

1

based flow batteries have been proposed and developed by coupling with different positive electrode reactions to provide a desired voltage and capacity for renewable energy storage.[34] Among them, zinc-bromide, zinc-cerium, zinc-nickel, zinc-iron, and zinc-iodine chemistries have received more interest.

Zinc-Bromide

The zinc-bromide hybrid FB was developed by Exxon, Gould and NASA in the 1970s.[35] Earth-abundant metal, relatively high open-circuit voltage of 1.82 V (**Eq. 1.7**), and high theoretical energy density of 440 Wh·kg^{-1} are among the main advantages of Zn-Br RFBs. However, high self-discharge and the strongly corrosive bromine media in the positive electrolyte are the two main issues of this system.[36] Few works are reported by the addition of several complexing agents to the positive electrolyte to complex with bromine into an alternative phase with low vapour pressure. Thus, a electrolyte with complexing agents is required in a practical large-scale Zn-Br RFBs.[37]

$$Zn(s) + Br_2 \leftrightarrow Zn^{2+} + 2Br^- \qquad E^0 = 1.82 \text{ V vs. SHE} \qquad (1.7)$$
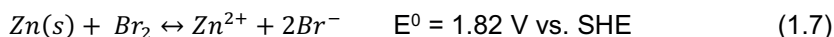
Zinc-Cerium

The zinc-cerium hybrid FB was first patented by Clarke et al.[38,39] in 2004 and has been developed by Plurion Inc.[6] This system uses a carbon polymer substrate and platinised carbon/titanium at the negative and positive electrodes respectively.[38,39] To slow down the oxygen evolution reaction and ensure reasonable solubilities for both the Zn (>2 M) and cerium species (c.a. 0.8 M), methanesulfonic acid (MSA) is used as a supporting electrolyte in the system. This system provides one of the highest OCV of 2.37 V (**Eq. 1.8**) in RFBs with aqueous electrolytes. The major limitation is the necessary use of high-cost platinum/titanium positive electrodes due to the corrosion of carbon-based electrodes in oxidative cerium electrolytes. Apart from that, high catalytic activity of platinum/titanium positive electrodes towards the oxygen evolution reaction, limits the performance of the battery.[36]

$$Zn(s) + 2Ce^{4+} \leftrightarrow Zn^{2+} + 2Ce^{3+} \qquad E^0 = 2.37 \text{ V vs. SHE} \qquad (1.8)$$

Zinc-Nickel

As an environmentally-friendly alternative to zinc-cadmium secondary batteries,[40] the concept of static zinc-nickel (Zn-Ni) batteries can be traced back to the 1900s. Porous matrix of zinc oxide was introduced as negative electrode and sintered nickel as positive electrode. The static Zn-Ni batteries provide a cell voltage of 1.7 V (**Eq. 1.9**). Afterwards, this chemistry with circulating electrolytes as Zn-Ni RFBs could mitigate some of the issues that arose with the static system including the zinc dendrite formation, shape change, and passivation.[24] A single-flow, membrane-less Zn-Ni RFB was designed later by borrowing the concept of lead-acid batteries. The Zn-Ni RFB achieved 96% of average coulombic efficiency and 86% of energy efficiency over 1000 cycles, due to the decreased thickness of the diffusion layer, and

subsequent concentration polarization at the surface of the electrode.[41] Therefore, the viability of a commercial Zn-Ni RFB has been hindered by the well-known phenomena of dendrite formation and zinc morphology variation over time.[42]

$$Zn\,(s) + 2KOH + 2H_2O + 2NiOOH(s) \leftrightarrow 2Ni(OH)_2(s) + K_2Zn(OH)_4$$
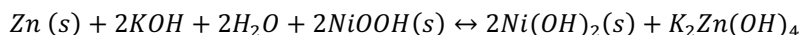
$$E^0 = 1.705 \text{ V vs. SHE} \quad (1.9)$$

Zinc-Iron

Zinc-iron (Zn-Fe) RFBs have been studied in alkaline, acidic, and alkaline-acidic supporting electrolytes. The conventional Zn-Fe RFBs with alkaline-based electrolytes are also known as "zinc-ferricyanide" batteries.[43,44] The main advantage of this redox chemistry is the utilisation of the low-cost, abundant metals in the earth´s crust. Although higher cell potential, handling solid zinc oxide precipitation in longer cycling is one of the major issues in Zn-based alkaline RFBs, as they suffer from low durability due to zinc oxide precipitation. Later on, Zn-Fe RFBs in acidic media were also developed with an OCV of 1.53 V (**Eq. 1.11**).[45] Two acidic systems are reported in Zn-Fe RFBs: i) using mixed solutions of Zn and Fe as anolyte and catholyte, ii) using Zn and Fe solutions separately, Zn in the negative and Fe in the positive side respectively. The roundtrip energy efficiency is around 60% at 25 mA·cm^{-2}, and coulombic efficiency of 91% was achieved at 30 mA·cm^{-2} in the mixed solution and the decoupled one, respectively.[24] To boost the cell voltage, alkaline-acidic supporting electrolyte system was developed by introducing a double ion-exchange membrane.[46] Although high cell voltage following power density is achieved, slow ion diffusion and low durability caused by the solid zinc oxide precipitations are the key problems for this system.

$$Zn(s) + 4OH^- + 2Fe(CN)_6^{3-} \leftrightarrow Zn(OH)_4^{2-} + 2Fe(CN)_6^{4-}$$

$$E^0 = 1.58 \text{ V vs. SHE} \quad (1.10)$$

$$Zn(s) + 2Fe^{3+} \leftrightarrow Zn^{2+} + 2Fe^{2+} \qquad E^0 = 1.53 \text{ V vs. SHE} \quad (1.11)$$

$$Zn(s) + 4OH^- + 2Fe^{3+} \leftrightarrow Zn(OH)_4^{2-} + 2Fe^{2+} \quad E^0 = 2.0 \text{ V vs. SHE} \quad (1.12)$$
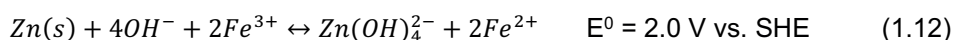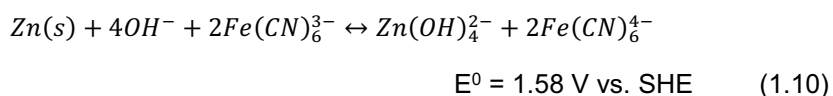
Zinc-Iodide

The zinc-iodide primary battery was first developed by Donald Ray Martin for academic demonstration in 1949,[47] employing metallic zinc and potassium iodide solution as the active electrode materials. After several decades, rechargeable zinc-iodide RFBs (ZIFBs) based on zinc iodide (ZnI$_2$) electrolyte, with a very high discharge energy density of 167 Wh·L^{-1}$_{catholyte}$ (5 M ZnI$_2$ electrolytes) were first proposed by B. Li et al. in 2015.[48] Thanks to the high solubility nature of iodide in aqueous media as well as the benign nature of zinc, thus, ZIFB enables a high energy density of ~322 Wh·L^{-1} at the solubility limit of ZnI$_2$ in the water (4,500 g·L^{-1}, 7 M). This high discharge energy density is nearly seven times that of the most researched aqueous RFBs (VRFB: ~25 Wh·L^{-1}) and approaches the energy density of low-end

LiFePO$_4$ cathode-based Li-ion batteries.[48] A ZIFB provides OCV of 1.29 V (**Eq. 1.13**). Unlike VRFB and other mentioned Zn-based hybrid RFBs, ZIFB operates with acid-free electrolyte, with near-neutral pH~3-4.

$$Zn(s) + I_3^- \leftrightarrow Zn^{2+} + 3I^- \qquad E^0 = 1.29 \text{ V vs. SHE} \qquad (1.13)$$
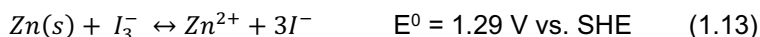
The optimum value of OCV (1.29 V) makes this RFB highly suitable to adapt to the state of the art of solar charging RFBs, where feasibility between operating voltages of photovoltaic cells and RFBs are one of the main key points to concern. Moreover, the relatively low thermodynamic potential of this system compared to the actual values required in water electrolysers, makes ZIFB a promising candidate for alternative devices integrating photoelectrodes.

1.3.2 Zinc-iodide redox flow batteries (ZIFBs)

State of the art

The ZIFB is based on the following redox reactions:

$$\text{Cathode: } I_3^- + 2e^- \leftrightarrow 3I^- \qquad E^0 = 0.563 \text{ V vs. SHE} \qquad (1.14)$$

$$\text{Anode: } Zn(s) \leftrightarrow Zn^{2+} + 2e^- \qquad E^0 = -0.763 \text{ V vs. SHE} \qquad (1.15)$$
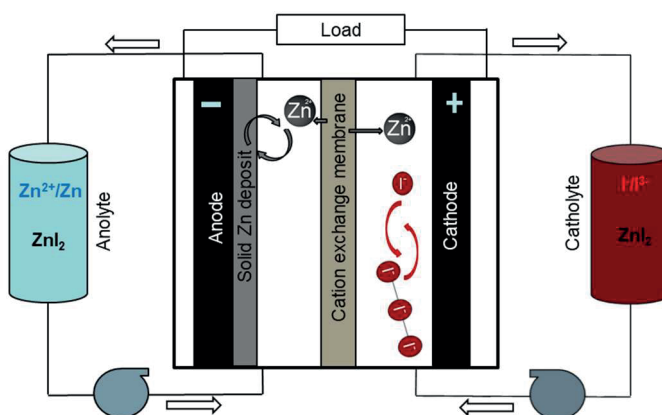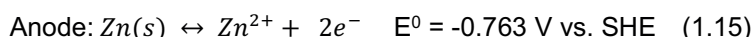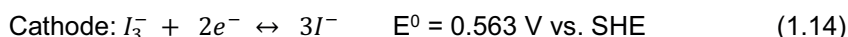
Figure 1.8. A schematic representation of a ZIFB (the sketch is not to scale).

The general schematic of ZIFB is shown in **figure 1.8**. The two active redox couples, Zn^{2+}/Zn(s) from the negative side and I$^-$/I$_3^-$ from the positive side respectively, are taking part in the redox reactions described in **Eq. 1.14 – 1.15**, where **Eq. 1.14** follows a two-step process of redox reaction (**Eq. 1.17**) and complexation (**Eq. 1.18**).[49–52]

$$2\,I^- \leftrightarrow I_2(s) + 2e^- \qquad (1.17)$$

$$I_{2(s)} + I^- \leftrightarrow I_3^- \qquad (1.18)$$
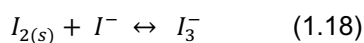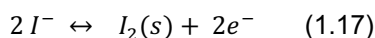
During charging, metallic Zn is reductively electrodeposited on the anode surface while triiodide ions are formed by oxidation of iodide in the positive half-cell. The reverse process occurs upon discharge.

Literature review

After the first proposal of ZIFBs based on zinc iodide (ZnI_2) aqueous electrolyte and pristine graphite felt (GF) electrodes,[48] several studies have been further conducted in this chemistry to date. As such, in terms of electrode improvement, Li and Liu et al. introduced a metal-organic framework (MOF) into the graphite felt surface as a highly active electrocatalyst, served as the positive electrode. This MOF-GF electrode shows higher energy efficiency compared to the pristine GF.[53] For achieving the long cycle life and enhanced energy density of ZIFB by mitigating the Zn dendrite formation, solid I_2 precipitation, several approaches have been done to improve the electrolyte, membrane and flow rate/system design. For example, a higher energy density of 202 Wh·L^{-1}$_{catholyte}$ has been achieved by Weng et al. by introducing bromide ion (Br$^-$) as a complexing agent to stabilise iodine molecules and free up the iodide ions which leads to increased capacity.[51] In 2018, Xie et al. described a long cycle life, high energy density ZIFB by replacing ZnI_2 with KI, $ZnBr_2$ and KCl as electrolytes and introducing a high ion conductive porous polyolefin membrane. The possibility of filling the pores of this membrane with a solution containing I_3^-, can suppress the Zn dendrite, hence, avoids the battery from micro-short circuiting.[54] Later on, the same group reported a super-high energy density single-flow ZIFB, employing a very high concentration of electrolytes (7.5 M KI and 3.75 M $ZnBr_2$), and sealing the positive compartment to avoid the blockage of the pump by solid I_2 precipitation.[55] Zhang et al. designed a high potential Zn-iodide alkaline FB by tuning the pH of the anolyte from acid to basic,[56] Ito et al. achieved over 90% coulombic efficiency after the addition of propylene carbonate in the electrolyte which forms hydrophobic polyiodide complex during cathodic oxidation in a Zn-iodide single FB without cation exchange membrane.[57] Mousavi et al. designed an ammonium chloride (NH_4Cl) supported ZIFB for achieving a very long cycle-life (2500 cycles), where multifunctional roles of NH_4Cl enhance the battery performance by mitigating Zn dendrite formation, facilitating half-cell reaction kinetics and unlocking extra capacity with the primary aid of I_2Cl^- formation.[58] A similar improvement of electrochemical performance of ZIFB has been demonstrated by Jian et al., using NH_4Br supported electrolyte, where Br$^-$ ions complex with I_2 forming soluble I_2Br^-, which frees up I$^-$ ions and thus unlocks the battery capacity, while NH_4^+ ions complex with Zn^{2+} ions to mitigate Zn dendrite formation with the electrostatic shielding effect.[59] Afterwards, Mousavi et al. explained a strategically designed, long cycle life ZIFB with an optimal catholyte to anolyte flow rate ratio (1:7) to inhibit the capacity fade trend that arises because of catholyte transport and poly(iodide) crossover from catholyte to anolyte.[60] In 2021, P.L. Roberts and group reported a ZIFB with a novel flow field design (by flow-by through mode), which significantly enhances discharge capacity and cycle life of battery compared to the conventional flow-by mode by eliminating dendrite´s growth rather leading to a compact and smoother Zn deposition.[61] Very recently, as a proof-of-concept, Li Gao et al. proposed a ZIFB with a cost-effective, high selective membrane incorporating

starch into a chitosan matrix, delivering a competitive energy efficiency (77.4%) at a current density of 80 mA·cm^{-2}. [62]

The operating conditions of ZIFB´s chemistries reported so far are summarised below:

Table 1.1. The summary of ZIFBs operational parameters reported to date.

Redox couples	Anolyte	Catholyte	Anode	Cathode	Membrane	J (mA·cm^{-2})	EE (%)
[48]**Zn-I$^-$**	5 M ZnI$_2$		GF	GF	N115	20	68
[53]**Zn-I$^-$**	2.5 M ZnI$_2$		GF	MOF-modified GF	N115	30	68
[51]**Zn-I$^-$/ Br$^-$**	5 M ZnI$_2$+2.5 M ZnBr$_2$		GF	GF	N117	10	68
[54]**Zn-I$^-$/ Br$^-$**	5 M ZnI$_2$+2.5 M ZnBr$_2$+1 M KCl		GF	GF	Polyolefin	80	80
[55]**Single-flow sealed catholyte compartment Zn-I$^-$/ Br$^-$**	7.5 M KI+3.75 M ZnBr$_2$		GF	GF	Polyolefin	20	80
[56]**Alkaline Zn-I$^-$**	6 M KOH	6 M KI+ 6 M I$_2$	Zn plate	G-foil	N117	20	70
[57]**Single-electrolyte type Zn-I$^-$**	0.5 M ZnCl$_2$ (anolyte) 1.5 M NaI (catholyte) +1 vol% PEG200, 0.15 vol% HCl, 20 vol% PC		GF	GF	Durapore	20	65
[58]**NH$_4$Cl supported-ZIFB**	2 M ZnCl$_2$+2 M NH$_4$Cl	1 M (NH$_4$I$_3$-NH$_4$I)/1.5 M NH$_4$Cl	GF	GF	N117	10	80
[59]**NH$_4$Br supported-ZIFB**	1 M ZnI$_2$+1 M NH$_4$Br		GF	GF	N115 N211	40	85
[60]**Tuned flow rate-ZIFB**	2.5 M ZnCl$_2$ +2.5 M NH$_4$Cl	5 M NH$_4$I +2.5 M NH$_4$Cl	GF	GF	Daramic	80	82
[61]**Novel flow field designed ZIFB**	3 M ZnI$_2$		GF	GF	N117	20	85
[62]**Proof of concept membrane-ZIFB**	0.5 M ZnBr$_2$/1 M KI in 2 M KCl		GF	GF	Chitosan-starch composite	80	77

Backlogs and open questions

Although the attractive features of ZIFBs consider a promising choice for future stationary energy storage, nonetheless, similar to other hybrid RFBs, the actual capacity of ZIFB chemistry is limited by the solid Zn plating/de-plating, even though the I$^-$/I$_3^-$ redox species are highly soluble (e.g. lithium iodide: c.a. 8.2 M, zinc iodide: c.a. 5.6 M, potassium iodide: c.a. 8 M) in aqueous media.[48] Moreover, all these ZIFB chemistries suffer from challenges, such as poor cyclability because of capacity

fading as a consequence of irreversible Zn plating/stripping and insoluble solid I_2 precipitation. Secondly, electrolyte volume imbalance arising from irreversible ions and water migration from one compartment to another during cycling results in unreliability for the long-term stability of ZIFB. Thirdly, low electrolyte conductivity and slow kinetics of redox reactions result in low operating current density, voltage, and energy efficiency.[55,56] All of these mentioned challenges hinder the ZIFB from large-scale deployment. Therefore, it is worth mentioning that the anode material and electrolyte play vital roles in ZIFBs round trip performance. Hence, it is an urgent need the exploration on the following studies:

i. Suitable anode material for the purpose of reversible Zn plating/stripping
ii. Enhancement in the electrolyte design for achieving long cycle life.

Despite the works reported so far in ZIFBs (**table 1.1**), few efforts have been made regarding those above-mentioned issues. Such as, enhancing the battery discharge capacity via incorporation of bromide[51,54,59] and chloride ions[58,60] as complexing agents in the electrolyte chemistry; modification as the single flow ZIFB by sealing the positive compartment, restricting the blockage of pump due to solid I_2 precipitation,[55] tuning the half-cell electrolyte flow rate for restricting the electrolyte transport during cycling,[60] alleviating the Zn deposition mechanism on the anode via engineering in the flow field design.[61]

1.4 Solar redox flow battery
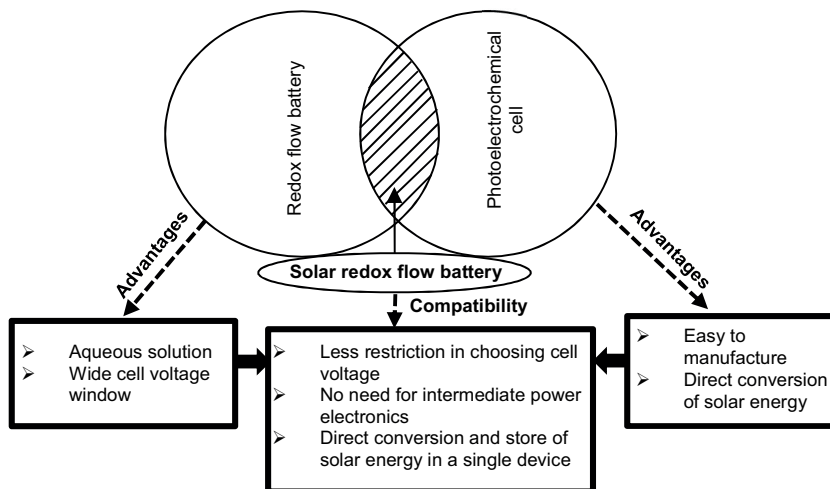
Figure 1.9. The relationship between photoelectric conversion and photoelectric storage and solar-redox flow batteries.

Although high-performance RFBs have been demonstrated even at the market level, the research for optimised RFB technology has been appealing to Today's R&D community. In this scenario, solar redox redox flow batteries appear as emerging technologies to tackle the photovoltaic intermittency issues[3] (**figure 1.9**).

1.4.1 General principles of solar redox redox flow battery

The general working scheme of solar redox flow batteries (SRFB) is illustrated in **figure 1.10**. In solar redox flow batteries (SRFBs), the solar energy absorbed by the photoelectrodes is converted into electro-chemical energy by charging up redox couples dissolved in the flowing electrolyte solutions in contact with the photoelectrodes. To deliver electricity on demand, the reverse redox reactions are carried out to release electro-chemical energy stored in the redox couples as the discharge happens in a conventional redox flow battery (RFB).[63] The integration of solar energy, electro-chemical energy and electrical energy is achieved directly and efficiently. Likewise, the conventional RFBs, where, the electrolyte is externally stored, thus, the size of the electrolytes reservoirs can be adjusted whenever needed, which is ideal for large-scale renewable energy storage. Hence, in practical applications, energy may not be produced on demand, however, needs to be stored for later use.[64]

Solar redox flow batteries (SRFB) are in some ways analogous to photoelectrochemical (PEC) water splitting, and many terminologies are borrowed from this field of research. In PEC water splitting, usually, one or two semiconductors are illuminated to split water into hydrogen and oxygen.[65] Thermodynamically, the water-splitting redox reaction requires 1.23 V; however, for practical experiments, a working device requires an additional 300-400 mV of overpotential at the electrodes even when suitable co-catalysts are used.[65] As most semiconductors cannot provide such a high voltage only from solar radiation, hence, unbiased and isolated PEC water splitting cells are crucial to design. A solar redox flow battery can alleviate this barrier since the cell voltage can be chosen freely.
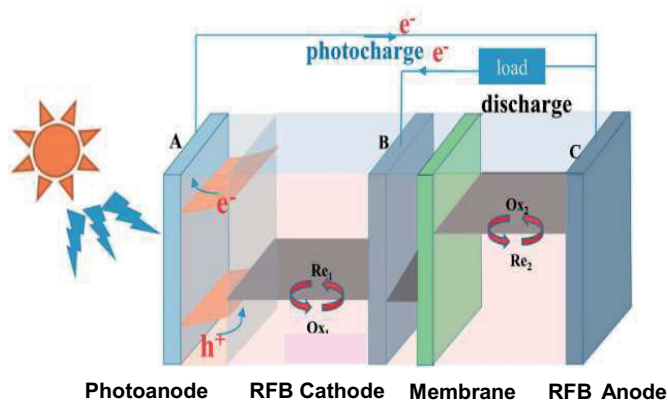
Figure 1.10. The working mechanism of solar redox flow battery (SRFB). Adapted from L. Gao et al.[66] (the sketch is not to scale).

Advantages and disadvantages

The feasibility of the integration of solar cells and RFB has been demonstrated by the recent emerging research, which shows several distinct advantages of using this integrated system to maximise the full-fledge utilisation of solar energy.

- The stored excess solar energy in the form of chemical energy by RFBs could be utilised in case of power shortages and unsustainable supply and could even transfer solar energy to cloudy areas or at night-time when there is no sunlight.
- Thanks to the compact and simple design of this integrated solar RFB, it can be utilised both locally and efficiently even in very remote areas. As long as the photoelectrode absorbs the sunlight, the electricity cost in these areas can be greatly reduced.
- Unlike the usual solar energy to electricity transfer mechanism, the loss of energy transfer between different devices will be largely reduced, which not only enhances the utilisation efficiency of solar energy but also shows distinctive benefits of safety and environmental protection.[64]

Despite the emerging state-of-the-art progress, SRFB technology is still in the infancy R&D stage, trying to overcome several drawbacks. Such as inevitable energy loss inside this integrated system, mainly caused by the poor photo-stability of electrolytes; polarisation and electron transfer through interfaces;[64] ohmic resistance when the integration is done by wired connections not monolithically, as well as, the low capacity; limited performance of photovoltaics/photoelectrodes such as insufficient photovoltage, photocurrent; poor stability of photoelectrodes in contact with electrolytes; and mismatch in the operation power between the photovoltaics/photoelectrodes and the RFB. These detailed drawbacks make it difficult to realise break-through high solar-to-output electricity efficiency and high energy density.[64]

1.4.2   History and current state of the art of SRFB

Leveraging rapidly developing parallel technologies of photovoltaic solar cells and RFBs, significant progress in the field of SRFBs has been made in the past few years (**figure 1.11**). The historical development of photoelectrochemical (PEC) storage devices shows, however, that this is not a recent approach.[67] Between the late 1970s and the late 1980s, many PEC approaches using organic and inorganic redox-pairs in `no-flow´ configurations were developed,[68,69] mostly with photoelectrodes in direct contact with the electrolyte and based on metal oxides, chalcogenides and III–V semiconductors. These early-stage periods are denoted as the `PEC Golden Age´. Although some systems demonstrated impressive efficiency values (e.g., solar-to-electrical energy conversion efficiency of 11.8%),[69] relevant aspects such as limited availability of low-cost and efficient photo-absorbers and membranes notably restrained the interest in these approaches at the time. Over the last few years, with the progress in PV technology and electrochemical devices (with more efficient and

cheaper membranes and cells), this possibility has re-gained attention, with configurations aiming to create compact and cost-effective devices by integrating PV materials or developing photoelectrodes in RFB systems. Due to the ease of fabrication, simple semiconductor photoelectrodes were found in most of the early SRFB demonstrations. For instance, the I^-/I_3^- redox pair used in the dye-sensitised solar cell (DSSC) technology[70] has led to the development of integrated systems with SSCs based on iodine catholytes and anolytes such as lithium.[71–74] These systems, however, are limited by the performance of TiO_2 photoanodes. More recently, quinone/halogen RFBs with relatively low cell potential (~0.8 V) have also appeared as examples of successful SRFBs, by using Si,[75,76] hematite,[77] WSe_2,[78] although the intrinsic cell potential limits their discharge power. A more recent example of higher voltage batteries has been proposed by Wang and group[79] with a ferrocyanide/anthraquinone battery with an integrated Ta_3N_5 photoanode and GaN/Si photocathode reaching 1.2 V with static operating conditions. Further, ferricyanide was explored by pairing with TEMPO-sulfate in a neutral media, to unbiased photo charging by TiO_2 protected Si photocathode by Bentien et al.[80] Other semiconductor materials, including $BiVO_4$[81] have addressed in SRFB application. In 2018, Li et al. addressed a monolithically integrated system with organic redox pairs and an III-V tandem solar cell with PV efficiency of 26.1%, reaching a record efficiency of 14.1%.[82] Despite the promising value attained, an intrinsic loss of 0.6 V photovoltage resulting in undesired efficiency loss compared to the solar cell efficiency evinces the need for proper matching.
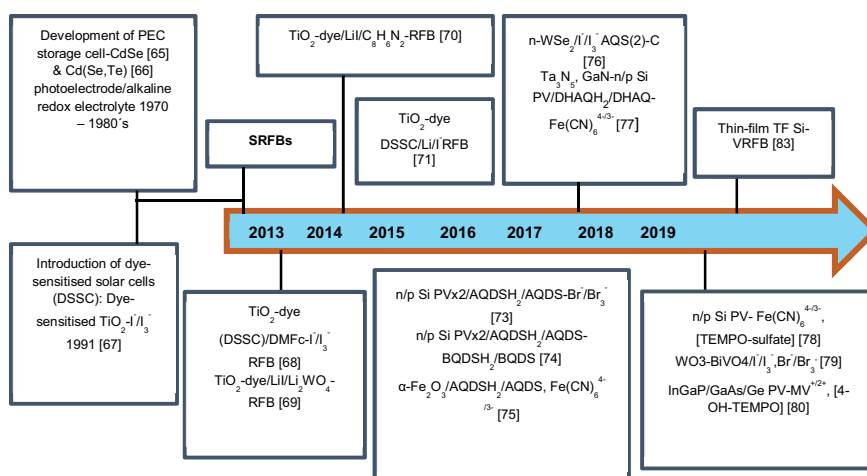
Figure 1.11. A timeline of the key development of SRFB. Design and information adapted from Sanchez-Díez et al.[3] and Wenjie Li et al.[83]

Compared to other RFBs, the mostly investigated all-vanadium RFBs, which display a higher power density considering their standard cell potential of 1.26 V, reaching values of up to 1.7 V in real operation,[84] but also represent a more challenging approach for PV integration. Despite this, they have already been demonstrated to be suitable energy storage systems for renewable solar and wind energy, even with power output fluctuations of the renewable system.[84] A CdS/DSSC photoanode proposed by Azevedo et al.,[85] and a monolithic triple-junction solar cell proposed by Urbain et al.,[31] are until now the only examples of integrated systems in full VRFBs, as the other studies on solar VRFBs have used TiO_2 photoelectrodes, reaching limited state-of-charge (SOC) or providing photo-assisted charge under low bias conditions.[86,87]

1.4.3   Backlogs and open questions

So far, from the current progress in SRFBs, it is clear that the exploration of the highly efficient yet low-cost photoabsorbers with the proper matching between photovoltage and RFB charging voltage (voltage requirements for VRFB: ~1.3 – 1.6 V) is still not deeply investigated. In parallel, to achieve industrial acceptance of SRFBs, new RFB chemistries using inexpensive and earth-abundant materials have not been well studied to reach advantages in lifespan and energy density values.

1.5 Objective of the thesis

The rapidly emerging Zn-based alternative RFBs is one of the promising contender for next generation solar energy storage. Among these alternative RFBs, ZIFB was selected as the targeted redox-couple for this thesis due to the unique features of earth-abundant, benign redox active material; corrosion free electrolytes; high discharge energy density and most importantly, optimum OCV, suitable to adapt to the solar charging RFB system. This appealing redox chemistry offers several open questions to be resolved for the sake of its full-fledged deployment. Therefore, in this work, we have focused our investigations on the enhancement of the ZIFB electrochemical performance mainly at lower operating current densities, suitable for the adaptation with the photovoltaic system. Furthermore, challenges arising from operating at lower current densities have been thoroughly investigated in this thesis. The main objectives of the thesis can be stated as follows:

- o Optimisation of ZIFB anode materials.
- o Suppression of the electrolyte volume imbalance during ZIFB cycling.
- o Improving the cyclability and capacity retention of ZIFB.
- o Device level adaptation of commercial PV module with lab-scale RFB.
- o Integration of optimised ZIFB with a low-cost PV cell.

In relation to the objectives stated above, the thesis is structured as follows:

- • **Chapter 2** presents the materials preparations and experimental methods and techniques used in this thesis.

Part I. Electrochemical performance evaluation of ZIFB.

- • **Chapter 3** presents the selection of the anode material to be used in ZIFB cycling on the basis of electrochemical and physicochemical analyses.

- • **Chapter 4** deals with the observations of the volume imbalances of electrolytes during cycling. Based on our analysis, a strategical experimental model has proposed to alleviate this issue.

- • **Chapter 5** is focused on the boosting the cycle life of ZIFB with the help of a cost-effective supporting electrolyte. The specific role of this supporting electrolyte in improving the ZIFB overall performance is thoroughly explained.

Part II. Unbiased photocharging of redox flow batteries: Solar RFBs.

- **Chapter 6** presents the first-time integration of commercial CIGS modules into VRFB for bias-free charging. Optimum operating voltage and power needed for unbiased photocharging were deeply studied.

- **Chapter 7** presents an approach of integrating the cost-optimised organic PV cell with the ZIFB of optimised chemistry from the part I of the thesis. The main advantages as well as remaining challenges of this final study of this thesis is highlighted.

Finally, **Chapter 8** draws general conclusions and highlights the original contributions of the thesis work. Some recommendations for future research are also provided.

1

1.6 References

1. *Renewable Energy Market Update*, (2020).

2. International Renewable Energy Agency, *Irena*, 1–3 (2021).

3. E. Sánchez-Díez, E. Ventosa, M. Guarnieri, A. Trovò, C. Flox, R. Marcilla, F. Soavi, P. Mazur, E. Aranzabe, and R. Ferret., *J. Power Sources*, **481** (2021).

4. L. . Mears and H. L. Gotschall, *EPRI-DOE Handbook of Energy Storage for Transmission & Distribution Applications*, (2003).

5. P. Alotto, M. Guarnieri, and F. Moro, *Renew. Sustain. Energy Rev.*, **29**, 325–335 (2014).

6. C. Ponce de León, A. Frías-Ferrer, J. González-García, D. A. Szánto, and F. C. Walsh, *J. Power Sources*, **160**, 716–732 (2006).

7. Z. Yang, J. Zhang, M. C. W. Kintner-Meyer, X. Lu, D. Choi, J. P. Lemmon, and J. Liu, *Chem. Rev.*, **111**, 3577–3613 (2011).

8. International Renewable Energy Agency (IRENA), *Electricity storage and renewables: Costs and markets to 2030*, p. 132, (2017).

9. A. Z. Weber, M.M. Mench, J. P. Meyers, P. N. Ross, J. T. Gostick, and Q. Liu., *J. Appl. Electrochem.*, **41**, 1137–1164 (2011).

10. G. L. Soloveichik, *Chem. Rev.*, **115**, 11533–11558 (2015).

11. H. Chen, T. N. Cong, W. Yang, C. Tan, Y. Li, and Y. Ding, *Prog. Nat. Sci.*, **19**, 291–312 (2009).

12. M. Skyllas-Kazacos, L. Cao, M. Kazacos, N. Kausar, and A. Mousa, *ChemSusChem*, **9**, 1521–1543 (2016).

13. Y. K. Zeng, X. L. Zhou, L. An, L. Wei, and T. S. Zhao, *J. Power Sources*, **324**, 738–744 (2016).

14. M. C. Wu, T. S. Zhao, H. R. Jiang, Y. K. Zeng, and Y. X. Ren, *J. Power Sources*, **355**, 62–68 (2017).

15. W. Wang, Q. Luo, B. Li, X. Wei, L. Li, and Zhenguo Yang, *Adv. Funct. Mater.*, **23**, 970–986 (2013).

16. M. Park, J. Ryu, W. Wang, and J. Cho, *Nat. Rev. Mater.*, **2**, 1–18 (2016).

17. H. S. Lim, A. M. Lackner, and R. C. Knechtli, 1154–1157 (1978).

18. M. Skyllas-Kazacos, M. Rychcik, R. G. Robins, and A. G. Fane, *J. Electrochem. Soc.*, **133**, 1057–1058 (1986).

19. N. Ra and A. Bhattacharjee, *Energy Technol.*, **9**, 18 (2021).

20. Y. A. Gandomi, D. S. Aaron, J. R. Houser, M. C. Daugherty, J. T. Clement, A. M. Pezeshki, T. Y. Ertugrul, D. P. Moseley, and M. M. Mench, *J. Electrochem. Soc.*, **165**, A970–A1010 (2018).

21. V. Singh, S. Kim, J. Kang, and H. R. Byon, *Nano Res.*, **12**, 1988–2001 (2019).

22. P. Leung, A. A. Shah, L. Sanz, C. Flox, J.R. Morante, Q. Xu, M.R. Mohamed, C. Ponce de Leon, and F.C. Walsh, *J. Power Sources*, **360**, 243–283 (2017).

23. M. J. Kwabi, D. G. Ji, and Y. Aziz, *Chem. Rev.*, **120**, 6467–6489 (2020).

24. A. Khor, P. Leung, M. R. Mohamed, C. Flox, Q. Xu, L. An, R. G. A. Wills,

J. R. Morante, and A. A. Shah., *Mater. Today Energy*, **8**, 80–108 (2018).

25. T. M. Gür, *Energy Environ. Sci.*, **11**, 2696–2767 (2018).

26. D. Reynard, C. R. Dennison, A. Battistel, and H. H. Girault, *J. Power Sources*, **390**, 30–37 (2018).

27. A. Parasuraman, T. M. Lim, C. Menictas, and M. Skyllas-Kazacos, *Electrochim. Acta*, **101**, 27–40 (2013).

28. M. Rychcik and M. Skyllas-Kazacos, *J. Power Sources*, **22**, 59–67 (1988).

29. M. Skyllas-Kazacos, M. H. Chakrabarti, S. A. Hajimolana, F. S. Mjalli, and M. Saleem, *J. Electrochem. Soc.*, **158**, R55–R79 (2011) h.

30. M. Skyllas-Kazacos, C. Menictas, and M. Kazacos, *J. Electrochem. Soc.*, **143**, L86–L88 (1996).

31. F. Urbain, S. Murcia-López, N. Nembhard, J. Vázquez-Galván, C. Flox, V. Smirnov, K. Welter, T. Andreu, F. Finger and J. R. Morante, *J. Phys. D. Appl. Phys.*, **52,** 044001 (2018).

32. J. Winsberg, T. Hagemann, T. Janoschka, M. D. Hager, and U. S. Schubert, *Angew. Chemie - Int. Ed.*, **56**, 686–711 (2017).

33. A. J. Bard. R. Parsons. and J. Jordan, *Standard potentials in aqueous solutions*, p. 848, (1985).

34. X. Li, P. de Léon C., F. C. Walsh, R. G. A. Wills, and D. Pletcher, *Adv. Batter. Mediu. Large-Scale Energy Storage Types Appl.*, 293–315 (2015).

35. P. C. Butler, D. W. Miller, and A. E. Verardo, *Proc. Intersoc. Energy Convers. Eng. Conf.*, **2**, 653–658 (1982).

36. J. Noack, N. Roznyatovskaya, T. Herr, and P. Fischer, *Angew. Chemie - Int. Ed.*, **54**, 9776–9809 (2015).

37. P. Butler, P. Eidler, and P. Grime, *Zinc/Bromine Batteries*, p. 37.2, (2001).

38. F. R. Lewis Clarke, B. Dougherty, S. Harrison, P. J. Millington, and S. Mohanta, **2**, 78–84 (2004).

39. R. Lewis Clarke, B. J. Dougherty, S. Harrison, P. J. Millington and S. Mohanta, **2** (2006).

40. L. Zhang, J. Chenga, Y. S. Yang, Y. H. Wen, X. D. Wang, and G. P. Cao, *J. Power Sources*, **179**, 381–387 (2008).

41. J. Cheng, L. Zhang, Y. S. Yang, Y. H. Wen, G. P. Cao, and X. D. Wang, *Electrochem. commun.*, **9**, 2639–2642 (2007).

42. S. Li, K. Li, E. Xiao, R. Xiong, J. Zhang, and Peter Fischer, *J. Power Sources*, **445**, 227282 (2020).

43. N. J. Magnani, R. B. Diegle, J. W Braithwaite, D. M. Bush, J. M. Freese, A. A. Akhil, and S. E. Lott *Sandia Natl. Lab.*, 123 (1987).

44. L. W. Hruska and R. F. Savinell, *J. Electrochem. Soc.*, **128**, 18–25 (1981).

45. Z. Xie, Q. Su, A. Shi, B. Yang, B. Liu, J. Chen, X. Zhou, D. Cai, and L. Yang, *J. Energy Chem.*, **25**, 495–499 (2016).

46. K. Gong, X. Ma, K. M. Conforti, K. J. Kuttler, J. B. Grunewald, K. L. Yeager, M. Z. Bazant, S. Gu and Y. Yan, *Energy Environ. Sci.*, **8**, 2941–2945 (2015).

47. R. A. Y. Martin, 496 *Journal of chemical education* 2–4 (1948).

48. B. Li, Z. Nie, M. Vijayakumar, G. Li, J. Liu, V. Sprenkle and W. Wang, *Nat. Commun.*, **6**, 1–8 (2015).

49. M. Davies and E. Gwynne, *J. Am. Chem. Soc.*, **74**, 2748–2752 (1952).

50. V. J. C and E. Barendrecht, *Electrochim. Acta*, **23**, 433–438 (1978).

51. G. M. Weng, Z. Li, G. Cong, Y. Zhou, and Y. C. Lu, *Energy Environ. Sci.*, **10**, 735–741 (2017).

52. M. Chakraborty, S. Murcia-Lopez, J. R. Morante, and T. Andreu, *J. Electrochem. Soc.*, **168**, 040532 (2021).

53. B. Li, J. Liu, Z. Nie, W. Wang, D. Reed, J. Liu, P. McGrail, and V. Sprenkle, *Nano Lett.*, **16**, 4335–4340 (2016).

54. C. Xie, H. Zhang, W. Xu, W. Wang, and X. Li, *Angew. Chemie - Int. Ed.*, **57**, 11171–11176 (2018).

55. C. Xie, Y. Liu, W. Lu, H. Zhang, and X. Li, *Energy Environ. Sci.*, **12**, 1834–1839 (2019).

56. J. Zhang, G. Jiang, P. Xu, A. G. Kashkooli, M. Mousavi, A. Yu and Z. Chen, *Energy Environ. Sci.*, **11**, 2010–2015 (2018).

57. S. Ito, M. Sugimasa, Y. Toshimitsu, A. Orita, M. Kitagawa, and M. Sakai, *Electrochim. Acta*, **319**, 164–174 (2019).

58. M. Mousavi, G. Jiang, J. Zhang, A. G. Kashkooli, H. Dou, C. J. Silva, Z. P. Cano, Y. Niu, A.Yu, and Z. Chen., *Energy Storage Mater.*, **32**, 465–476 (2020).

59. Q. P. Jian, M. C. Wu, H. R. Jiang, Y. K. Lin, and T. S. Zhao, *J. Power Sources*, **484**, 229238 (2021).

60. M. Mousavi, H. Dou, H. Fathiannasab, C. J. Silva, A. Yu, and Z. Chen *, *Chem. Eng. J.*, **412**, 128499 (2021).

61. F. Shakerihosseinabad, S. R. Daemi, D. Momodu, D. J. L. Brett, P. R. Shearing, and E. P. L. Roberts., *ACS Appl. Mater. Interfaces*, **13**, 41563–41572 (2021).

62. L. Gao, Y. Ding, G. He, and G. Yu, *Small*, **2107055**, 1–7 (2022).

63. W. Li and S. Jin, *Acc. Chem. Res.* (2020).

64. P. Lu, P. Leung, H. Su, W. Yang, and Q. Xu, *Appl. Energy*, **282**, 116210 (2021).

65. R. va de Krol and M. Grätzel, *Photoelectrochemical Hydrogen Production*, p. 322, (2012).

66. L. Gao, X. Zhang, X. Zhao, S. Tao, and J. Lu, *Chem. Lett.*, **49**, 248–251 (2020).

67. K. Wedege, D. Bae, W. A. Smith, A. Mendes, and A. Bentien, *J. Phys. Chem. C*, **122**, 25729–25740 (2018).

68. D. Hodes, G., Manassen, and J. Cahen, *Nature*, **261**, 403–404 (1976).

69. S. Licht, G. Hodes, R. Tenne, and J. Manassen, *Lett. to Nat.*, **326**, 863–864 (1987).

70. A. Amin, M. Al Emran, and M. F. Hossain, *academia* (1991).

71. P. Liu, Y. I. Cao, X. P. Ai, and H. X. Yang *ChemSusChem*, **6**, 802–806 (2013).

72. G. R. L. and X. P. G. N. F. Yan, *J. Mater. Chem. A*, **1**, 7012–7015 (2013).

73. N. F. Yan, G. R. Li, and X. P. Gao, **161**, 736–741 (2014).

74. M. Yu, W. D. McCulloch, D. R. Beauchamp, Z. Huang, X. Ren, and Y. Wu., *J. Am. Chem. Soc.*, **137**, 8332–8335 (2015).

75. S. Liao, X. Zong, B. Seger, T. Pedersen, T. Yao, C. Ding, J. Shi, J. Chen, and C. Li, *Nat. Commun.*, **7** (2016).

76. W. Li, H-C. Fu, L. Li, M. C-Acevedo, Jr-H He, and S. Jin, *Angew. Chemie - Int. Ed.*, **6900**, 13298–13302 (2016).

77. K. Wedege, J. Azevedo, A. Khataee, A. Bentien, and A. Mendes, *Angew. Chemie - Int. Ed.*, **55**, 7142–7147 (2016).

78. J. R. McKone, F. J. DiSalvob, and H. D. Abruña, *J. Mater. Chem. A*, **5**, 5362–5372 (2017).

79. Q. Cheng, W. Fan, Y. He, P. Ma, S. Vanka, S. Fan, Z. Mi, and D. Wang, *Adv. Mater.*, **29**, 1–8 (2017).

80. K. Wedege, D. Bae, E. Drazevic, A. Mendes, P. C. K. Vesborg and A, Bentien *RSC Adv.*, **8**, 6331 (2018).

81. Y. Zhou, S. Zhang, Y. Ding, L. Zhang, C. Zhang, X. Zhang, Y. Zhao, and G. Yu, *Adv. Mater.*, **103**, 1802294 (2018).

82. W. Li, H. C. Fu, Y. Zhao, J. H. He, and S. Jin, *Chem*, **4**, 2644–2657 (2018).

83. W. Li, J. Zheng, B. Hu, H-C. Fu, M. Hu, A. Veyssal , Y. Zhao Jr-H. He, T. L. Liu,

A. H-Baillie, and S. Jin, *Nat. Mater.*, **19**, 1326–1331 (2020).

84. R. López-Vizcaíno, E. Mena, M. Millán, M. A. Rodrigo, and J. Lobato, *Renew. Energy*, **114**, 1123–1133 (2017).

85. J. Azevedo, T. Seipp, J. Burfeind, C. Sousa, A. Bentien, J. P. Araújo, and A. Mendes, *Nano Energy*, **22**, 396–405 (2016).

86. Z. Wei, Y. Shen, D. Liu, and F. Liu, *Sci. Rep.*, **7**, 1–9 (2017).

87. S. Liao, J. Shi, C. Ding, M. Liu, F. Xiong, N. Wang, J. Chen, and C. Li, *J. Energy Chem.*, **27**, 278–282 (2018).

Chapter 2

RFB cell set up and experimental techniques

This chapter has been mainly written for the thesis, which also includes a summary of the "Materials and methods" sections of the paper published and under review for publishing during the thesis (presented as Chapters 3 – 6).

2

2.1 Introduction

This chapter presents the collection of materials preparation, experimental techniques and methods used in this PhD dissertation. It starts by describing the materials preparation (**section 2.2**) where assembling of the lab scale ZIFB, pre-treatment procedures of cell components and theoretical cell capacity calculation have been explained. Then follows different electrochemical characterisation methods of ZIFB and SRFB (**section 2.3**) where evaluation of ZIFB full-cell and half-cell have been described along with the standard figures of merit of RFBs and SRFBs. Finally, the chapter closes by describing ex-situ physicochemical characterisation methods (**section 2.4**) used in this thesis.

2.2 Materials

This section briefly detailed the overview of the materials and their preparations, which have used to perform most of the experiments throughout the thesis.

2.2.1   Lab-scale ZIFB single cell

The ZIFB single cell was assembled using an in-house designed flow cell setup (**figure 2.1**). Electrodes of 10 cm^2 geometric area were assembled by sandwiching Nafion® 117 membrane in between two half-cell compartments. In the anode compartment, graphite felt (Sigracell® GFA 1.5 EA, 1.5 mm thick), carbon paper (Toray® TGP-H-60, 0.18 mm thick), graphite foil (Alfa Aesar®, 0.5 mm thick) or Zn metal foil (Goodfellow®, 0.5 mm thick) were used as anodes (experiments with these different anodes only performed for **Chapter 3**, afterward only graphite foil was used as anode in rest of the experiments of the thesis). Titanium metal plate was used as a negative current collector. Around 4 mm space was kept between the anode surface and membrane for the metallic Zn deposition. In the cathode compartment, two stacked graphite felts were used as the cathode in contact with a graphite plate as the positive current collector. Viton® gaskets were used in between each component to avoid electrolyte leakage. Electrolyte was prepared at room temperature by mixing 1.5 M ZnI$_2$ (98.0%, Aldrich) and KI (99.5%, Sigma Aldrich) (1:1) in aqueous solution (milli-Q ultrapure, deionised water). The cell was connected to 10 mL of electrolyte reservoirs on each side. Electrolyte was circulated to the cell by a peristaltic pump (Masterflex L/S series) through Tygon® tubing at a fixed flow rate of 13 mL·min^{-1} (**figure 2.2**).
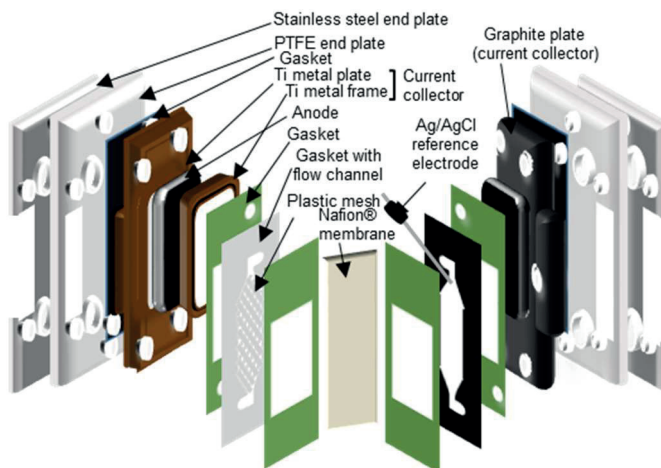
Figure 2.1. Lab-scale assembling of single-cell ZIFB.
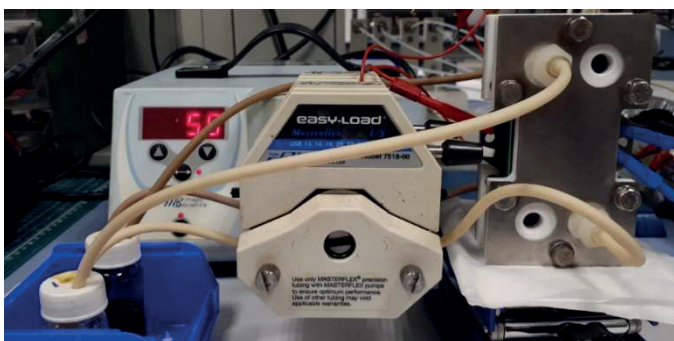
Figure 2.2. Digital photograph of the running ZIFB full-cell.

Graphite felt pre-treatment

In order to introduce oxygen functional groups, graphite felt (G-felt) electrodes were thermally pre-treated at 420°C for 10 hours using a ramp rate of 5°C min^{-1} in air.

Membrane pre-treatment

The membrane used for all the experiments is Nafion 117 cation exchange membrane. In order to activate the sulfonated groups on the surface, the pre-treatment process was done as of described in **figure 2.3**.

All these steps were done at 80°C for 1 hour on each. After the pre-treatment, the membrane is always stored in 0.5 M H_2SO_4.
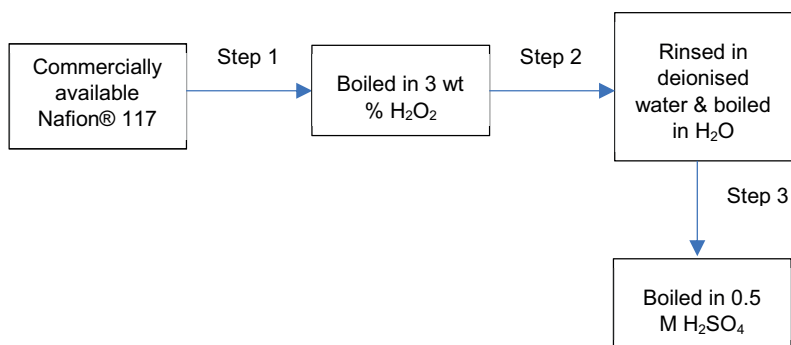
Figure 2.3. Pre-treatment procedures of Nafion 117.

There are some further modifications in the component selection between **Chapters 3 – 5**, which are summarised in **table 2.1**.

Table 2.1. The summary of ZIFB cell configurations is used in the different chapters.

	Chapter 3	**Chapter 4**	**Chapter 5**
Anode	Graphite felt (pre-treated) Carbon paper Graphite foil Zinc foil	Graphite foil	Graphite foil
Cathode	Two stacked graphite felts (pre-treated)		
Anolyte	1.5 M ZnI_2:KI	1.5 M ZnI_2:KI	1.5 M ZnI_2:KI:NaCl*
Catholyte		1.5 M ZnI_2:3.5 M KI*	1.5 M ZnI_2:3.5 M KI:1.5 M NaCl*
Membrane	Nafion 117 (pre-treated)		
Flow rate	13 mL·min^{-1}	13 mL·min^{-1}	25 mL·min^{-1}

*The details about these electrolytes solution chemistry are briefed in the corresponding chapters.

2.2.2 Theoretical capacity calculation from ZnI_2:KI (1:1) electrolyte

The overall redox reactions of ZIFB (previously mentioned in **Chapter 1**, **Eq. 1.13**):

$$I_3^- + Zn(s) \leftrightarrow 3I^- + Zn^{2+} \quad E^0 = 1.299 \text{ V vs. SHE}$$
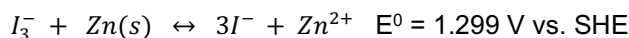
where the positive side redox reaction follows a two-step process (previously mentioned in **Chapter 1**, **Eq. 1.17** and complexation **Eq. 1.18**).

$$2I^- \leftrightarrow I_2 + 2e^-$$

$$I_2 + I^- \leftrightarrow I_3^-$$
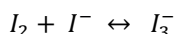
In our electrolyte chemistry, the mixing of potassium iodide (KI) along with ZnI_2 (1:1) provides enough free I^- ions in the solution to equilibrate both compartments in terms of theoretical capacity.

As per Faraday´s law,

$$\text{Capacity} = F * c * n * V \qquad (2.1)$$

Where F is Faraday´s constant, c is the concentration of ions in the salt, n is the number of electrons participating in the reaction per mole of reactant, and V is the volume of electrolyte.

Negative half-cell: (Zn^{2+} as reactant)

For 10 mL of a solution of 1.5 M ZnI_2,

Theoretical capacity = 0.804 Ah

Positive half-cell: (I^- as reactant)

For 10 mL of a solution of:

1.5 M ZnI_2:   Theoretical capacity = 0.536 Ah

1.5 M KI: Theoretical capacity = 0.268 Ah

In total: Theoretical capacity = (0.536 Ah + 0.268 Ah) = 0.804 Ah

However, according to the two-step redox reaction process of positive (I^-) side, just 2/3 of I^- ions are taking part in the charging process which corresponds to ~67% state of charge (SOC), while the remaining I^- forms highly soluble polyiodide, I_3^-. Thus, if the charging continues to higher SOC, there will be the formation of insoluble solid I_2 which can further lead to interrupt the electrolyte flow by blocking the tubing side following capacity loss.[1] Moreover, this maximum SOC before precipitation of solid I_2 is further calculated based on the equilibrium equation.

Maximum capacity calculation

In ZIFB systems, during charge, Zn^{2+} ions at the negative side are electroplated onto the surface of the anode in metallic form. Meanwhile, Zn^{2+} ions are also participating as charge carriers across the cation exchange membrane (CEM). Therefore, the same amount of Zn^{2+} ions transfer through the membrane from positive to negative half-cell to balance the charge due to the negligible transportation of I$^-$ ions through the CEM. During discharge the reverse process takes place. As a result, the amount of Zn^{2+} ions will decrease on the positive side and remain constant on the negative side with increasing the state of charge (SOC). Based on the experiments performed by B. Li and group,[2] flow cell charge/discharge cycling with varied anolyte volumes deliver identical energy output. Therefore, it is concluded that the anolyte in a ZIFB flow cell does not directly participate in the redox reactions that contribute to the overall cell energy and power delivery. The energy density of a ZIFB flow cell is solely dependent on the concentration of the catholyte. Therefore, all volumetric cell capacity and energy density are calculated based on the catholyte volume assuming that all the I$^-$ is converted into I$_3^-$ in catholyte on charge.

Based on the redox reaction of the positive side in the following equation (previously mentioned in **Chapter 1, Eq. 1.14**):

$$I_3^- \ + \ 2e^- \ \leftrightarrow \ 3I^- \qquad E^0 = 0.563 \text{ V vs. SHE}$$

The SOC can be expressed according to the following reaction:

$$SOC = \frac{[I_3^-]}{\frac{1}{3}[I^-] + [I_3^-]}$$

And the remaining concentration of I$^-$ can be calculated as:

$$[I^-] = \frac{3[I_3^-](1 - SOC)}{SOC}$$

Also, based on the equilibrium constant of the complexation reaction (**Eq. 1.18 of Chapter 1**) ($K_{eq} \sim 780$ at 25ºC):

$$K_{eq} = \frac{[I_3^-]}{[I_2][I^-]} = 780$$

For the maximum I_2 concentration determined by its theoretical water solubility $[I_2]$ = 0.011 M (at 25ºC), and by combining the two previous equations, it is possible to determine the maximum SOC before precipitation of solid I_2 occurs:

$$SOC_{max} \approx 72\%$$

Based on the previous calculation, a limiting SOC of 67% was defined, which for our system conditions, represents 0.536 Ah of charge capacity limit.

Specific capacity (Ah·L^{-1}) has been calculated based on the volume of the catholyte (10 mL).

2.2.3   ZIFB cell design for in-situ electrochemical analysis

The below-mentioned specific cells design for *in-situ* electrochemical study has been implemented in the study of **Chapter 4**.

The schematic of these cells set-up is represented in **figure 2.4** (practical set-up after assembling is shown in **figure 2.5**). ZIFB single cell as described in **section 2.2.1**, is connected to these two identical, auxiliary cells in series.

These identical cells were built for performing half-cell electrolytes resistances by *in-situ* electrochemical impedance spectroscopy (EIS). The components details are described in **figure 2.6**. These auxiliary cells are made up of graphite foil as working electrode and graphite felt as counter/reference electrode of 4 cm^2 electrode geometric areas, without a separator/membrane. Graphite foil and graphite felt are the same as used in the ZIFB single cell. Each half-cell electrolyte passed through the ZIFB single cell which then entered into these auxiliary cells, finally flowing out from the auxiliary cells to the reservoirs. Graphite plates with serpentine flow frames are used as current collectors.
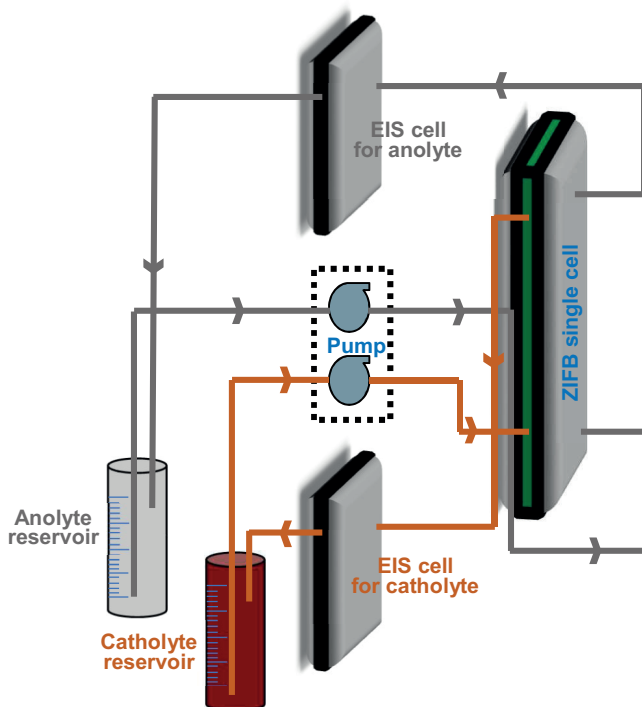
Figure 2.4. Schematic representation of cells set up for *in-situ* electrochemical analysis: ZIFB lab-based single cell with two auxiliary cells.
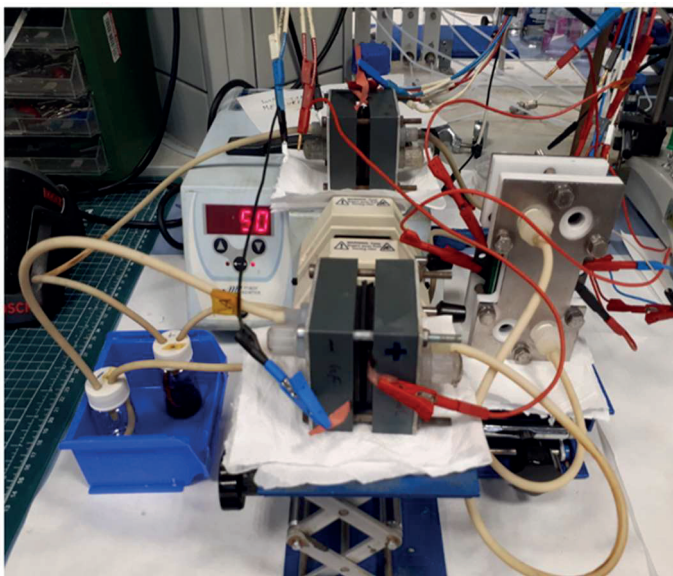
Figure 2.5. Practical image of the cells set up for *in-situ* electrochemical analysis.
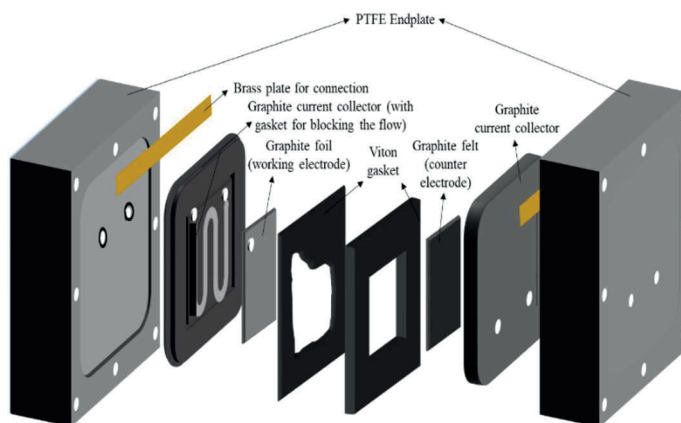
Figure 2.6. Auxiliary cell components in detail.

A note to the reader:

As mentioned in **Chapter 1 section 1.5**, **Part II** of the thesis is focused on the adaptation of the lab-scale based RFB to the photovoltaic cell for achieving solar powered RFB. The general idea of SRFB cell preparation follows almost the same as what is detailed in **section 2.2.1** except for some deviation in the components between the ZIFB and SVRFB. Rest of the details such as, the fabrication of photovoltaic (PV) cells; coupling of the PV cell with the RFB (SVRFB and SZIFB) will be provided in the experimental sections of **Chapters 6** and **7** dedicated to SRFB.

2.3 Electrochemical characterisation

This section briefly details the overview of the various experimental techniques implied in this thesis. Such as evaluation of the ZIFB cells with various electrochemical and physicochemical techniques, following, general characterisation methods, which are, used as the standard practices in lab-based SRFB studies.

2.3.1 Evaluation of lab-scale ZIFB single cell

Charge/discharge cycling

An assembled RFB built with desired redox couples is characterised by galvanostatic cycling to determine the energy density, coulombic, voltage, and energy efficiencies. Moreover, cycling tests also reveal the lifetime of RFBs, which is usually determined by the chemical stability and membrane permeability of redox couples.[3]
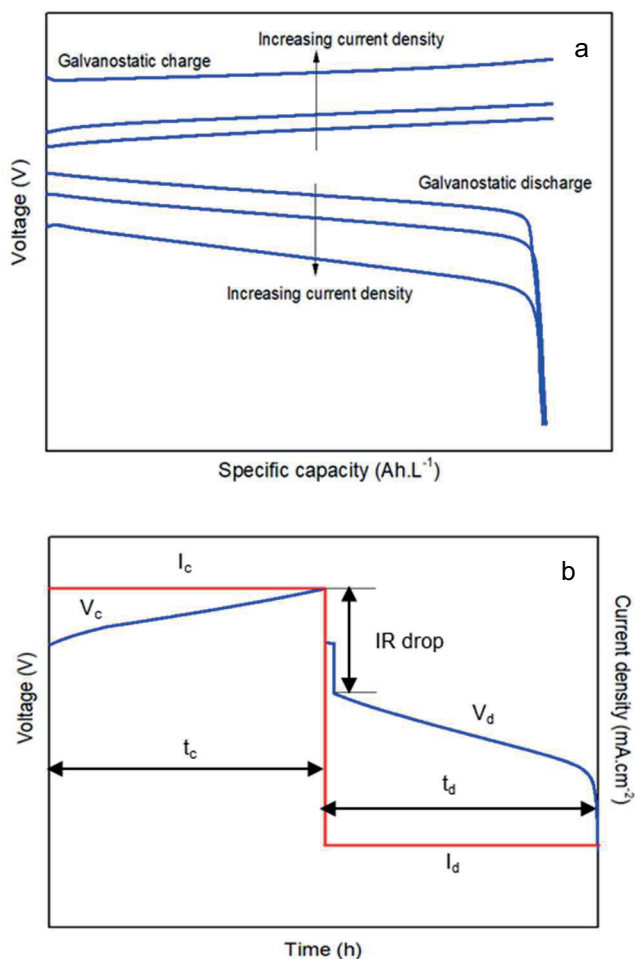
Figure 2.7. Galvanostatic cycling of RFB: (a) traditional charge-discharge curves and (b) cycling profile of one cycle.

Figure 2.7a shows the classical galvanostatic charge and discharge curves with increasing current density of RFB. The higher the applied current density leads to higher internal losses. **Figure 2.7b** depicts a better insight into the charge-discharge operation. Where V_c and V_d refer to charging and discharging voltages; I_c and I_d refer to charging and discharging currents; t_c and t_d refer to charging and discharging times respectively.

In this thesis, the electrochemical performance of the ZIFB single cell was carried out by the above-mentioned charge/discharge tests under galvanostatic conditions operating at 10, 20, and 40 mA·cm^{-2} using a Biologic® VMP3 potentiostat. The charge was controlled by both upper cut-off voltage (within the range of 1.6-1.7 V) or reaching 67% of theoretical capacity.

Electrochemical Impedance Spectroscopy (EIS)

EIS analysis is one of the most common technique used in RFB research to measure the series resistance of RFBs at high frequency. EIS is also performed periodically between various tests to assess the overall impedance characteristics of RFBs at different stages.[4] **Figure 2.8** explains the Nyquist impedance plot to determine the EIS resistances of a typical RFB.

In this thesis, EIS measurements were conducted at open-circuit conditions within a frequency range of 200 kHz to 100 mHz and AC perturbation of 10 mV of amplitude to investigate the series resistance (R_s) of the ZIFB cell. The results of EIS measurements have been discussed in **Chapters 3** and **4**.
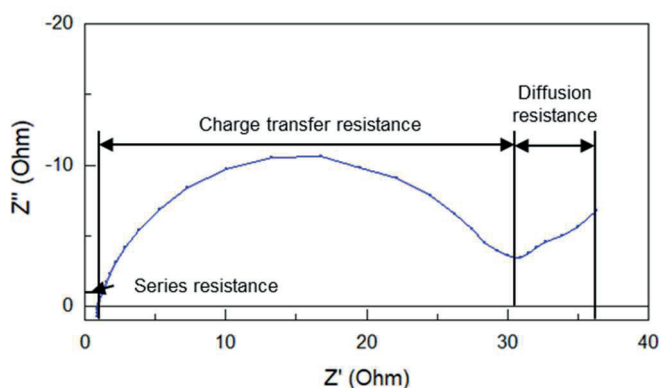
Figure 2.8. Nyquist impedance plot of a typical RFB.

In-situ EIS

In **Chapter 4** of the thesis, *in-situ* EIS is conducted to study half-cell electrolyte resistances in various SOCs.

Through this setup (discussed in **section 2.4.3**), changes in the half-cell electrolytes resistance were analysed in real-time by applying potentiostatic electrochemical impedance spectroscopy (PEIS) on charged electrolytes passing through the two auxiliary half-cells. Electrolytes were charged from 0% to 60% SOC with intervals of 15%. In between, PEIS was conducted in open-circuit conditions (OCV) within a frequency range of 200 kHz to 100 mHz and AC perturbation of 10 mV of amplitude at electrolytes of 0%, 15%, 30%, 45%, and 60% SOC respectively. The complete measurement was carried out at the 1st charging cycle of the ZIFB single cell at the current density of 10 mA·cm^{-2}.

Current-interrupt method

Current-interrupt method (**figure 2.9**), commonly applied in fuel cells, is based on the transient voltage response after current interruption i.e., changing from polarisation conditions (i >0) to relaxation mode (i = 0, *i.e.*, open circuit conditions) in a short time period[5].

This technique consists in following the transient potential variation from polarisation conditions (i >0) to relaxation mode (i = 0, i.e., open circuit conditions) and calculating the ohmic resistance (R_{ohm}) as a consequence of the ohmic voltage drop. The ohmic resistance can therefore be calculated as:

$$R_{ohm} = \frac{\Delta V}{i} \qquad (2.2)$$

In this thesis, the results of this technique have been discussed in **Chapters 3** and **4**.
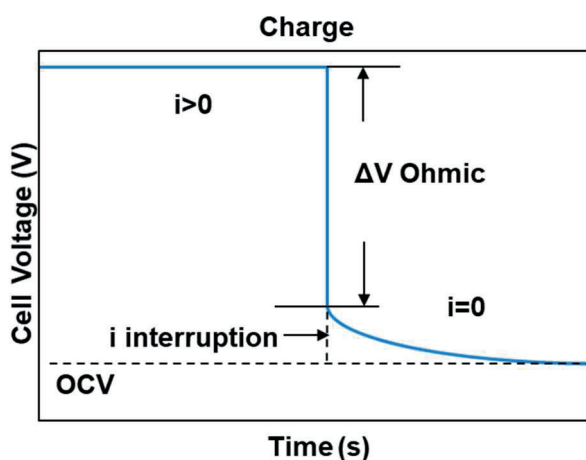
Figure 2.9. Representation of the current-interrupt method in terms of transient cell voltage.

Discharge polarisation

The discharge polarisation method (**figure 2.10**) is another useful technique to determine the maximum power density of a RFB with the desired redox couples. Apart from that, this technique gives information about the three major polarisation regions, which are activation, ohmic, and concentration polarisations according to the dominant reason for voltage loss with the increase in discharge current density in an operating RFB. The most practiced ways to reduce these losses will be discussed in the next section (**section 2.2)** in ¨Operating cell voltage¨ paragraph.

In this thesis, this method has applied in the work in **Chapter 5**.
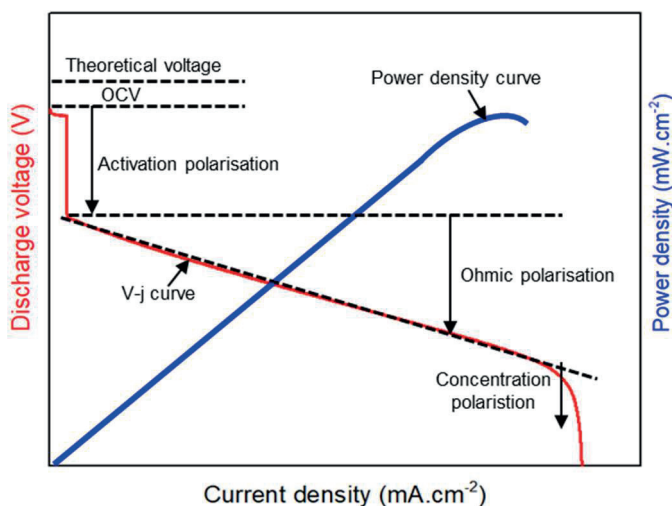
Figure 2.10. Typical discharge polarisation curve of a RFB.

2.3.2   Figures of merit of RFBs

The electrical performance of RFBs is evaluated based on several parameters and can be measured by the following equations.

- **Cell voltage,** E_{cell} **(V)** The total difference in electrochemical potential between the chemical states of the active elements on the two sides of the electrochemical cell determines the electromotive force (emf or voltage). Generally, the cell voltage (E_{cell}) is the difference in potential between the two half-cells, given by the Nernst equation. For flow batteries, it is reasonable to approximate activities with the concentrations, so **Eq. 2.3** is usually used (here for the reduction $O + ne^- \rightarrow R$):

$$E = E^0 + \frac{RT}{nF}.\ln\frac{[C_O^*]}{[C_R^*]} \qquad (2.3)$$

Where E^0 is the standard electrode potential (under standard conditions of 1 M of effective concentration, 1 bar pressure, and at ambient temperature of 298.15 K), while $\frac{C_o^*}{C_R^*}$ is the ratio between the bulk concentrations of the oxidised and reduced species. The cell voltage for the reaction $C_o + ne^- + A_R \rightarrow C_R + A_O + ne^-$ is then given by:

$$E_{cell} = \Delta E^0 - \frac{RT}{nF}.\ln\frac{[A_0][C_R]}{[C_0][A_R]} \qquad (2.4)$$

Where ΔE^0 is the difference in standard potential for the two compounds, while the ratio $\frac{[A_0][C_R]}{[C_0][A_R]}$ is the reaction quotient containing the active concentrations (denoted by square brackets) of redox couples in the anolyte and catholyte in both reduced and oxidised states.

- **Operating cell voltage,** in practical systems, the actual cell potential during charge is higher and lower during discharge than the theoretical cell potential due to the internal loss of the cell. Several factors are responsible for the internal loss such as activation polarisation, concentration polarisation, and ohmic potential drop. The overall cell potential can be described at any moment during the operation of the cell as follows:

$$E_{cell} = E^+ - E^- + \eta^+ - \eta^- - iR_{cell} \quad (2.5)$$

Where E^+ is the positive half-cell potential during charge, E^- is the negative half-cell potential during charge, η^- is the activation overpotential for the negative half-cell reactions [V], η^+ is the concentration overpotential at the positive half-cell reactions [V], i is the current density [A·cm^{-2}] and R_{cell} is the ohmic resistance of the cell [Ω·cm^2].

The internal loss impacts the overall voltage and energy efficiency of the battery during charge-discharge cycling. Therefore, it is necessary to reduce all of the voltage losses to improve overall energy efficiency. Minimisation of ohmic losses depends on the selection of membrane and electrode materials with low electrical resistance, reduction of internal spaces or components, and minimising contact resistances. Activation overpotential losses could be reduced by using electrode materials with good electrocatalytic properties, while concentration overpotential could be reduced by introducing mass transfer enhanced electrodes, increasing flow rates, and improving the electrolyte flow distributions.[6] Besides, the materials/components selections for cell assembling, and efficient cell design are equally important for improving the overall performance of RFB.

- **Volumetric capacity, C (Ah·L⁻¹)** of the electrolyte indicates the amount of charge that can be stored in a certain amount of electrolyte based on the specific redox-active material. It is dependent on the amount of redox-active material, number of electrons that participate in the redox process. It is calculated from the following formula:

$$C = \frac{m.n.F}{M.V} \qquad (2.6)$$

- **Energy density, ED** and **Power density, PD**

  Energy density and power density are two of the most important characteristics of an energy storage system. Energy density is limited by the solubility of ions in the electrolyte solutions. Thanks to the unique nature of RFBs to allow for independent scale-up of power and capacity since the chemical species are stored outside the cell. Therefore, higher capacity systems are more efficient with enhanced energy density.

  The power each cell generates depends on the current density and voltage. Material innovations in the electrodes and membrane have the potential to significantly reduce the internal resistance of the cell thus operating at higher current densities. Using a thinner membrane while maintaining ion selectivity has enabled some redox flow cells to achieve higher current densities and a promising total output power.[7] Thus, energy and power density are a primary weakness of flow batteries, and an area which future research has significant potential to improve.

  Energy density, ED (Wh·L⁻¹) is calculated from volumetric capacity C (Ah·L⁻¹) and the voltage:

$$ED = C.E_{cell} = \frac{m.n.F}{M.V}.E_{cell} \qquad (2.7)$$

  m = mass, n = number of electrons, F = Faraday´s constant, M = molar mass, V = volume.

  Power density, PD (mW·cm⁻²) is calculated from the current density (mA·cm⁻²) (referred to the membrane area of the RFB cell) multiplied by the operating voltage.

- **Coulombic efficiency (CE)**, defines as the discharge capacity divided by the charge capacity of the same charge/discharge cycle as:

$$CE = \frac{Q_D}{Q_c} \qquad (2.8)$$

41

CE <99% indicates crossover of the redox-active material through the membrane into the opposite half-cell or an irreversible side reaction of the redox couple or water splitting reactions e.g. oxygen or hydrogen formation.

- **Voltage efficiency (VE)**, is the ratio between the mean discharging and charging voltage,

$$VE = \frac{\bar{E}_D}{\bar{E}_C} \qquad (2.9)$$

The VE decreases as the current density increases. The multiplication of CE by VE yields the energy efficiency (EE),

$$EE = CE.VE \qquad (2.10)$$

C = charging, D = discharging, Q = charge, and E = voltage[8].

EE values are usually between 50-90%, depending on the current density, which is correspondingly dependent on several parameters such as the electrochemical kinetics, the conductivity of the electrolyte, membrane, and cell resistance.

The electrolyte utilisation was defined as the ratio between the capacity attained during discharge ($Q_{discharge}$) and the maximum theoretical capacity ($Q_{theoretica}$) according to the concentration and volume of active species in the electrolyte in both compartments.

2.3.3 Half-cell based electrochemical characterisation

Electrodeposition

Electrodeposition is a powerful technique for growing high-quality film/layers based on the occurrence of electrochemical redox reactions at the electrode|electrolyte interface.[9] Metal electrodeposition is a widely employed technique in which metal is reduced on the electrode surface.[10] Deposition occurs in two steps: (a) nucleation followed by (b) growth of the formed nuclei, and generates a conformal deposit of the material. Both, the applied current and potential are critical parameters that determine not only the amount deposited but also the stoichiometry and composition of the film.[11]

In **Chapters 3** and **5** of this thesis, the results of the electrodeposition measurements are discussed. The experimental details are briefed here:

Chapter 3:

The zinc electrodeposition tests were done in a three-electrode cell. G-felt, C-paper, or G-foil anodes of 1 cm^2 area were used as working electrodes, platinum mesh as the counter electrode, and Hg/Hg$_2$SO$_4$ as the reference electrode. The total charge was applied of about 193 C·cm^{-2} under current densities of 10 and 20 mA·cm^{-2}.

Chapter 5:

The zinc electrodeposition tests were done in a two-electrode connection using FTO (Aldrich, surface resistivity of ~13 Ω/sq) of 1 cm^2 area as working and platinum mesh as counter/reference electrodes respectively. About 54 C·cm^{-2} of total charge was applied at a current density of 20 mA·cm^{-2}.

Cyclic voltammetry (CV)

The electrochemical properties of redox couples are typically studied by cyclic voltammetry (CV), a very popular technique for obtaining initial electrochemical information about a new system.[12] CV is performed using a 3-electrode set up with a working electrode, a reference electrode, and a counter electrode. CV is first performed in a wide voltage range within the stable voltage window of the solvent to find possible redox peaks (**figure 2.11**) and then switched to a narrow voltage range to study the individual positive and negative redox reactions. By varying the CV scan rates, the kinetics property (D: diffusion coefficient) of redox couples can also be quantitatively estimated using the Randles-Sevcik equation.[4]

In **Chapter 5** of this thesis, the results of the CV measurements are discussed. The experimental details are briefed here:

CV tests were carried out in a conventional three-electrode cell. A static glassy carbon electrode (GCE) with a diameter of 3 mm was used as a working electrode while a Hg/Hg$_2$SO$_4$ in K$_2$SO$_4$ solution (saturated) and platinum mesh served as the reference and counter electrodes respectively. 25 mM solution (ZnI$_2$:KI) without and with NaCl was used for the CV test at the scan rate ranging between 10 to 50 mV·s^{-1}. On the negative side half-cell, a potential sweep between -0.8 V to -2.05 V vs Hg/Hg$_2$SO$_4$ (forward and reverse scan) was carried out to reduce Zn^{2+} and oxidize metallic Zn (s) at the surface of the GCE. On the positive side half-cell, forward, and reverse sweep was carried out between -0.8 V to 0.5 V vs Hg/Hg$_2$SO$_4$ to oxidize I$^-$ and reduce I$_3^-$ respectively. The diffusion coefficient associated with I$^-$ oxidation and I$_3^-$ reduction reactions were calculated by applying the Randles-Sevcik method as per the following equation:[13]

$$i_p = 0.4463 \, nFAc_0 \left(\frac{nFvD}{RT}\right)^{1/2} \qquad (2.11)$$

Where i$_p$ is peak current (A), F is Faraday constant (C·mol^{-1}), T is temperature (K), n is the number of electrons (n=2), A is the electrode surface area (0.07 cm^2), c$_0$ is the bulk concentration of active species (mol·L^{-1}), v is the scan rate (v·s^{-1}) and D is the diffusion coefficient (cm^2·s^{-1}). Using the slopes of the fitted linear Randles-Sevcik plots, the diffusion coefficient was calculated.
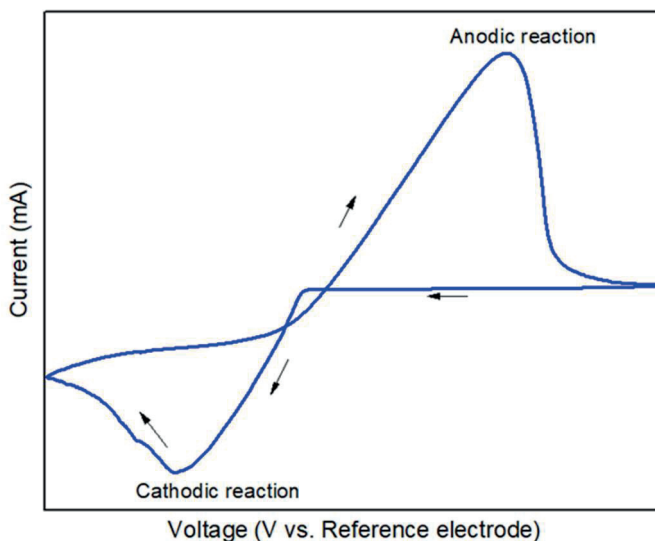
Figure 2.11. Variation of current as a function of potential in a cyclic voltammogram.

2.3.4 SRFB characterisation

J-V curve analysis

The most important characterisation for a solar cell is linear scan voltammetry (LSV) in two-electrode mode under calibrated illumination (**figure 2.12a**) to evaluate their open circuit voltage (V_{oc}), short circuit current density (J_{sc}), fill factor (FF), power conversion efficiency and maximum power point (MPP) (the corresponding equations are mentioned in **Eq. 2.12** and **2.13**).

Cycling test of SRFB

To perform cycling tests of SRFB, two potentiostat channels are needed (**figure 2.12b**). Channel 1 is configured under the RFB mode to monitor the battery potential and channel 2 is configured under the photocharge mode to monitor the photocurrent. During the photocharging process, channel 1 is set to open circuit to measure the battery OCV and channel 2 is set to short circuit to measure the photocurrent generated by the solar cell under simulated illumination. The charging process can either have a time limit and/or a cell voltage cut-off to control the capacity utilisation range. However, due to the possible decay of the photocurrent with time and higher SOC%, setting time limit only is not effective specially for long-term cycling tests. Hence, setting upper voltage limits in Channel 1 during photocharging process is preferred. During discharge, illumination is stopped, and channel 1 is set to open circuit which then holds the charged voltage of the battery. Next, the galvanostatic discharge could be performed with only a single channel setting a lower voltage limit, the same as the process for discharging normal RFB. After cycling tests, CE, VE, and

EE can be calculated based on the equations described in **section 2.3.5** (**Eq. 2.14 – 2.16**).
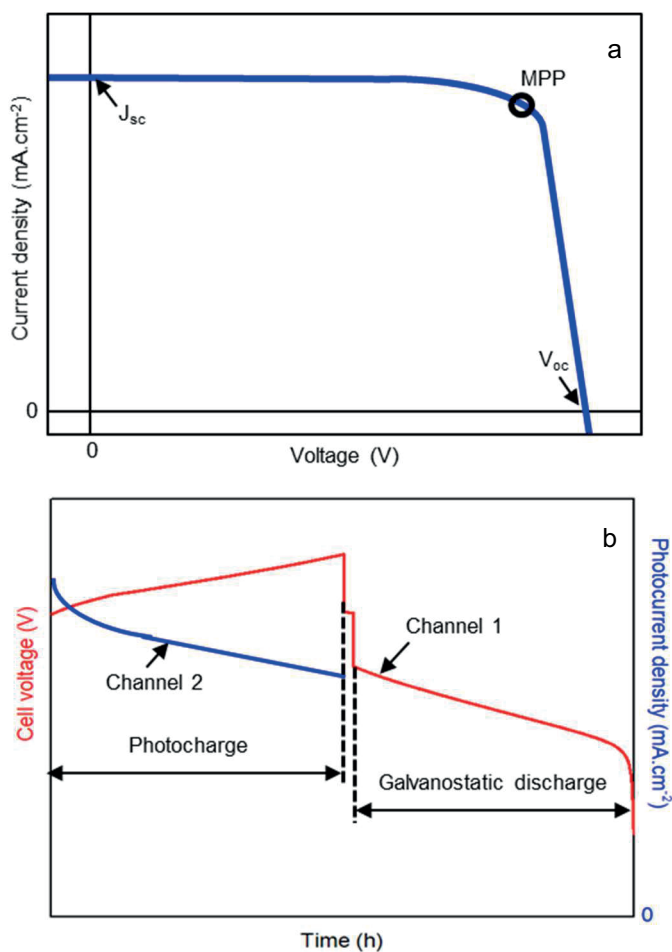
Figure 2.12. Basic characterisations in SRFB (a) J-V curve of a PV cell and (b) SRFB cycling profile.

A note to the reader:

Part II (**Chapters 6** and **7**) of the thesis are dedicated to the SRFB study. The details about the experimental conditions/parameters and results of the SRFB experiments are discussed in those chapters.

2.3.5 Figures of merit of SRFBs

To elucidate and define the performance of SRFBs, we briefly introduce the prerequisite parameters.

Efficiency calculation of solar cell:

The fill factor (FF) and the solar cell efficiency (η) of the photovoltaic cell are estimated according to the following equations:

$$FF = \frac{I_{max}V_{max}}{I_{sc}V_{oc}} \quad (2.12)$$

$$\eta = \frac{V_{oc}I_{sc}FF}{P_{in}} \quad (2.13)$$

Where, I_{max} and V_{max} are the photocurrent and photovoltage at the maximum power point, V_{oc} and I_{sc} are the open-circuit voltage and the short circuit current, respectively, and P_{in} is the incident solar power.

Efficiency calculation of SRFB:

On the other hand, SRFB efficiencies are determined from the (photo) charge/discharge curves. Coulombic efficiency (CE), voltage efficiency (VE), and energy efficiency (EE) are calculated using the following equations:

$$CE = \frac{Q_{discharge}}{Q_{photocharge}} = \frac{\int i_{discharg} \, dt}{\int i_{photocharg} \, dt} \quad (2.14)$$

$$VE = \frac{V_{discharge}}{V_{photocharge}} \quad (2.15)$$

$$EE = CE.VE \quad (2.16)$$

Herein, $Q_{discharge}$ and $Q_{photocharg}$ represent the discharge capacity and photocharge capacity, respectively. $i_{discharge}$ and $i_{photocharge}$ are the discharge current and photocharge current respectively. $V_{discharg}$ and $V_{photocharge}$ stand for the voltage of discharge and photocharge. It is important to mention that as in the photocharge the phtotocurrent density is variable with time, while in the galvanostatic discharge it is constant, the calculation of VE is not very straightforward like conventional RFB.

A solar-to-charge efficiency (η_{STC}) was calculated as the ratio between the energy stored and the incident energy during the photocharge. The instantaneous η_{STC} changes with the SOC and a general expression can be found in the following equation:

$$\eta_{STC} = \frac{E_{charge}}{E_{in}} = \frac{Q_{photocharg} \, V_{photocharge}}{AP_{hv}t} x100\% \quad (2.17)$$

Where $Q_{photocharge}$ is the battery capacity during photocharge (mA·h), $V_{photocharg}$ is the average charge voltage (V), A is the area of the photovoltaic module (cm²), P_{hv} is the incident illumination power density (mW·cm⁻²) and t is the charge time (h).

The overall round-trip energy conversion efficiency (η_{RT}) can be expressed as the ratio between the total energy extracted from the system and the energy supplied during charge (i.e. incident photon energy) and can be calculated as expressed in the following equation:

$$\eta_{RT} = \frac{E_{out}}{E_{in}} = \frac{Q_{discharge}V_{discharg}}{AP_{h\nu}t} x100\% \qquad (2.18)$$

Where, $Q_{discharg}$ is the battery capacity during discharge (mA·h) and $V_{discharg}$ is the average discharge voltage (V).

A note to the reader:

The section of various electrochemical characterisation methods ends here. Those above-detailed methods were mostly performed in this thesis. The results and related discussions have detailed in the corresponding chapters (**Chapter 3** – **7**). Few techniques which were specifically used in a certain chapter, discussed only in that corresponding chapter.

2.4 Ex-situ physicochemical characterisation

X-ray Diffraction (XRD)

XRD is a powerful technique to identify crystal structure, including the lattice parameters (a, b, c, α, β, γ) and the spacing between lattice parameters (hkl Miller indices). The technique is based on the X-ray diffraction phenomenon: when an incident X-ray beam interacts with an ordered crystal, constructive and non-constructive interferences between the scattered rays are generated, as the distance between the scattering centres is of the same order of magnitude as the wavelength of the incident radiation. This generates a diffraction pattern that is characteristic of every crystalline compound.[11]

In **Chapters 3** and **5** of this thesis, the results of the XRD measurements of electrodeposited zinc on the anodes are discussed. The common experimental details are:

Structural analysis with XRD was performed by using a Bruker D8 Advance diffractometer equipped with a Cu Kα radiation (0.15417 nm) source, a LYNXEYE super speed detector, and a Ni filter.

Figure 2.13. Picture of the XRD D8 Advance Bruker at IREC facilities.[6]

Scanning electron microscopy (SEM)

SEM method allows for unveiling the morphology (and composition) of the samples. They can determine the morphology (shape and size of the nano or microstructure). Elemental composition can also be obtained simultaneously with adequate equipment such as energy dispersive X-ray spectroscopy (EDX). SEM technique operates with secondary and backscattered electrons. While secondary electron detection allows for the inspection of the morphology and topography of the sample, backscattered electrons are adequate for analysing differences in composition. After interacting with the atoms of the sample, these electrons emerge with energies between zero and the energy of the incident electrons. Secondary electrons are those emitted with energies below 50 eV and arise from the surface region of the sample. Backscattered electrons have energies above 50 eV and they interact with deeper atoms in the sample. They are sensitive to the atomic weight of the elements in the sample; the higher they are, the brighter the image appears.[11,12]

In **Chapters 3** and **5** of this thesis, the results of the SEM measurements of electrodeposited zinc on the anodes are discussed. The common experimental details are:

The morphology and nanostructure of zinc layer on anodes are characterised by Zeiss Auriga 60 field emission scanning electron microscope (FE-SEM) with an acceleration voltage of 5 kV.

Figure 2.14. Picture of the SEM Zeiss Serie Auriga FESEM at IREC facilities.[6]

Sessile drop/Contact angle

The sessile drop method is often used to make direct measurements of the contact angle to determine preferential wetting behaviour of a solid substrate by the drop of a liquid, mostly water. In the sessile drop measurement, when a liquid droplet is placed on top of a substrate, two possibilities could occur thereafter: (1) the droplet quickly finds a static shape and stays on the surface, or (2) in the case of a porous substrate, the droplet can be wicked (totally or partially) by the substrate. It is assumed that, in the time frame of these events, evaporation is negligible, which is a realistic approximation if the droplet is not too small and volatile liquids such as hexane are avoided.[14] In **figure 2.15**, the wetting behaviour of liquid electrolyte with sessile drops plus contact angles are shown. High wettability with good adhesion (hydrophilicity-**figure 2.15b**) is demonstrated by a contact angle less than 90º while poor wettability and adhesion (hydrophobicity-**figure 2.15c**) can be obtained for a contact angle greater than 90º and less than 180º. Surface tension and viscosity define electrolyte wettability. Equilibrium contact angle and surface roughness are the parameters that affect wetting properties.[15]

In **Chapter 3** of this thesis, sessile drop measurements are discussed. Below are the experimental details:

Sessile drop technique (dataphysics instruments, model no. TBU90E) was performed to understand the wetting behaviour of the electrolyte on the different carbon-based anode surfaces. 10 µL of the droplet was applied.
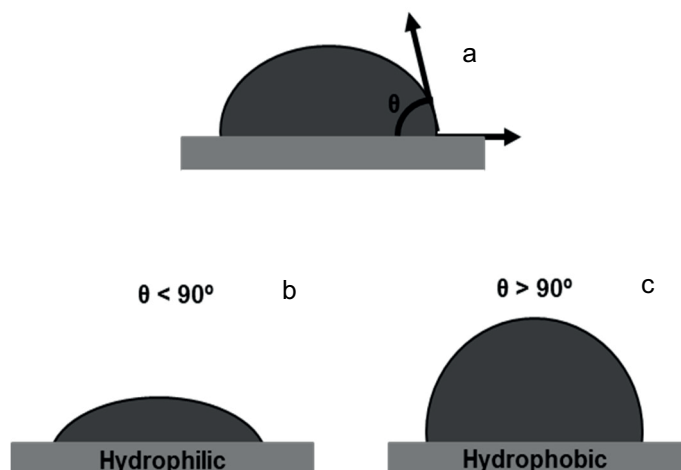
Figure 2.15 Schematic illustration of (a) sessile drop technique with the contact angle (θ). Sketch of a droplet on (b) a hydrophilic and (c) a hydrophobic surface.

Raman spectroscopy

Raman spectroscopy is one of the most commonly used non-destructive, non-electrochemical tool in the chemistry field, which provides information about the elemental composition, molecular structure, and crystallinity of a sample. Raman scattering experiments usually involve the excitation of a sample with light that is not absorbed by the sample. Most of this light passes directly through the system or is elastically scattered; it is scattered without a change in photon energy (Rayleigh effect). However, some photons exchange energy with the sample and are inelastically scattered, with a change in wavelength reflecting the loss or gain in energy. This process is called the Raman effect. Raman spectroscopy provides molecular vibrational information complementing that of IR spectroscopy. Because it is carried out with excitation and detection in the visible region of the spectrum, it can be employed in electrochemical cells with glass windows and aqueous solutions,[12] as well as in solid samples to study the degree of crystallinity.

In **Chapters 3** and **5** of this thesis, the results of the Raman measurements have discussed. The experimental details are:

Chapter 3:

To understand the graphitic structural properties of different carbon-based anodes, Raman spectroscopy measurements were carried out by using Horiba Scientific Superhead iHR320 spectrometer equipped with a 532 nm excitation laser source.

Chapter 5:

To get an insight into the complex formation after the introduction of the supporting electrolyte to the main electrolyte solution, Raman spectroscopy measurements were conducted in the backscattering configuration through an optical probe connected to Horiba Jobin-Yvon FHR640 monochromator coupled with a CCD detector. The solid-state laser (532 nm) was used as an excitation source, and the laser power was kept at ~140 $W \cdot cm^{-2}$. The spectral position was corrected by imposing the main peak of monocrystalline Si to 520 cm^{-1}.

2

2.5 References

1. C. Xie, Y. Liu, W. Lu, H. Zhang, and X. Li, *Energy Environ. Sci.*, **12**, 1834–1839 (2019).

2. B. Li, Z. Nie, M. Vijayakumar, G. Li, J. Liu, V. Sprenkle and W. Wang, *Nat. Commun.*, **6**, 1–8 (2015).

3. M-A. Goulet; M. J. Aziz, *J. Electrochem. Soc.*, **165**, A1466 (2018).

4. W. Li and S. Jin, *Acc. Chem. Res.* (2020).

5. Y. A. Gandomi, D. S. Aaron, J. R. Houser, M. C. Daugherty, J. T. Clement, A. M. Pezeshki, T. Y. Ertugrul, D. P. Moseley, and M. M. Mench, *J. Electrochem. Soc.*, **165**, A970–A1010 (2018).

6. F. J. Vázquez Galván, Doctoral thesis, https://www.tdx.cat/handle/10803/665610#page=1 (2019).

7. M. R. Mohamed, S. M. Sharkh, and F. C. Walsh, *5th IEEE Veh. Power Propuls. Conf. VPPC '09*, 551–557 (2009).

8. J. Winsberg, T. Hagemann, T. Janoschka, M. D. Hager, and U. S. Schubert, *Angew. Chemie - Int. Ed.*, **56**, 686–711 (2017).

9. G. Hopg and R. M. Penner, *Chapter 16: Metal Deposition*, p. 661–676, Elsevier B.V.

10. L. P. Bicelli, B. Bozzini, C. Mele, and L. D'Urzo, *Int. J. Electrochem. Sci.*, **3**, 356–408 (2008).

11. M. I. D. GARCÍA, Doctoral thesis, https://rua.ua.es/dspace/handle/10045/74451 (2017).

12. A. J. Bard and L. R. Faulkner, *Electrochemical methods: Fundamentals and Applications*, (2001).

13. G. Denuault, M. Sosna, and K. J. Williams, *Chapter 11: Classical experiments*, p. 431–469, Elsevier B.V., (2007).

14. A. Forner-Cenca, Doctoral thesis, https://doi.org/10.3929/ethz-a-010811344 (2016).

15. S. Hosseini, A. Abbasi, L-O. Uginet, N. Haustraete, S. Praserthdam, T. Yonezawa, and S. Kheawhom, *Sci. Rep.*, **9**, 1–12 (2019).

Thesis: Part I

Electrochemical performance evaluation of ZIFB

Chapter 3

Optimisation of anode materials
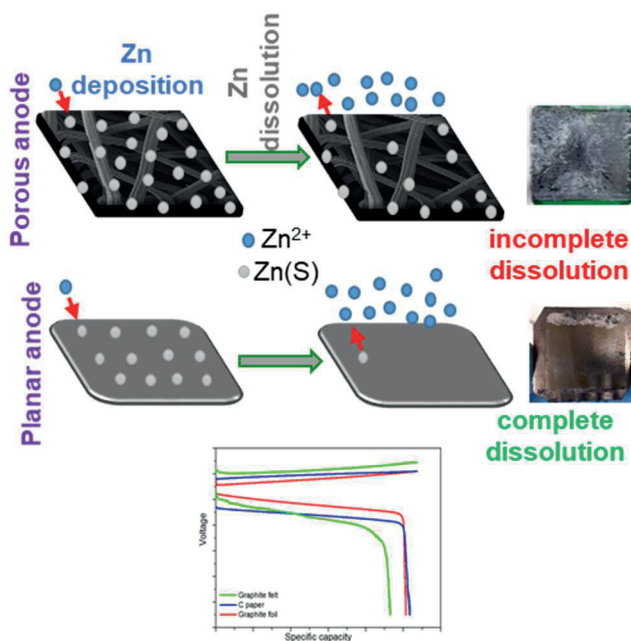
The main parts of this chapter have been published in Journal of the electrochemical society as ¨Structural Influence of the Anode Materials towards Efficient Zn Deposition/Dissolution in Aqueous Zn-Iodide Flow Batteries¨ by Monalisa Chakraborty, Sebastián Murcia-López, Joan Ramón Morante, and Teresa Andreu (Journal of The Electrochemical Society, 2021 168 040532).

The published text and figures have been marginally edited and reorganized for this thesis chapter, and parts of the introduction and experimental part were omitted as that was already introduced in the general introduction (Chapter 1) and experimental methods (Chapter 2) chapters. Additional figures from the Supporting information of the article have been included in the chapter.

3

3.1 Publication abstract

Zinc-iodide flow battery (ZIFB) is one of the best potential candidates for future grid-scale energy storage, due to its eye-catching features of benign, high energy density, and non-corrosive nature. However major investigations have not been done yet on the negative electrode of this battery where the Zn deposition/dissolution mechanism takes place, which may have an impact on the battery performance. Herein, we have reported a comparative study of different carbon-based anodes which are conventional graphite felt, carbon paper, and graphite foil. Single-cell charge/discharge performances among these three different anodes depict that the cell with planar, hydrophilic graphite foil anode is showing the best energy efficiency and the lowest cell resistance among the carbonaceous electrodes. Zn dissolution process during discharge seems to be the bottleneck for having a stable cell, which was corroborated by the use of a Zn foil anode that shows excellent efficiencies along the successive cycles.

3.2 Introduction

3.2.1 Scope of our work based on the current state of the art

The general working scheme, literature reviews, backlogs, and open questions related to ZIFB have already been discussed in **Chapter 1 section 1.3.2**. So far studies on aqueous Zn-I$^-$ batteries have been mainly focused on improving cathode materials, I$^-$/I$_3^-$ redox chemistry, design of a single flow battery without the use of cation exchange membrane.[1–9] Few investigations have been done so far on the impact of Zn plating/stripping on cell electrochemical performance. Lu et al. worked on nitrogen and sulfur-doped 3D porous graphene foams as both cathode and anode which enable rapid ion transport as well as a reversible Zn plating/stripping process in anode.[10] Chamoun et al. demonstrated that electrochemically synthesised hyper-dendritic nanoporous Zn foam anode exhibits excellent capacity retention over 100 cycles which could be helpful for Zn-based rechargeable batteries.[11] Jiang et al. reported first-principle calculations of Zn adsorption mechanism on carbon surfaces and found that by modifying the carbon surface by creating single vacancies it is possible to achieve uniform Zn deposition on graphite felt electrode.[12] Hosseini et al. recently reported that the addition of dimethyl sulfoxide (DMSO) as a potential additive in the anolyte of alkaline Zn-air FB, enhances Zn dissolution from the surface of the anode, which improves discharge capacity and cyclability.[13] However, so far from most of the published literature, it is clear that the negative side of the aqueous Zn-based flow batteries is a vital aspect that has been often overlooked. Whereas negative electrode plays a significant role in the cell cycling performance as Zn plating/stripping takes place during charge/discharge cycling.

3.2.2 Objectives of the chapter

Based on the points of the effective Zn deposition/dissolution to the anode surface, herein, we have carried out comparative studies of different carbon-based anodes such as conventional porous graphite felt (G-felt),[1] carbon paper (C-paper)[1] and planar graphite foil (G-foil)[1] to understand the influence of the anode materials in the ZIFB full-cell cycling performance.

Highlights of the chapter

To obtain the main objectives, the following investigations have carried out:

o   ZIFB single-cell electrochemical performance analysis to obtain a very first picture of the cell level performance of these anodes.

o   Validation of the obtained electrical performance of ZIFB with different anodes by further routine electrochemical and physicochemical investigations.

o   Half-cell electrodeposition tests following SEM characterisation to gather ideas about the change of Zn plating microstructure and morphologies based on the physical properties of the anodes.

o   Contact angle test to verify the electrolyte wettability on anodes that helped to understand the full-cell cycling of the anodes.

A note to the reader:

The `materials and methods´ related to this chapter have already been discussed in the general experimental methods chapter (**Chapter 2**). The ZIFB full-cell experiments were performed with the cell configurations detailed in **section 2.2.1** (see **table 2.1** for a quick view). The ZIFB single cell cycling was carried out up to the defined limiting SOC of 67%, which has been explained in **section 2.2.2**. Electrochemical performances of ZIFB using different carbon-based anodes were evaluated by traditional charge/discharge cycling, EIS, and current-interrupt method, for full-cell mode and electrodeposition method for half-cell mode respectively. Morphological and structural analyses of anode materials were studied by SEM, XRD, and Raman spectroscopy. Finally, electrolyte wetting behaviour on these anodes was assessed by the sessile drop technique. The experimental settings and parameters of all these above-mentioned techniques implemented in this chapter are thoroughly detailed in **Chapter 2.**

---

[1]These abbreviations have been directly adapted from the publication of this work. The reader could find these abbreviated words in the rest of the chapters of this thesis.

3.3 Results and discussion

3.3.1 Electrochemical performance of ZIFB with different anodes
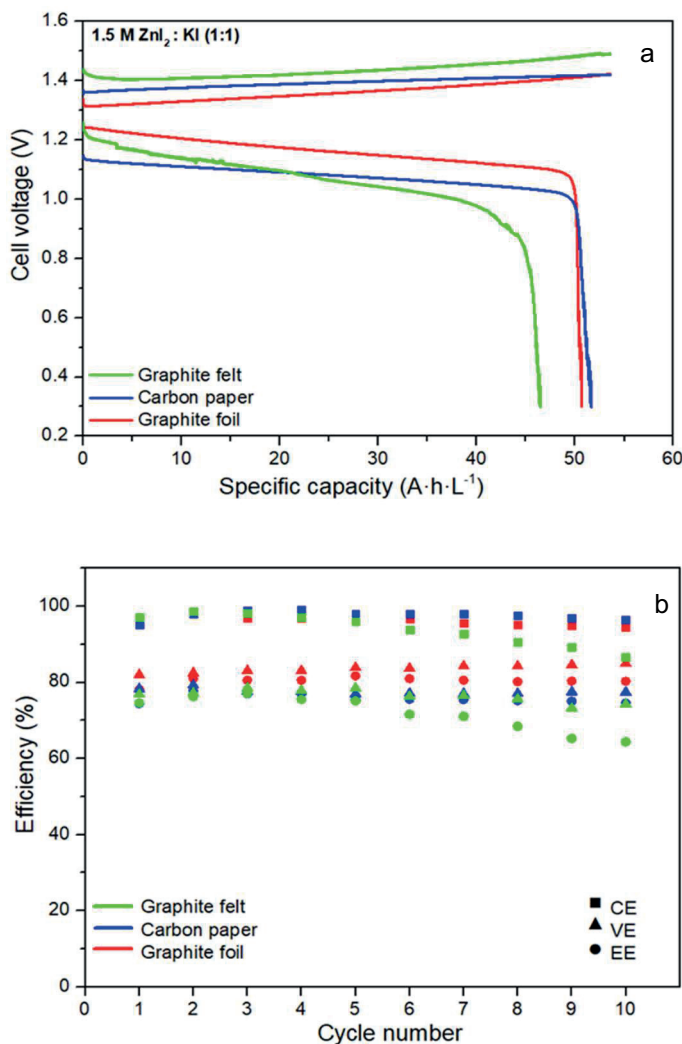
Figure 3.1. Comparison of (a) charge-discharge voltage curves of 10th cycle and (b) cycling performances for efficiencies of the full-cell of graphite felt, carbon paper, and graphite foil as anode and graphite felt as cathode at 1.5 M ZnI_2: KI (1:1) at a current density of 10 mA·cm^{-2}.

Figure 3.1a represents charge-discharge voltage curves of full-cell assembled with G-felt as the cathode and different anodes. Cycling was done with 1.5 M ZnI_2: KI (1:1) electrolyte at the current density of 10 mA·cm^{-2}.

It can be seen that the cell assembled with G-felt anode is showing the lowest discharge capacity compared to the cells assembled with C-paper and G-foil anodes. Besides, cells with G-felt and C-paper show higher internal resistances compared to

the cell with G-foil. Cycling efficiencies are shown in **figure 3.1b**. As it can be seen, CE of the cell with G-felt anode decreases gradually upon cycling which leads to EE decay, although VE does not show any significant decay. The cell using C-paper anode maintains stable performance without a steep drop in any of the efficiencies. Finally, the cell with G-foil anode exhibits excellent VE among all the three anodes. Additionally, along with approximately consistent CE values throughout the cycling period, this cell is showing the best EE compared to the other two cells in overall.

In **table 3.1** the values of ohmic resistance (R_{ohm}) estimated from the current-interrupt method at two current densities (10 and 20 mA·cm^{-2}) are summarised. These values are calculated based on the average voltage drops at the end of the charge during all the cycles and are associated to the ohmic drop after relaxation when changing from polarisation to open-circuit conditions. Similar R_{ohm} values are obtained with independence on the applied current density. In general, the G-foil exhibits the lowest ohmic resistance, associated to the lowest voltage drop after relaxation, while both G-felt and C-paper present higher values. In particular, the C-paper has the highest resistance despite its intrinsic good electrical conductivity (<0.08 Ω·cm), which can be explained by its poor wettability, as indicated later. These results agree with the obtained voltage efficiencies, which were lower and similar with the two porous electrodes along all the cycles.

Table 3.1. Comparison of ohmic resistance (R_{ohm}) from current-interrupt method during charge process at two current densities of 10 and 20 mA·cm^{-2}.

	j (mA·cm^{-2})	V1 (V)	V2 (V)	ΔV_{ohmic} (V)	R_{ohm} (Ω·cm^2)
G-felt	10	1.45 ± 0.010	1.33 ± 0.010	0.12 ± 0.004	11.60 ±0.400
	20	1.56 ± 0.040	1.34 ± 0.010	0.22 ± 0.040	11.20 ±0.300
C-paper	10	1.42 ± 0.010	1.28 ± 0.010	0.14 ± 0.001	13.60 ±0.400
	20	1.54 ± 0.005	1.30 ± 0.003	0.24 ± 0.005	12.20 ±0.400
G-foil	10	1.41 ± 0.002	1.32 ± 0.003	0.09 ± 0.002	9.40 ±0.300
	20	1.47 ± 0.003	1.30 ± 0.003	0.17 ± 0.005	8.40 ±0.300

EIS tests at OCV were carried out to investigate the series resistance (R_s) of the cell assembled with all three anodes. **Figure 3.2** depicts the Nyquist impedance plots of the ZIFB single-cell with anodes; G-felt, C-paper, and G-foil respectively in 1.5 M ZnI$_2$:KI (1:1) electrolyte. Here, R_s is the combination of electrolyte resistance, electrode resistance, and interface resistance (**figure 3.2b**). R_s is lowest in G-foil by taking into account a slight difference with C-paper, and highest in G-felt. Therefore, this R_s value could provide a preliminary statement about the electrical conductivities of these three anode materials where G-foil is showing the highest electrical conductivity.
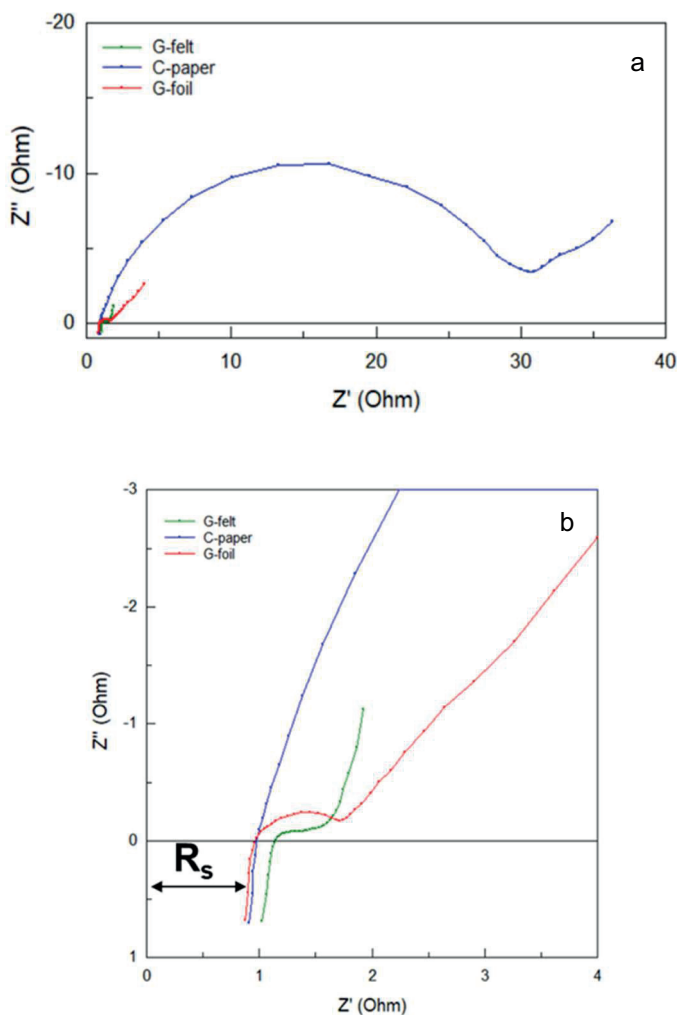
Figure 3.2. (a) Nyquist impedance plot of full-cell with G-felt, C-paper, and G-foil as respective anodes and graphite felt as cathode at 1.5 M ZnI_2: KI (1:1), (b) Enlarged plot ranging from 0 to 4 Ω.

Additionally, the XRD measurement of the cycled G-foil (**figure 3.3**) clearly shows only metallic Zn (JCPDS 041−1487) along with two peaks of weak intensities which belong to graphite (JCPDS 004-0831). Both structures belong to the hexagonal crystalline group and exhibit a certain orientation towards the [002] direction. This pattern proves that solid Zn is the only dominant product that is reversibly deposited on the G-foil anode.
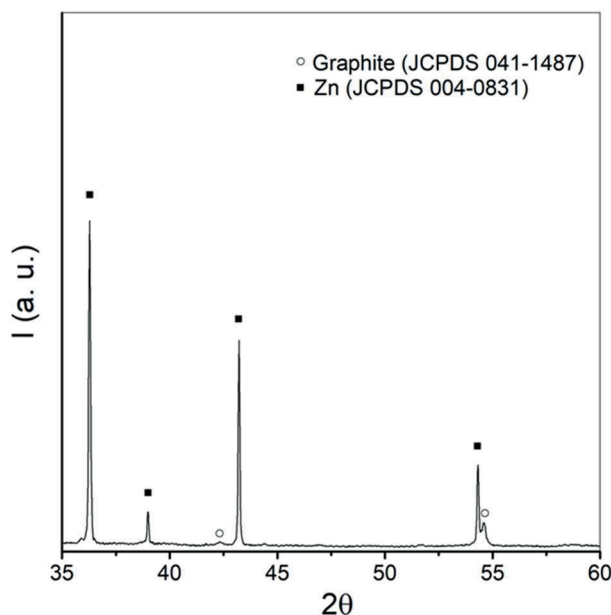
Figure 3.3. XRD pattern of the cycled G-foil anode with electrolyte 1.5 M ZnI_2:KI (1:1).

For further comparing the graphitic structures and crystalline properties of these anode materials, we performed Raman spectroscopy measurements. **Figure 3.4** illustrates the Raman spectra of G-felt (thermally-treated), C-paper, and G-foil. The first-order Raman spectrum exhibits defect/disordered (D), graphitic (G), and overtone (2D) bands at around 1340, 1575, and 2700 cm^{-1} (these bands are slightly shifted in each material), respectively. It can be seen that the intensity of the D band is higher than the G band in G-felt. This proves the presence of defects associated to sp3 hybridisation by breaking crystal symmetry (C–C stretching bond), and amorphous structure. On the other side, the C-paper spectrum exhibits G band of intensity higher than D band, which proves the tendency towards the oriented, graphitised structure. Finally, G-foil is showing a very sharp peak (G), about 4 times higher intensity than D, proving a highly graphitic structure. The graphitic peak-to-peak intensity ratios (I_D/I_G) are calculated to be 1.28, 0.28, and 0.24 for G-felt, C-paper, and G-foil, respectively. Based on these ratios, it is possible to state the degree of crystallinity. As the intensities of D to G bands are inversely proportional to the crystallinity,[15,16] hence, the graphite foil is showing the highest degree of crystallinity while G-felt exhibits a more defective structure.

Therefore, in agreement with the values presented in **table 3.1**, G-foil exhibits a higher extension of the sp2 hybridisation, which in turn might be associated to higher intrinsic electrical conductivity. Consequently, this crystalline, highly conductive nature of G-foil allows it to retain a stable CE throughout the full-cell cycling period (**figure 3.1b**). However, this does not explain the difference between this anode with the C-paper.
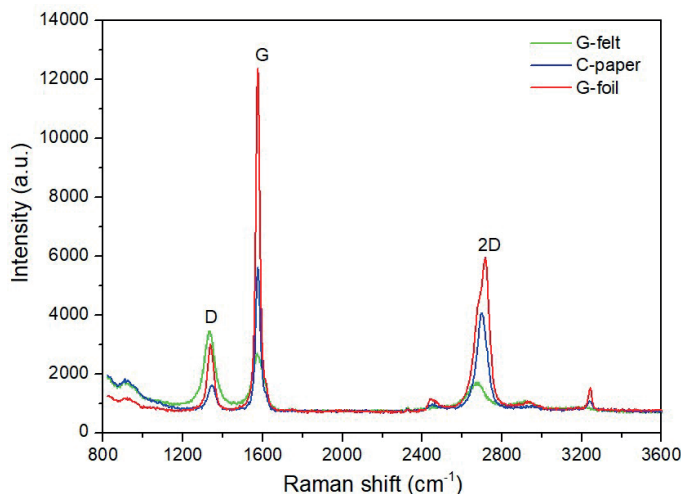
Figure 3.4. Raman spectra of different anodes.

3.3.2 Zinc plating-stripping process with different anodes

To investigate the morphology and microstructure of Zn deposition on the anode surface, we carried out the electrodeposition on three different anodes with varied physical structures: G-felt (thermally- treated), C-paper, and G-foil. An aqueous solution of 1.5 M ZnI_2:KI was used as the electrolyte. These chronopotentiometry measurements were performed up to 67% SOC which corresponds to surface charge density of 193 C·cm^{-2} at two current densities, 10 and 20 mA·cm^{-2}. In G-felt (**figure 3.5a**), all the fibers including those in the inner part of the electrode are covered with deposited Zn, as its highly porous nature allows the electrolyte to penetrate from the surface to the inner part of the substrate, leading to conformal deposition at 20 mA.cm^{-2} (**figure 3.5d**). The highly hydrophilic nature of G-felt is shown in **figure 3.6a**, where after electrolyte drop deposition the materials became immediately wet and no contact angle was formed on the surface. In the case of C-paper, the fibers seem partially covered by non-uniform and discrete deposition at 10 mA·cm^{-2} (**figure 3.5b**), and an accumulation of the Zn deposit is present mostly on the surface at higher current density (**figure 3.5e**).
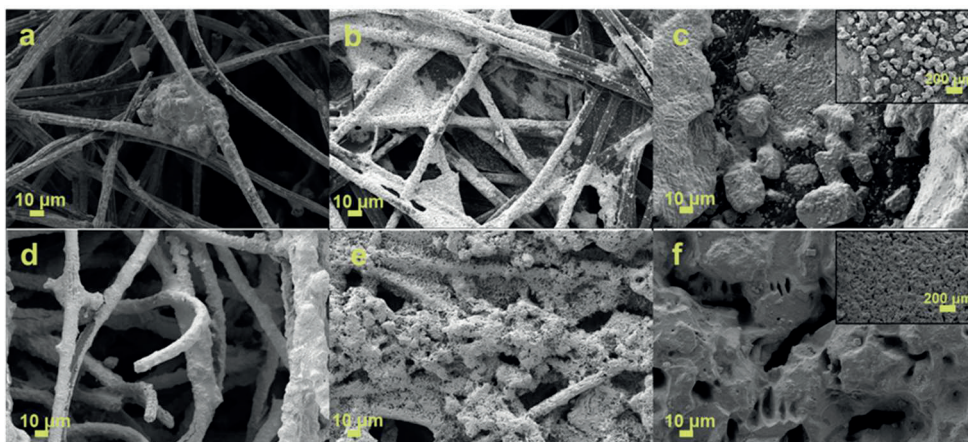
Figure 3.5. SEM images of (a) & (d) thermally-treated G-felt, (b) & (e) pristine C-paper and (c) & (f) pristine G-foil; electrodeposited at 193 C·cm^{-2} at current density of 10 mA·cm^{-2} (a)–(c) and 20 mA·cm^{-2} (d)–(f) respectively.

The difference in the deposition behaviour between the three electrodes and in particular between the two porous substrates, G-felt and C-paper, can be ascribed to many factors. Albeit both materials consist of graphitised carbon (with differences in the graphitisation degree), some differences in the functionalisation of the surface can be expected to influence the electrochemical behaviour. Additionally, the obvious distinction in the microstructure also implies that both materials possess different electrochemical surface areas. In this sense, the thicker G-felt also exhibits higher porosity (close to 90% vs 78% for the C-paper) and lower density than the C-paper (< 0.1 g·cm^{-3} for G-felt and 0.44 g·cm^{-3} for C-paper). These facts imply that the three substrates have potentially different areal capacities in the order of G-felt > C-paper > G-foil, although in the present study only the geometrical area has been considered. Moreover, the partial PTFE coating of the C-paper confers certain hydrophobic properties to this electrode with a contact angle of 137° (**figure 3.6b**), which does not allow the electrolyte to go into the bulk, and probably leads to the highest charge transfer resistance as seen in the Nyquist plot (**figure 3.2a**). The fact that C-paper has a limited wettability, introduces an additional overpotential which may explain the differences in the polarisation resistance observed in the previous section, despite its high electrical conductivity. On the other side, SEM image of charged G-foil anode at 10 mA·cm^{-2} (**figure 3.5c**) depicts identical particle-like deposition only on the surface as its planar structure does not allow electrolyte access to the bulk. G-foil is slightly hydrophilic, with a contact angle of 77° (**figure 3.6c**), and at 20 mA·cm^{-2} a much uniform and compact deposition than for C-paper, as seen in **figure 3.5f** (including inset picture at higher magnification). Overall, by comparing these three anodes it is obvious that the morphology and pattern of Zn deposition vary according to the changes in the electrode microstructure.
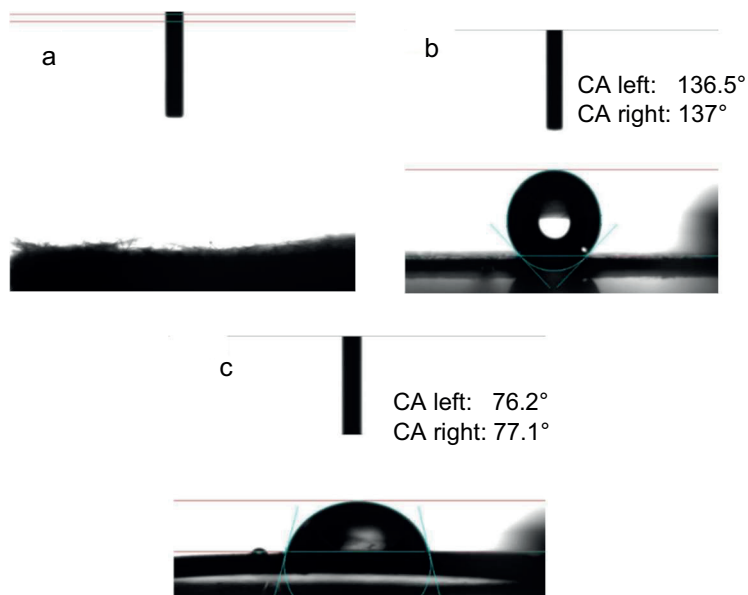
Figure 3.6. Sessile drop test of different anodes with electrolyte 1.5 M ZnI_2: KI (1:1) (a) thermally-treated G-felt, (b) C-paper, and (c) G-foil.

Concerning the discharge, the pictures of these cycled anodes (**figure 3.7**) enlighten the reason for the difference between these cells cycling performance. A high amount of remaining Zn metal deposition can be seen on the G-foil (**figure 3.7a**) which means that the dissolution of the deposited products did not happen properly. After discharge, some remaining Zn is still deposited on the current collector side (**figure 3.7i**) as well due to the porous nature of felt. This result of the improper dissolution of Zn could be correlated to the rapid capacity fading with cycling (**figure 3.1b**) due to the loss of Zn^{2+} active ions. Compared to G-felt, a few amount of un-etched Zn metal is present in the C-paper anode surface (**figure 3.7b**), whereas, in G-foil, almost no remaining deposited metallic Zn has been seen except an accumulation in the top part of the electrode which could be attributed to the effect of a non-favorable fluid hydrodynamics situation at the vicinity of the sealing gasket.
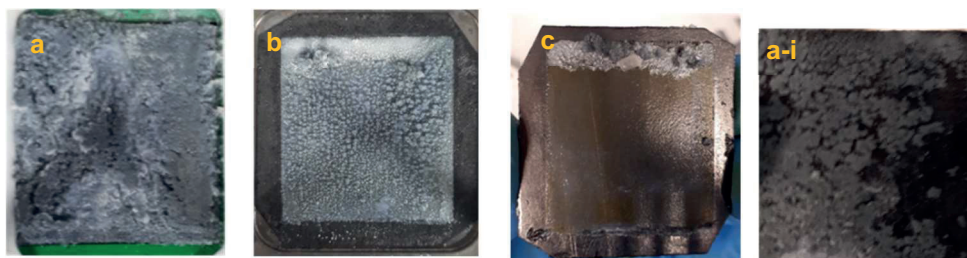

Figure 3.7. Morphologies of different anodes after 10 full cycles at current density of 10 mA·cm^{-2}; G-felt (a) membrane side (a-i) current collector side; membrane side of C-paper (b) and (c) G-foil respectively.

To sum up, we might state that observing higher discharge capacity of graphite foil is due to the uniform Zn electrodeposition and its planar nature. In brief, the nature of Zn metal deposition is crucial to factors such as the porous structure of the anode and higher applied current. As Yufit et al.[17] reported that generally in the porous electrode, for example, in G-felt, deposition starts to form from the back contact of the electrode by filling all the pores and then it grows further to the electrode surface. During the discharge process, the deposited products etch back from the electrode bulk. Higher applied current results in higher localized current gradient, which promotes inhomogeneous dissolution from bulk. Hence, in the consecutive cycles, the new products deposit over the already present, un-etched deposition. This deposited layer covers the bulk of the electrode upon cycling, which impacts the cell electrochemical performance by fading discharge capacity and overall cell efficiency (energy efficiency). The electrochemical performance of the cell assembled with G-felt anode (**figure 3.1**) and the digital images of cycled G-felt anode (**figure 3.7a, 3.7a-i**) strongly prove this statement. Whereas comparing the electrochemical full-cell performance and digital images of G-felt with the G-foil, we could state that Zn metal deposition/dissolution process occurs in an almost reversible manner in planar, graphite foil anode.

3.3.3   Electrochemical full-cell performance of Zn metal foil as anode

In order to prove that when using carbonaceous anodes "Zn dissolution" during discharge plays a vital role in the cycling performances of the cell, restricting the cell discharge capacity, we carried out the full-cell charge/discharge and cycling performances of a cell assembled with highly conductive, Zn metal foil and G-felt as anode and cathode respectively, with all other test parameters were kept the same with previous full-cell tests.

Figure 3.8a shows an excellent discharge capacity among the results shown with the carbonaceous anodes. It is clear from **figure 3.8b** that this cell is exhibiting excellent coulombic efficiency, with almost 100% capacity retention throughout the cycling, along with very well-consistent voltage and energy efficiencies. Apart from having a planar structure and high conductivity, the reason for achieving high discharge capacity might be attributed to the no shortage of redox-active Zn^{2+} ions with cycles at the anode half-cell. As the eventual deficiency of Zn^{2+} ions might happen because of the continuous and not fully reversible deposition/dissolution process, here it can be covered up by the participation of Zn metal foil as the anode. Hence, by comparing the full-cell cycling efficiencies of the cell with porous G-felt (**figure 3.1**) with this cell with Zn foil, it is clear that Zn is the limiting factor that restricts the battery to reach high discharge capacity by losing active Zn^{2+} ions in the metallic form, remaining in the electrode without etching back during the discharge process.
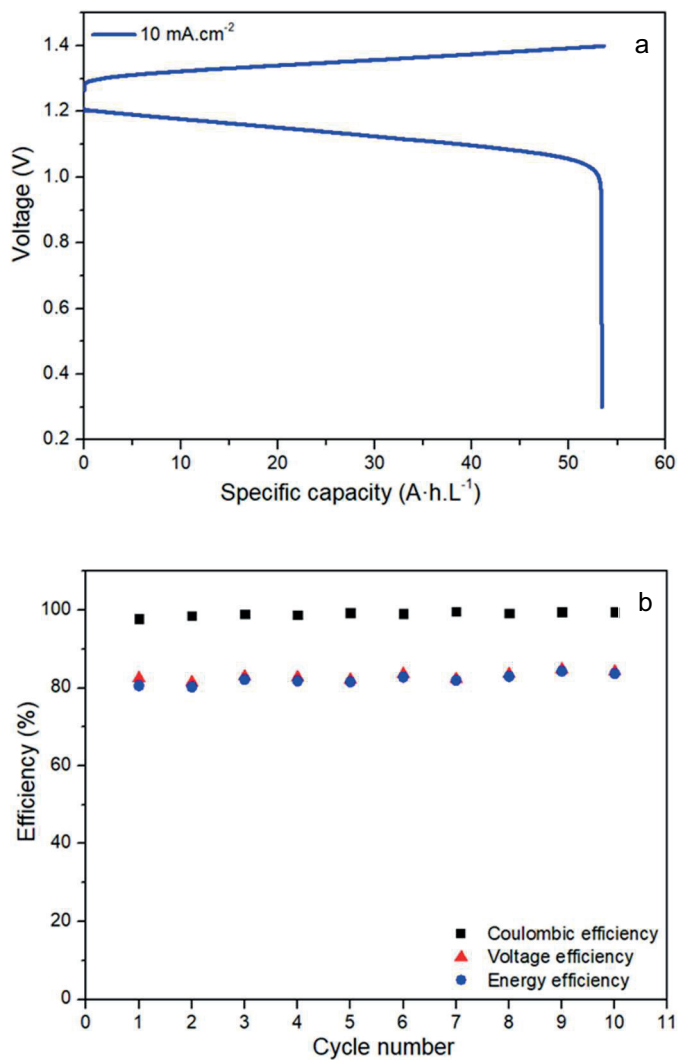
Figure 3.8. Full-cell performance of Zn foil as anode and G-felt as cathode with 1.5 M ZnI$_2$: KI (1:1) at a current density of 10 mA·cm^{-2}. (a) charge-discharge voltage curve and (b) cycling performances for efficiencies of the cell.

3.4 Conclusion

Herein, we investigated the impact of different anode materials on ZIFB electrochemical performances. We have found that in the anode material, few factors play a crucial role to achieve excellent and stable cycling efficiencies through reversible Zn metal deposition and dissolution. They are their physical structure (such as porous, and planar), electrolyte wettability, and electrical conductivity. From the full-cell electrochemical evaluation we have found that compared to porous structures such as graphite felt and carbon paper with high electrochemical surface areas associated to the different microstructures, a planar graphite foil anode exhibits the best capacity retention, due to more reversible Zn plating/stripping process, while maintaining the lowest internal resistance and consistently high-efficiency values. These results are also associated to the combined hydrophilic nature and highly graphitised structure, which ultimately guarantee high wettability and lower ohmic resistances. We obtained similar results with a Zn foil anode, proving that Zn is a limiting element affecting the cell capacity while having a porous structure is not a requirement for reaching high efficiencies.

In this work on Zn-iodide flow batteries, we have developed a statement about the influence of the structure of the anode materials towards achieving excellent full-cell electrochemical performance, which might further enlighten a path for efficient cyclability of ZIFBs by selecting the best-performed anode. Moreover, the cell potential attained during the charge with the planar electrode shows relatively low overall losses vs. the thermodynamic value (1.299 V), which lies below the practical water electrolysis voltage (>2 V). Hence, this system is a potentially excellent candidate to couple with photoelectrodes, aiming at developing next-generation solar charging batteries.

3.5 References

1. G. M. Weng, Z. Li, G. Cong, Y. Zhou, and Y. C. Lu, *Energy Environ. Sci.*, **10**, 735–741 (2017).

2. B. Li, J. Liu, Z. Nie, W. Wang, D. Reed, J. Liu, P. McGrail, and V. Sprenkle, *Nano Lett.*, **16**, 4335–4340 (2016).

3. H. Pan, B. Li, D. Mei, Z. Nie, Y. Shao, G. Li, X. S. Li, K. S. Han, K. T. Mueller, V. Sprenkle, and J. Liu, *ACS Energy Lett.*, **2**, 2674–2680 (2017).

4. C. Bai, F. Cai, L. Wang, S. Guo, X. Liu, and Z. Yuan, *Nano Res.*, **11**, 3548–3554 (2018).

5. Y. Li, L. Liu, H. Li, F. Cheng, and J. Chen, *Chem. Commun.*, **54**, 6792–6795 (2018).

6. C. Xie, H. Zhang, W. Xu, W. Wang, and X. Li, *Angew. Chemie - Int. Ed.*, **57**, 11171–11176 (2018).

7. C. Xie, Y. Liu, W. Lu, H. Zhang, and X. Li, *Energy Environ. Sci.*, **12**, 1834–1839 (2019).

8. J. Zhang, G. Jiang, P. Xu, A. G. Kashkooli, M. Mousavi, A. Yu and Z. Chen, *Energy Environ. Sci.*, **11**, 2010–2015 (2018).

9. S. Ito, M. Sugimasa, Y. Toshimitsu, A. Orita, M. Kitagawa, and M. Sakai, *Electrochim. Acta*, **319**, 164–174 (2019).

10. K. Lu, H. Zhang, B. Song, W. Pan, H. Ma, J. Zhang, *Electrochim. Acta*, **296**, 755–761 (2019).

11. M. Chamoun, B. J. Hertzberg, T. Gupta, D. Davies, S. Bhadra, B. V. Tassell, C. Erdonmez and D. A. Steingart, *NPG Asia Mater.*, **7**, e178-8 (2015).

12. H. R. Jiang, M. C. Wu, Y. X. Ren, W. Shyy, and T. S. Zhao, *Appl. Energy*, **213**, 366–374 (2018).

13. S. Hosseini, A. Abbasi, L-O. Uginet, N. Haustraete, S. Praserthdam, T. Yonezawa, and S. Kheawhom, *Sci. Rep.*, **9**, 1–12 (2019).

14. Y. A. Gandomi, D. S. Aaron, J. R. Houser, M. C. Daugherty, J. T. Clement, A. M. Pezeshki, T. Y. Ertugrul, D. P. Moseley, and M. M. Mench, *J. Electrochem. Soc.*, **165**, A970–A1010 (2018).

15. F. Tuinstra and J. L. Koenig, *J. Chem. Phys.*, **53**, 1126–1130 (1970).

16. O. A. Maslova, M. R. Ammar, G. Guimbretière, J. N. Rouzaud, and P. Simon, *Phys. Rev. B - Condens. Matter Mater. Phys.*, **86**, 1–5 (2012).

17. V. Yufit, F. Tariq, D. S. Eastwood, M. Biton, B. Wu, P. D. Lee, and N. P. Brandon, *Joule*, **3**, 485–502 (2019).

3

3

Chapter 4

Suppressing water migration by asymmetric electrolyte formulation
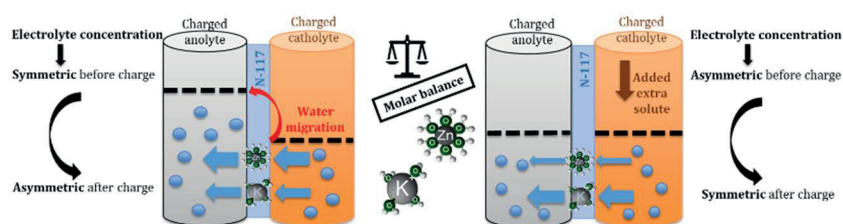
The main parts of this chapter are currently `under peer-review´ in Electrochimica Acta journal as ¨Suppressing water migration in aqueous Zn-Iodide flow batteries by asymmetric electrolyte formulation¨ by Monalisa Chakraborty, Teresa Andreu, Ben Molinari, Joan R. Morante and Sebastián Murcia-López (submitted on September 2022).

The text and figures (submitted to the journal) have been marginally edited and reorganised for this thesis chapter, and parts of the introduction and experimental part were omitted as that was already introduced in the general introduction (Chapter 1) and experimental methods (Chapter 2) chapters. Additional figures from the Supporting information of the submitted article have been included in the chapter.

4

4.1 Publication abstract

Zinc-iodide flow battery (ZIFB) is under research for the last years due to its suitability as a potential candidate for future electrochemical energy storage. During cycling, one of the biggest challenges that affect the reliable performance of ZIFB is the substantial water migration through the membrane because of differential molar concentrations of anolyte and catholyte that imbalance the osmotic pressures in each compartment. Considering the mass balances, herein we propose to equalize the total ionic concentration of electrolytes by the addition of extra solute into the compartment of lower ion concentration as a way to restrict the water crossover. Experimental validation of this electrolyte concentrations balancing strategy has been carried out by assessing the post-cycled electrolytes, and half-cell charged electrolytes, which confirms the efficient suppression of water migration from catholyte to anolyte. Besides, an in-depth analysis of ions and water transport mechanism through Nafion 117 membrane confirms that solvated K^+ ions of lower ionic radius compared to solvated Zn^{2+} ions are the dominant migrating carrier. Therefore, the addition of extra KI solute is beneficial to suppress the major transport of large hydrated Zn^{2+} ions along with the higher amount of water. Finally, the improved ZIFB cell behaviour with enhanced electrical conductivity, discharge capacity, and voltage efficiency in the cell assembled with the electrolytes of balanced molar concentrations conclude our present study, proving that tuning the electrolytes concentrations is an effective way to suppress water migration as an appealing method in the prospect of upscaling ZIFB application.

4.2 Introduction

4.2.1   Scope of our work based on the current state of the art

As per state-of-art of ZIFBs, several challenges need to be addressed before reaching their full fledge usage, such as extending battery discharge capacity following cycle life by ameliorating irreversible metallic Zn plating/stripping on the anode and suppressing water migration from one compartment to another during cycling. Different approaches have already been reported to address some of these challenges. Such as enhancing the energy efficiency by introduction of MOF-based electrocatalyst,[1] modifying electrolyte design via incorporation of bromide ions,[2] and chloride ions[3] as complexing agents, tuning the anolyte pH,[4] replacing ZnI_2 electrolyte with KI and $ZnBr_2$ along with the introduction of low-cost porous separator with self-healing mechanism from Zn dendrite growth.[5]

Water migration during cycling is a concerning issue in all flow batteries chemistries, which needs to be addressed for the prospect of capacity retention, cyclability, and long-term stability. In all-vanadium RFBs, several groups have reported this issue for the last decade. Sun and co-workers, first investigated the source of water migration in VRFBs. They have mentioned that the concentration differences of vanadium ions between positive and negative compartments are the main reason for the ion

crossover along with the water transfer driven by osmosis and electro-osmotic drag (EOD) through the Nafion proton exchange membrane.[6] Knehr et al. have presented a mathematical 2-D transient, isothermal model of a VRFB, which incorporates the species crossover as well as the transfer of water across the membrane, resulting in cell capacity loss.[7] Yan and group have demonstrated the mechanism of restricting the electrolyte volume changes by balancing the osmotic pressure via the addition of a draw solute of 2-methylimidazole in the electrolyte of a single-cell VRFB assembled with TiO_2 nanoporous membrane.[8] Oh et al. have developed a water transport model, which accounts for the various mechanisms of water and species crossover through the membrane. Further, they have validated this numerical model with experimental data and found that the water crossover via diffusion and EOD are the dominant mechanisms that cause electrolyte imbalance during cell charging/discharging.[9] Song and co-workers have studied electrolyte transfer mechanisms across a Nafion membrane based on the transport phenomena and further validated experimentally, where they found the electrolyte imbalance during cycling as the effect of viscosity, which they have optimized by manipulating the flow rate.[10]

Apart from the vanadium redox chemistry, Liu and group have addressed the water migration in alkaline Zn-Fe FBs. They have found that the water migration is the combined effect of concentration gradient, ionic strength difference on half-cell electrolytes, and the electric field. For mitigation purposes, they have studied a series of electrolyte additives and observed that Na_2SO_4 as an additive in the negative electrolyte is showing a good performance by suppressing water migration of Zn-Fe FB cell assembled with polybenzimidazole membrane.[11] Mousavi et al. have reported that differential hydraulic pressure between two sides of the microporous polyethylene separator, accelerates electrolyte transport as well as species crossover via convection, which they have optimized theoretically and experimentally by maintaining asymmetric half-cell electrolyte flow rates in a ZIFB single-cell.[12]

4.2.2 Objectives of the chapter

So far, it is clear from the literature that water migration during flow batteries operation is a serious challenge, normally overlooked, that can cause efficiency decay in long-term cycling, and hinder flow batteries from large-scale deployment. Most of the studies have been reported based on numerical water transport models to understand the transport mechanism. Few studies have been done so far on single-flow ZIFBs to restrict water transfer between compartments. For example, Xie et al. described a high-power density single-flow ZIFB by sealing the positive compartment,[13] Ito et al. reported <90% coulombic efficiency after the addition of propylene carbonate in the electrolyte, forming hydrophobic polyiodide complex during cathodic oxidation in a single-flow ZIFB without cation exchange membrane.[14]

Herein, we propose to formulate an asymmetric redox flow battery to compensate ion migration by the addition of extra solute to the catholyte as a simple strategy to restrict water migration.

Highlights of the chapter

To obtain the main objectives, the following investigations have carried out:

o   Observation of ZIFB cell post cycling electrolytes volume to assess the water transfer.

o   Calculation of electrolytes molar concentrations.

o   Evaluation of half-cell charged electrolytes resistances by *in-situ* EIS.

o   Validation of the water migration suppression strategy and comparing the improvement by evaluating the half-cell charged and post-cycled electrolytes.

o   Finally, ZIFB cell electrochemical performance comparisons between the standard and tuned electrolytes.

4.3 Materials and methods

A note to the reader:

The `materials and methods´ related to this chapter have already been discussed in the general experimental methods chapter (**Chapter 2**). The ZIFB full-cell experiments were performed with the cell configurations detailed in **section 2.2.1** (see **table 2.1** for a quick view). An aqueous solution containing a mixture of 1.5 M ZnI_2 (98.0%, Aldrich) and 1.5 M KI (99.5%, Sigma Aldrich) (1:1) was used as the standard electrolytes in both cell chambers and after the addition of extra 2 M KI in the catholyte, the electrolyte ratio was 1.5:3.5 in the catholyte chamber. The cell was connected to two glass cylinders (10 mL of electrolyte on each reservoir) to measure the volume changes of electrolytes during the charge-discharge operation. ZIFB specific cells design for *in-situ* electrochemical study has detailed in **section 2.2.3**.

The electrochemical charge-discharge test of ZIFB single cell was conducted under galvanostatic conditions, up to the defined limiting SOC of 67% which has been explained in **section 2.2.2** at current densities of 10 and 20 mA·cm^{-2} respectively. The charge was controlled by both upper cut-off voltage (1.6 V) and 67% of theoretical capacity (as mentioned in **section 2.3.1** of **Chapter 2)**. In this chapter, apart from the traditional charge-discharge analysis, the rest of the electrochemical performance comparisons of ZIFBs, without and with tuned electrolytes are evaluated by *in-situ* EIS, and the current-interrupt method (thoroughly detailed in **section 2.3.1** of **Chapter 2)**.

4.3.1 Migration of cations through Nafion CEM

Cation migration through Nafion 117 cation-exchange membrane (CEM) test was analysed by using anolyte and catholyte solutions. The ZIFB cell was charged up to 67% of theoretical capacity at 20 mA·cm^{-2} of current density. Anolyte and catholyte solutions collected at 0% and 67% SOCs of both the cases: with and without extra added 2 M KI were analyzed with ICP-OES (Perkin Elmer Optima 3200 RL) to determine the Zn^{2+} and K^+ ions concentrations. Concentrations of Zn^{2+} ions were measured at the corresponding wavelengths of 202, 206, and 213 nm, and the average value is displayed in **table 4.5**, and 766 nm of wavelength was applied to measure the concentrations of the K^+ ions.

4.4 Results and discussion

4.4.1   Electrolytes volume imbalance post cycling
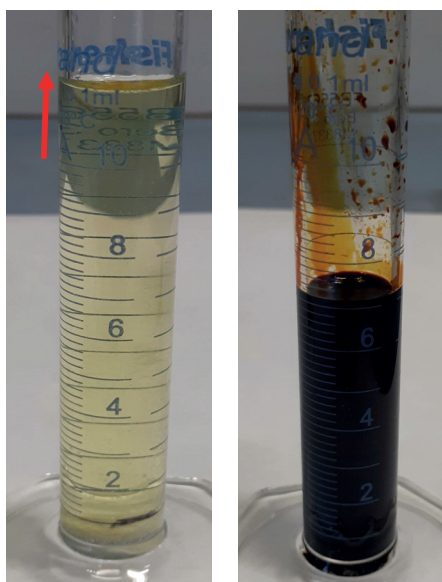
Figure 4.1. Optical images of volume variations of electrolytes (picture taken after reverse flow) after 15th cycles of the cell assembled with electrolyte of 1.5 M ZnI$_2$:KI (1:1).

In a standard redox ZIFB, both anolyte and catholyte have the same electrolyte composition. In line with our former work presented in **Chapter 3**, the standard electrolyte was an aqueous solution of 1.5 M ZnI$_2$ and KI (1:1). Upon cycling, we observed the above-mentioned (see **section 4.1.1**) water migration issue. As a representative example, in **figure 4.1** it can be seen the electrolyte volumes after 15 charge-discharge galvanostatic cycles at 20 mA·cm^{-2} of a ZIFB single cell. Considering that the initial volume at each compartment was 10 mL, the volume of the anolyte increased from the initial state while the catholyte is showing an intense reduction from the initial volume, causing an imbalance, with a partially irreversible water transfer from catholyte to anolyte upon cycling.

The reason for water transfer might be attributed to the effect of the imbalance of ionic concentrations between anolyte and catholyte compartments. As stated by several groups,[6,8–12] multiple factors such as combined effects of concentration gradient, difference in the ionic strength, hydraulic pressure, and viscosity, crucially affect water crossover through a membrane via diffusion; EOD, or osmosis mechanism. During charge, the number of free active anions and cations, I$^-$ in catholyte and Zn^{2+} in anolyte, decrease due to the formation of I$_3^-$ species and solid Zn electroplating, respectively, together with the subsequent movement of cations through the Nafion membrane to balance the charges between the two half-cells.

In our case, the anolyte and catholyte (at 0% SOC) are made up of 1.5 mol·L^{-1} ZnI$_2$ and KI (1:1), hence, having identical numbers of the total concentrations of ions of 7.5 mol·L^{-1} on both sides. During the charging process, considering electroplating of 1 mol·L^{-1} Zn^{2+} on the anode while 3 mol·L^{-1} of I$^-$ will produce 1 mol·L^{-1} I$_3^-$ on the cathode side. Consequently, at 67% SOC, the total concentration of ions is 6.5 mol·L^{-1} in anolyte and 5.5 mol·L^{-1} in catholyte. When Nafion CEM is used as the separator for ZIFB, cations (Zn^{2+} and K$^+$ along with H$^+$) are the main charge-balancing ions. Therefore, to balance the charges, based on the following electroneutrality condition in the electrolyte:

$$\sum_i z_i c_i^e = 0 \qquad (4.1)$$

respective Zn^{2+} and K$^+$ ions will migrate from catholyte to anolyte, resulting in differential ions concentrations of 8 mol·L^{-1} and 4 mol·L^{-1} in anolyte and catholyte respectively, as seen in **table 4.1**. Because of differential ions concentrations between two compartments, the water shuttle takes place from the chamber of lower ionic concentration (catholyte) to the higher ionic concentration (anolyte) via the osmosis phenomenon.

Table 4.1. Mass balance of a symmetric electrolyte formulation.

	[Zn^{2+}](M)	[K$^+$](M)	[I$^-$](M)	[I$_3^-$](M)	Charge	$\sum$[i] (M)
ANOLYTE						
0% SOC	1.5	1.5	4.5		0	7.5
67% SOC -no compensation-	0.5	1.5	4.5		-2	6.5
67% SOC -after ion migration-	1.0	2.5	4.5		0	**8.0**
CATHOLYTE						
0% SOC	1.5	1.5	4.5		0	7.5
67% SOC -no compensation-	1.5	1.5	1.5	1.0	2	5.5
67% SOC -after ion migration-	1.0	0.5	1.5	1.0	0	**4.0**

In order to further understand the real-time variations during the charge, electrolyte resistances have been measured using auxiliary cells coupled in series to the electrolyte circuit (the description of the cells have detailed in **figures 2.3-2.5** in **Chapter 2**). **Figure 4.2** represents half-cell EIS analysis of electrolytes, in the course of first charging at various SOCs (from 0% to 60% SOC). In the impedance analysis of anolyte (**figure 4.2a**) of standard electrolyte, it could be seen that charge transfer resistance (R$_{ct}$) is decreasing with an increment of SOC, from 9.56 Ω·cm^{-2} at 0% SOC to 4.62 Ω·cm^{-2} at 60% SOC (fitted from the aforementioned Randles equivalent circuit). This descending trend of R$_{ct}$ might be caused by the gradual decrement of Zn^{2+} ions concentration in the anolyte during charge which is partially compensated by K$^+$ ions perturbing the spatial double layer. On the other hand, ohmic resistance

(R_{ohm}) decreases from 0.49 $\Omega \cdot cm^{-2}$ to 0.25 $\Omega \cdot cm^{-2}$ as SOC increases from 0% to 60%. This decreasing trend could be visible in the onset enlarged plot. The decrement of R_{ohm} is equally attributed to the partial replacement of Zn^{2+} by K^+ ions with higher ionic mobility.

On the cathode side, (**figure 4.2b**) ohmic resistance (R_{ohm}) exhibits a rising trend from 0.28 $\Omega \cdot cm^{-2}$ to 0.46 $\Omega \cdot cm^{-2}$ with higher SOC, 0 to 60% respectively. As per equation 4, in the charging process, 3 moles of I^- are oxidized to produce 1 mol of I_3^- together with the cation migration to the anolyte side, limiting the number of free charge carriers, hence, increasing catholyte ohmic resistance. Concerning charge transfer resistance, upon charging it was observed a slight decrement of R_{ct} from 0.52 $\Omega \cdot cm^{-2}$ to 0.3 $\Omega \cdot cm^{-2}$. The reason for this decreasing trend might be correlated with the statement given by Jeon and co-workers, who have studied the effect of charge transfer resistance, and electrode kinetics through *in-situ* EIS analysis in the catholyte and anolyte respectively in zinc-bromine redox flow batteries. A similar reduction of R_{ct} in catholyte has been observed which is explained by the formation and further accumulation of polybromide complexes on the cathode surface. These accumulated polybromide complexes promote the electrochemical adsorption of the Br^-, hence, accelerating the overall electrode reaction and reduction of R_{ct} with increasing SOC.[15] Similar roles of $I_3^-/I_2/I^-$ halide chemistry could be hypothesized from our catholyte EIS analysis, where charged I_3^- species play a positive role in the adsorption of I^- ion at the double layer interface, facilitating the reduction of the R_{ct} at high SOC.

4

4
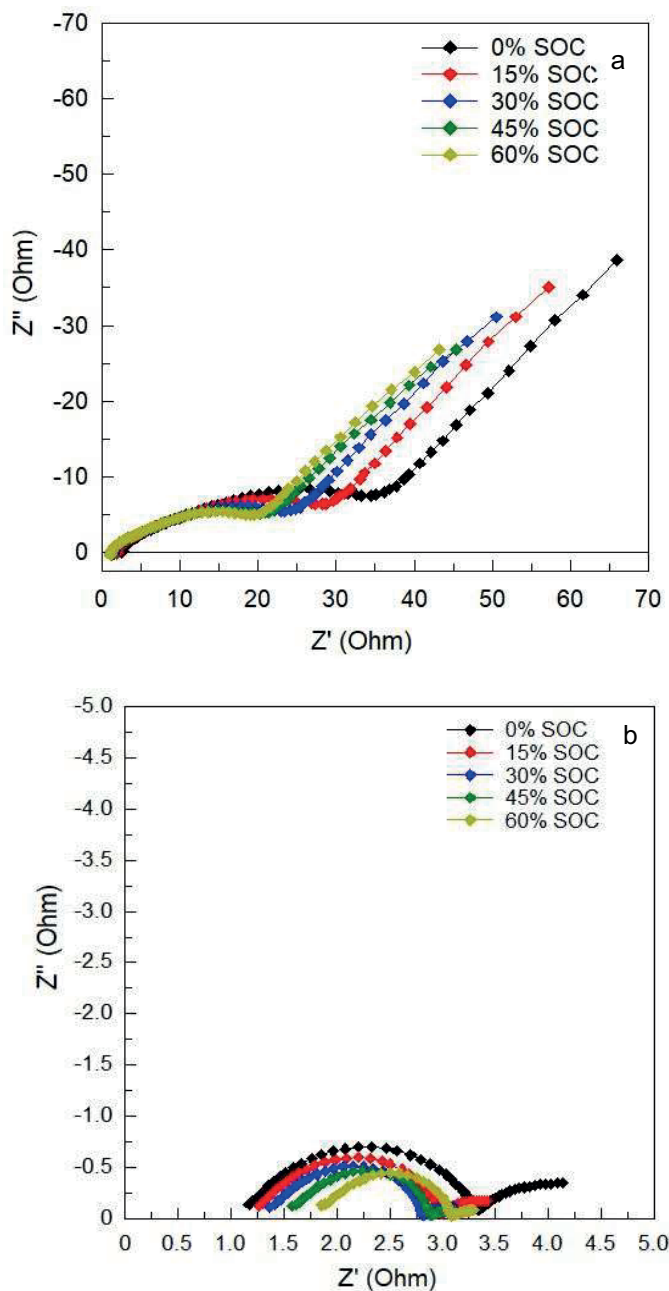
Figure 4.2. In-situ electrochemical impedance spectroscopy (EIS) analysis of half-cell electrolytes under various SOCs for the 1st cycle of charge at a current density of 10 mA·cm^{-2}. (a) anolyte and (b) catholyte with 1.5 M ZnI$_2$: KI (1:1). (the inset shows the equivalent circuit model used to fit the experimental data).

4.4.2 Mitigation strategy

Based on the above analysis of the water migration from catholyte to the anolyte via osmosis as an effect of differential ionic concentrations, 2 mol·L^{-1} of KI is added as an extra solute to the catholyte to balance the total concentrations of ions in both compartments at 67% SOC (**table 4.2**). Hence, now, at 0% SOC, total concentrations of ions of anolyte and catholyte are 7.5 mol·L^{-1}, and 11.5 mol·L^{-1} respectively. After the charging process by considering electroplating of 1 mol·L^{-1} Zn^{2+} and formation of 1 mol·L^{-1} I$_3^-$, the total concentration of ions is 6.5 mol·L^{-1} in anolyte and 9.5 mol·L^{-1} in catholyte. Afterward, the migrations of Zn^{2+} and K$^+$ cations for charge neutrality, the total concentrations of ions reach a balanced state of the identical value of 8 mol·L^{-1} in each chamber unlike the previous electrolyte of values 8 mol·L^{-1} in anolyte and 4 mol·L^{-1} in catholyte.

Table 4.2. Mass balance of an asymmetric electrolyte formulation (+2 M KI at the catholyte).

	[Zn^{2+}](M)	[K$^+$](M)	[I$^-$](M)	[I-](M)	Charge	∑[i] (M)
ANOLYTE						
0% SOC	1.5	1.5	4.5		0	7.5
67% SOC -no compensation-	0.5	1.5	4.5		-2	6.5
67% SOC -after ion migration-	1.0	2.5	4.5		0	**8.0**
CATHOLYTE						
0% SOC	1.5	3.5	6.5		0	11.5
67% SOC -no compensation-	1.5	1.5	1.5	1.0	2	9.5
67% SOC -after ion migration-	1.0	2.5	3.5	1.0	0	8.0

To get a practical insight of the water migration mechanism as an effect of differential ions concentrations and amelioration by balancing the total number of ions in both compartments after the addition of extra solute to the catholyte, the ZIFB cell was cycled with 1.5 M ZnI$_2$:KI (1:1) anolyte, and with 1:1 and 1.5: 3.5 ratios in the catholyte at 20 mA·cm^{-2}. **Figure 4.3a** represents the volume variations of half-cell electrolytes after 1st charge cycle of cases: without and with added 2 M KI in the catholyte. At the 1st charged state, these two sets of electrolytes depict a well-clear difference in volume. The cell operated with the standard 1:1 ratio catholyte, shows ~3.75 mL of water transfer from catholyte to anolyte, whereas the cell ran with added extra KI presents comparatively less water shuttle of ~1.25 mL. The optical images of half-cell electrolytes (**figure 4.3b-g**) before and after charge depict the real-time picture of water migration. Overall, this comparison of the half-cell electrolytes volume changes in two cases justifies the hypothesis explained of suppressing water migration (**table 4.2**) by balancing the total concentration of ions between the two chambers.
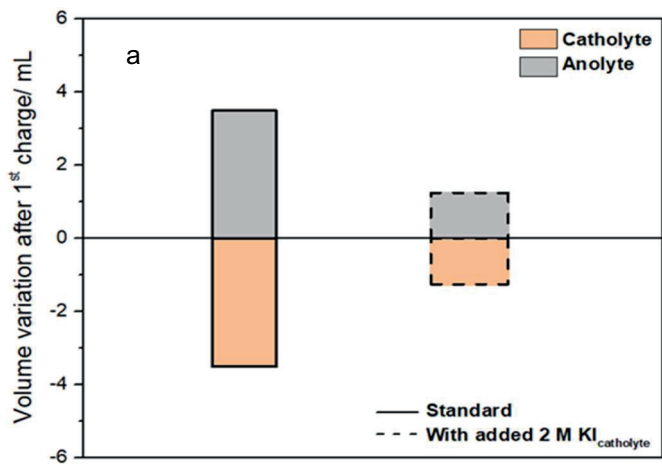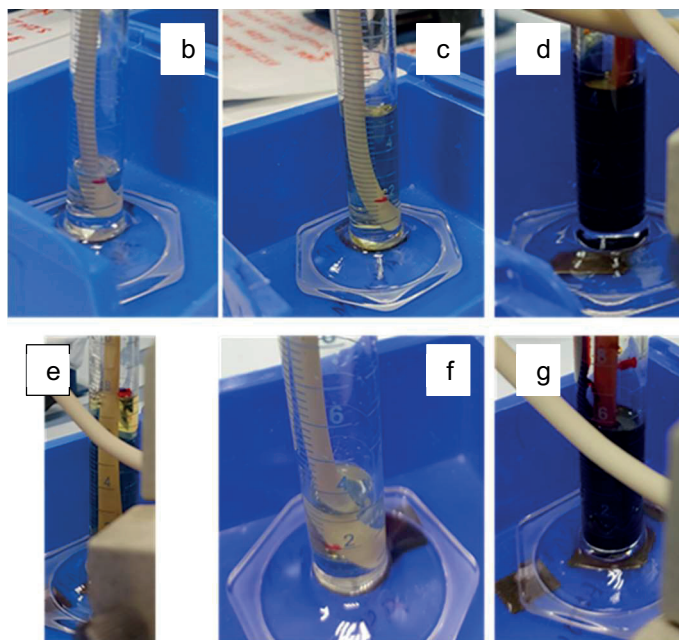
Figure 4.3. Volume variations of electrolytes after ZIFB full-cell cycling at a current density of 20 mA·cm^{-2}. (a) after 1st charge cycle. Optical images of volume variations. (b) 1.5 M ZnI$_2$:KI (1:1) (at 0% SOC); after 1st charging cycle (c) anolyte & (d) catholyte; (e) 1.5 M ZnI$_2$: KI (1:1) + 2 M KI$_{catholyte}$ (at 0% SOC); after 1st charging cycle (f) anolyte & (g) catholyte.
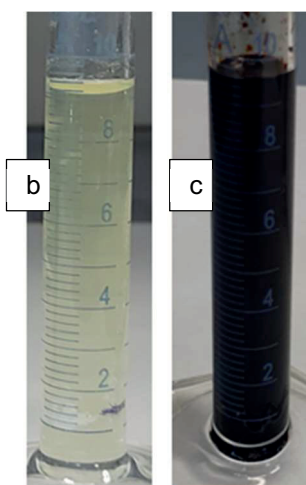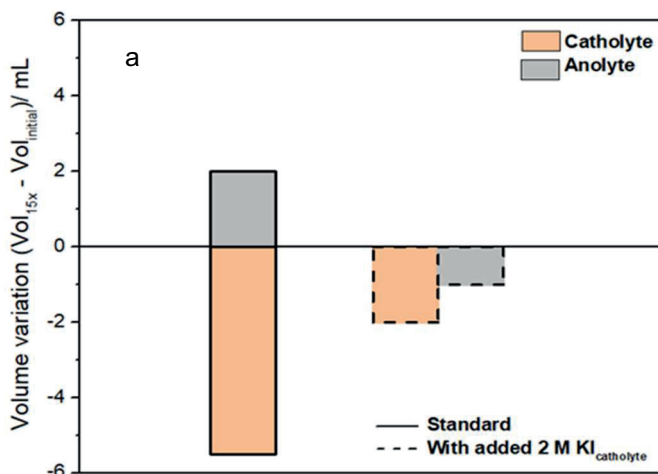
Figure 4.4. Volume variations of electrolytes after ZIFB full-cell cycling at a current density of 20 mA·cm^{-2}. (a) after 15th charge-discharge cycles. Optical images of volume variations of the cell assembled with the tuned electrolyte of 2 M KI$_{catholyte}$ (b) anolyte & (c) catholyte (picture has taken after reverse flow).

Furthermore, the volume of half-cell electrolytes after 15 continuous cell charge-discharge cycles with tuned electrolytes is illustrated in the bar graph in **figure 4.4a**. Unlike the volume variations trend with the cell operated with standard electrolyte, here, the trend is not that similar of extreme decrement of catholyte volume and increment of anolyte volume despite a way less reduction of catholyte volume (~2 mL). Optical images of cycled electrolytes in **figure 4.4b-c**, present almost the same electrolyte volumes, adding another evidence of suppressed water transfer from catholyte to anolyte as a real-time view.
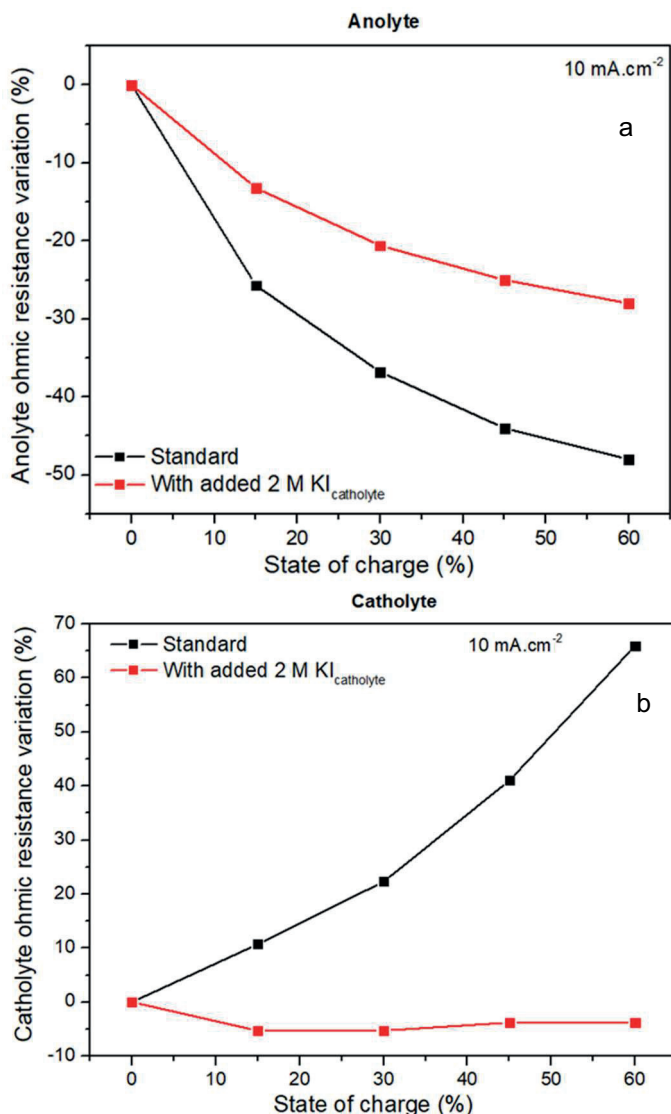
Figure 4.5. Comparison of the variations of (a) anolyte, and (b) catholyte ohmic resistances (R_{ohm}) with various SOCs for both electrolyte formulations (data reported in **Table 4.3**).

The measurement using the auxiliary cells revealed a more stable ohmic resistance of both compartments in the asymmetric electrolyte formulation compared to the standard cell, as shown in **figure 4.5**. The addition of extra KI at the catholyte compensates the ohmic resistance increment due to the depletion of I⁻ and K⁺ ions during the charging process, corroborating our initial hypothesis. On the other hand, the reduction of ohmic resistance at the anolyte is unavoidable due to the replacement of Zn^{2+} by K⁺ ions and the differences between both configurations might be attributed to the effective ion concentrations and mobilities owing to the fact that water is also migrating to the anolyte side.

Table 4.3. Parameters from the EIS fitting using the Randles circuit model.

	SOC (%)	R_{Ohm} ($\Omega \cdot cm^{-2}$)	CPE1-T	CPE1-P	R_{ct} ($\Omega \cdot cm^{-2}$)	W_s1-R	W_s1-T	W_s1-P
Circuit parameters: Anolyte								
Standard		0.49	0.001	0.46	9.56	231.30	19.10	0.59
With added 2 M KI$_{catholyte}$	0	0.68	0.001	0.69	1.59	82.10	166.80	0.38
Standard		0.36	0.002	0.47	7.68	218.40	21.00	0.59
With added 2 M KI$_{catholyte}$	15	0.59	0.001	0.61	2.25	40.80	10.40	0.43
Standard		0.31	0.001	0.49	6.18	199.30	24.00	0.56
With added 2 M KI$_{catholyte}$	30	0.54	0.001	0.56	2.88	43.50	8.10	0.45
Standard		0.28	0.002	0.53	4.94	195.60	37.60	0.51
With added 2 M KI$_{catholyte}$	45	0.51	0.001	0.60	2.30	33.50	7.70	0.47
Standard		0.25	0.002	0.54	4.62	194.50	37.50	0.52
With added 2 M KI$_{catholyte}$	60	0.49	0.001	0.61	2.13	32.20	9.10	0.47

4

	SOC (%)	R_{Ohm} ($\Omega \cdot cm^{-2}$)	CPE1-T	CPE1-P	R_{ct} ($\Omega \cdot cm^{-2}$)	CPE1-T	CPE1-T
				Circuit parameters: Catholyte			
Standard		0.28	0.0001	0.73	0.52	1.11	0.32
With added 2 M $KI_{catholyte}$	0	2.41	2.33E-05	0.76	1.49	0.14	0.26
Standard		0.31	0.0001	0.76	0.42	2.24	0.33
With added 2 M $KI_{catholyte}$	15	2.28	8.46E-06	0.84	0.79	0.72	0.09
Standard		0.34	0.0001	0.78	0.35	3.45	0.32
With added 2 M $KI_{catholyte}$	30	2.28	8.76E-06	0.84	0.80	1.00	0.09
Standard		0.39	0.0001	0.78	0.32	4.54	0.32
With added 2 M $KI_{catholyte}$	45	2.31	1.02E-05	0.83	1.01	1.50	0.18
Standard		0.46	0.0001	0.79	0.30	4.75	0.30
With added 2 M $KI_{catholyte}$	60	2.32	7.24E-06	0.88	1.01	1.50	0.23

4

4.4.3   Mass transport through the membrane

To corroborate that the ion transport through the Nafion membrane influences the water crossover during charge, Zn^{2+} and K^+ ions concentrations were determined by ICP-OES. Measurements were done with standard 1:1 catholyte and tuned 1.5:3.5 catholyte at 0% and 67% SOC. Concentrations of I^- and I_3^- ions are calculated from the faradaic equations based on the Zn^{2+} and K^+ ions concentrations and moles of solutes were estimated by multiplying the molar concentrations with the final measured volume after the charge (presented in **tables 4.4-4.5**).

Table 4.4. The final volume of half-cell electrolytes after the charge (measured after reverse flow).

Electrolyte	Compartment	Cases	Final volume measured (mL)
1.5 M ZnI$_2$:KI	Anolyte	0% SOC	10.00
		67% SOC	13.50
	Catholyte	0% SOC	10.00
		67% SOC	6.50
[1.5 M ZnI$_2$:KI] + 2 M KI$_{catholyte}$	Anolyte	0% SOC	10.00
		67% SOC	11.25
	Catholyte	0% SOC	10.00
		67% SOC	8.75

Table 4.5. Comparison of total ion concentrations (M) of half-cell electrolytes at 0% SOC and after 1st charge cycle of ZIFB single cell with electrolytes of standard and with added 2 M KI in catholyte at 20 mA·cm^{-2}. Data of Zn^{2+} and K^+ were measured by ICP-OES.

Standard electrolytes										
Side	[Zn^{2+}] (M)	Zn^{2+} (mol)	[K$^+$] (M)	K$^+$ (mol)	[I$^-$] (M)	I$^-$ (mol)	[I$_3^-$] (M)	I$_3^-$ (mol)	Total (mol)	[Total] (M)
Anolyte 0% SOC	1.3400 ±0.04	0.0134 ±0.04	1.4100 ±0.006	0.0141 ±0.006	4.0900 ±0.03	0.0409 ±0.03	0	0	0.0684 ±0.02	6.8400 ±0.02
Catholyte 0% SOC	1.3400 ±0.04	0.0134 ±0.04	1.4100 ±0.006	0.0141 ±0.006	4.000 ±0.03	0.0409 ±0.03	0	0	0.0684 ±0.02	6.8400 ±0.02
Anolyte 67% SOC	0.6500 ±0.03	0.0080 ±0.03	1.8000 ±0.01	0.0243 ±0.01	3.8200 ±0.03	0.0510 ±0.03	0	0	0.0840 ±0.01	6.2700 ±0.01
Catholyte 67% SOC	0.8900 ±0.04	0.0050 ±0.04	0.3200 ±0.03	0.0020 ±0.03	2.1000 ±0.04	0.0130 ±0.04	1.3900 ±0.04	0.0090 ±0.04	0.0300 ±0.02	4.7000 ±0.02

With added 2 M KI$_{catholyte}$										
Side	[Zn^{2+}] (M)	Zn^{2+} (mol)	[K$^+$] (M)	K$^+$ (mol)	[I$^-$] (M)	I$^-$ (mol)	[I$_3^-$] (M)	I$_3^-$ (mol)	Total (mol)	Total (M)
Anolyte 0% SOC	1.3400 ±0.04	0.0134 ±0.04	1.4100 ±0.006	0.0141 ±0.006	4.0900 ±0.03	0.0409 ±0.03	0	0	0.0684 ±0.02	6.8400 ±0.02
Catholyte 0% SOC	1.2000 ±0.04	0.0120 ±0.04	2.9500 ±0.005	0.0295 ±0.005	5.3500 ±0.03	0.0535 ±0.03	0	0	0.0950 ±0.02	9.5000 ±0.02
Anolyte 67% SOC	0.4600 ±0.04	0.0050 ±0.04	2.4800 ±0.020	0.0280 ±0.02	3.9500 ±0.03	0.0440 ±0.03	0	0	0.0770 ±0.02	6.8900 ±0.02
Catholyte 67% SOC	0.9400 ±0.04	0.0080 ±0.04	1.1400 ±0.010	0.0100 ±0.01	3.0200 ±0.03	0.0260 ±0.03	1.0300 ±0.03	0.0090 ±0.03	0.0530 ±0.03	6.1300 ±0.03

The standard electrolyte is having identical numbers of moles of Zn^{2+} and K$^+$ ions before charge. From the differences in the number of moles of K$^+$ ions in anolyte and catholyte, before and after charge, it is estimated that ~85% of K$^+$ ions moved from catholyte to anolyte through the membrane. On the other side, the differences between Zn^{2+} ions in the anolyte and catholyte indicate that ~63% of Zn^{2+} ions moved from catholyte to anolyte in the charging process. Whereas the tuned electrolyte with extra added 2 M KI in the catholyte is depicting a different scenario after charge, with around 66% of K$^+$ and 32% of Zn^{2+} ions migrated from catholyte to anolyte during charge. For better understanding, schematic illustrations of ion transport resulting in water transfer phenomena through the membrane before and after charge, are explained in **figure 4.6**. To sum up, according to our observations, K$^+$ ions are the dominant migrating cationic species through the membrane, compared to divalent Zn^{2+} ions. In the standard electrolyte, almost all the K$^+$ ions from the catholyte along with a major portion of Zn^{2+} ions moved to the anolyte while in the tuned electrolyte, comparatively 50% less Zn^{2+} ions migrated due to the availability of more K$^+$ ions in the catholyte solution.
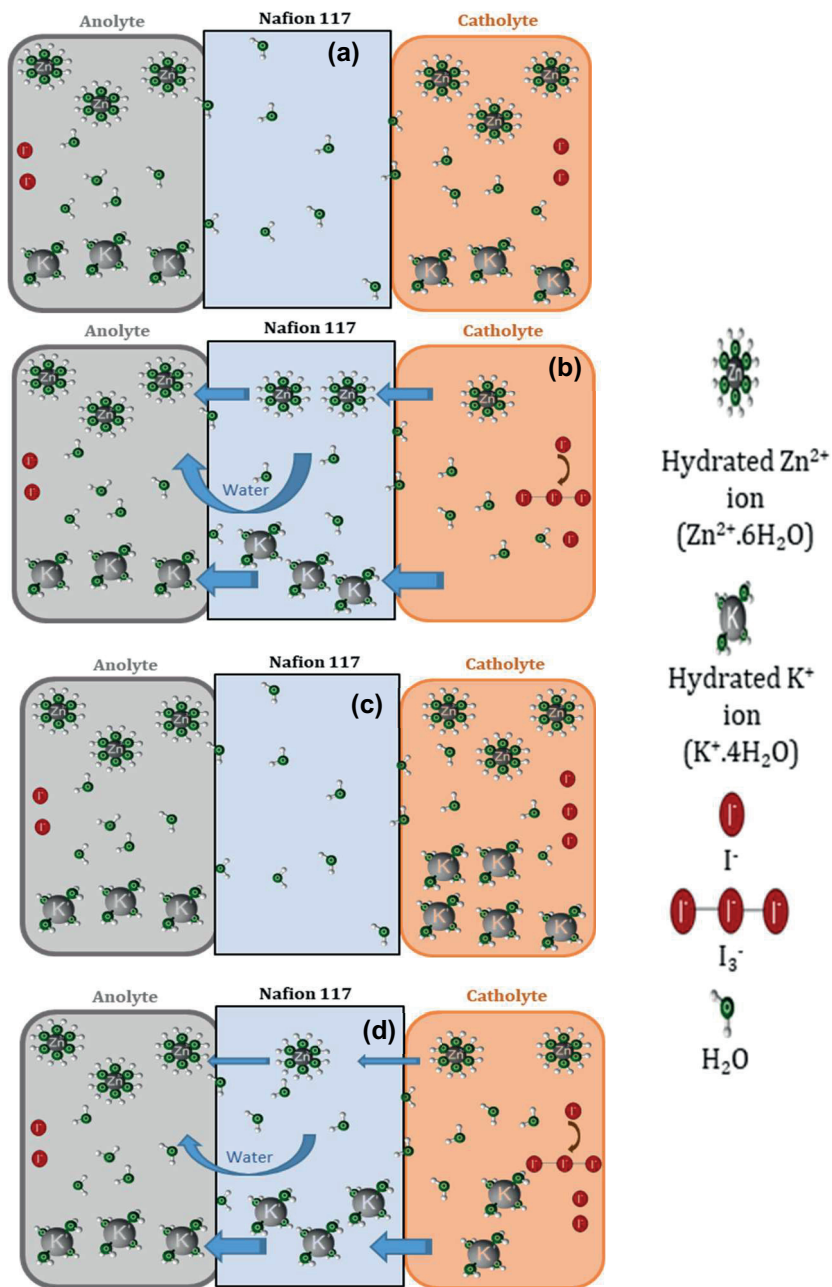
Figure 4.6. Schematic illustration of cations migration mechanism following water transfer through Nafion 117 CEM in charge process of electrolytes consisting of 1.5 M ZnI_2: KI (1:1) before charge (a), after charge (b), and 1.5 M ZnI_2: KI (1:1) + 2 M KI$_{catholyte}$, before charge (c) and after charge (d).

Several parameters play important roles in cation diffusion and water transport through the Nafion membrane. Nightingale et al. compared the hydrated ionic radii of various monovalent and multivalent ions, reporting hydrated Zn^{2+} ions ($Zn^{2+}\cdot 6H_2O$) of radii 4.3 Å and hydrated K^+ ions ($K^+\cdot 4H_2O$) of 3.3 Å respectively.[16] These values give a clear view of what we have observed that solvated K^+ ions move faster through the membrane than Zn^{2+} ions because of having higher mobility. Xie and Okada et al. stated that water transport behavior in Nafion 117 is related to parameters like surface-charge density, and hydration enthalpy of the cations. After conducting experiments with various aqueous electrolytes containing monovalent and multivalent cations, it has been found that divalent cations exhibit higher charge density and hydration enthalpy,[17] hence, tend to carry more water molecules during transport.[18] The study of Goswami et al. about the self-diffusion coefficients of monovalent and divalent cations in Nafion 117 presents that monovalent ions have higher self-diffusion coefficients compared to divalent ions. Consequently, K^+ ions show a higher diffusion coefficient value than Zn^{2+} ions. In addition, they have performed water uptake studies of these various ions in Nafion 117, and the results show lower water uptake capacity by K^+ ions (12.3%) compared to Zn^{2+} ions (21.3%).[19] All these studies closely match with the results we obtained. In this sense, although divalent Zn^{2+} cations possess lower self-diffusion coefficients and slower mobility than K+ ions, can transport more water molecules through the membrane, due to their higher water uptake, being major responsible for water migration. Now, the comparison of the link between the ions and water transport scheme through the membrane of the two sets of electrolytes we have studied is very clear: in the standard electrolyte, after the migration of almost all hydrated K^+ ions, a major portion of Zn^{2+} ions along with large water molecules migrate from catholyte to anolyte, causing larger volume variation; whereas due to the availability of more K^+ ions in the tuned electrolyte, almost ~50% less Zn^{2+} ions migrated which significantly suppresses the water migration.

Besides, the number of moles of I^- ions in anolyte before and after the charged state of both, the standard and tuned electrolyte, shows well evidence of no migration of anions through Nafion 117. Finally, the total number of moles and the total molar ion concentrations depict the complete picture of the standard and tuned electrolyte system, showing much higher total molar concentrations in anolyte compared to catholyte in the case of standard electrolyte whereas the difference is comparatively very less in the tuned electrolyte. Comparison of these practical values of molar concentrations with the detailing, given in the theoretical calculation (**table 4.1** for standard electrolyte) and (**table 4.2** for tuned electrolyte), makes a close correlation that balancing the total ions concentrations of half-cell electrolytes by addition of extra solute to the compartment of lower solute concentrations (catholyte in this case) is an efficient way to suppress the water crossover through the membrane which is an effect of differential ions concentrations.

4.4.4 Electrochemical performance

Figure 4.7 shows the comparison of the first cycle of the charge-discharge profile of the ZIFB single cell, carried out with these two sets of electrolytes at a current density of 10 mA·cm^{-2}. The cell with tuned electrolyte is exhibiting better performance with higher discharge capacity and lower internal resistance compared to the cell with standard electrolyte. During the charge, R_{ohm} of the full ZIFB single cell was estimated from the current-interrupt method (**figure 4.8** and **table 4.6**). It is interesting to mention that, compared to the cell consisting of standard electrolytes, the cell with tuned electrolyte exhibits an average of 100 mV magnitude of lower polarization voltage following a stable R_{ohm}, associated with the lowest voltage drop after relaxation throughout the different SOCs. These stable and lowest values of R_{ohm} of the cell agree with the stable catholyte R_{ohm} values obtained from EIS analyses (**figure 4.5b**) together with the restriction of Zn^{2+} migration through the membrane as seen in ICP analysis. These R_{ohm} values could give a preliminary idea about the electrical conductivity of the cell which is higher in the case of the asymmetric formulation.
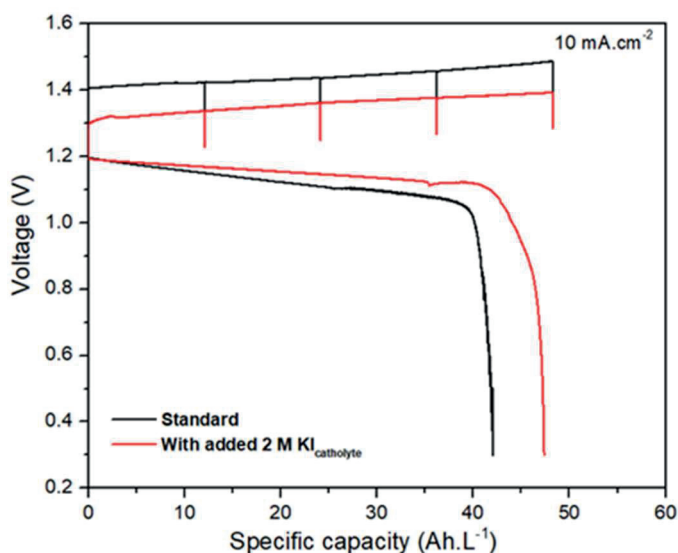
Figure 4.7. Comparison of 1st cycle charge-discharge voltage curves of the ZIFB single cell with the electrolyte without and with added 2 M KI in catholyte at a current density of 10 mA·cm^{-2}.
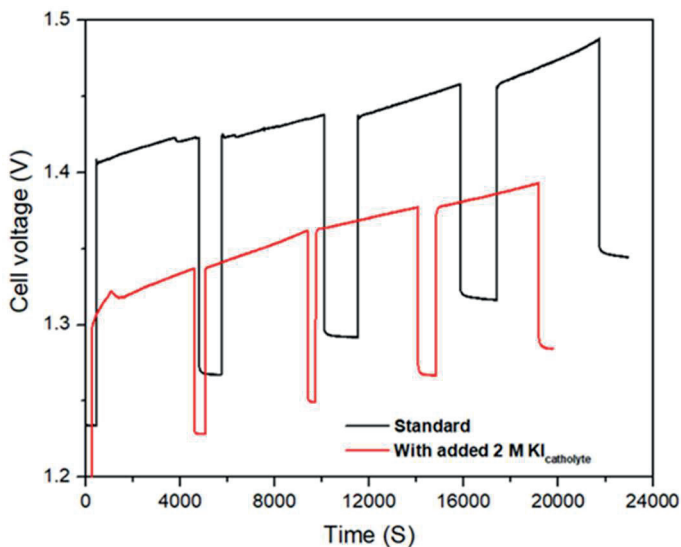
Figure 4.8. Voltage profile of ZIFB cell of standard and with 2 M KI in catholyte, used for Current-interruption method.

Table 4.6. Comparison of R_{ohm} of ZIFB single cell from the current-interrupt method under various SOCs of the 1st charge cycle with electrolytes of standard and added 2 M KI in catholyte at the current density of 10 mA·cm^{-2}.

	SOC(%)	V1 (V)	V2 (V)	ΔV_{ohmic} (V)	Ohmic resistance ($\Omega \cdot cm^2$)
Standard		1.42	1.27	0.15	15.00
With added 2 M KI$_{catholyte}$	15	1.34	1.25	0.11	11.00
Standard		1.44	1.33	0.11	11.00
With added 2 M KI$_{catholyte}$	30	1.36	1.25	0.11	11.00
Standard		1.46	1.32	0.14	14.00
With added 2 M KI$_{catholyte}$	45	1.34	1.23	0.11	11.00
Standard		1.48	1.35	0.13	13.00
With added 2 M KI$_{catholyte}$	60	1.39	1.29	0.10	10.00

In conclusion, these comparisons of half-cell electrolyte conductivity following full-cell electrical conductivities with standard and tuned electrolytes, add another parallel statement to our present study of electrolytes volume imbalances of ZIFB. The cell operating with balanced electrolytes concentrations, not only suppressed the water crossover but also improved the cell conductivity.

4.5 Conclusion

Water migration in RFBs long-term cycling is a serious issue since it hinders RFBs from full-fledged commercialization. In this study of volume variations of electrolytes of zinc-iodide flow batteries, differences in total ions concentrations between half-cell charged electrolytes are proposed to be the main underlying factor for water migration, specifically caused by water transport from the compartment of lower (catholyte) to higher (anolyte) ions concentrations via osmosis phenomenon. Balancing the total ions concentrations on both sides of electrolyte chambers, by the addition of extra solute (KI) to the chamber of lower molar concentration (catholyte in this case) has been suggested as a reliable solution for suppressing water migration. This theoretical approach has been successfully demonstrated experimentally starting from the volume evaluation of ZIFB cell after 1st charge and post-cycling electrolytes. Moreover, analysis of water and ions transport mechanism through Nafion 117 membrane reports K^+ ions are the dominant migrating ion, the addition of extra KI in the catholyte could reduce the passage of large solvated Zn^{2+} ions resulting in a higher portion of water transfer. Furthermore, from the stable charged catholyte ohmic resistances from EIS analysis and improved cell electrical conductivity, consequently, better charge-discharge performance confirmed the overall positive impact of ZIFB cell cycling with the electrolyte of balanced molar concentrations. This approach, by formulating the electrolytes with the only addition of extra solute ions of the same solution chemistry, to suppress water migration while maintaining the classical flow battery format, can positively add a valuable point to the commercialization of the next-generation flow batteries.

4.6 References

1. B. Li, J. Liu, Z. Nie, W. Wang, D. Reed, J. Liu, P. McGrail, and V. Sprenkle, *Nano Lett.*, **16**, 4335–4340 (2016).

2. G. M. Weng, Z. Li, G. Cong, Y. Zhou, and Y. C. Lu, *Energy Environ. Sci.*, **10**, 735–741 (2017).

3. M. Mousavi, G. Jiang, J. Zhang, A. G. Kashkooli, H. Dou, C. J. Silva, Z. P. Cano, Y. Niu, A.Yu, and Z. Chen., *Energy Storage Mater.*, **32**, 465–476 (2020).

4. J. Zhang, G. Jiang, P. Xu, A. G. Kashkooli, M. Mousavi, A. Yu and Z. Chen, *Energy Environ. Sci.*, **11**, 2010–2015 (2018).

5. C. Xie, H. Zhang, W. Xu, W. Wang, and X. Li, *Angew. Chemie - Int. Ed.*, **57**, 11171–11176 (2018).

6. C. Sun, J. Chen, H. Zhang, X. Han, and Q. Luo, *J. Power Sources*, **195**, 890–897 (2010).

7. K. W. Knehr, E. Agar, C. R. Dennison, A. R. Kalidindi, and E. C. Kumbur, *J. Electrochem. Soc.*, **159**, A1446–A1459 (2012).

8. L. Yan, D. Li, S. Li, Z. Xu, J. Dong, W. Jing, and W. Xing, *ACS Appl. Mater. Interfaces*, **8**, 35289–35297 (2016).

9. K. Oh, M. Moazzam, G. Gwak, and H. Ju, *Electrochim. Acta*, **297**, 101–111 (2019).

10. Y. Song, X. Li, J. Xiong, L. Yang, G. Pan, C. Yan, and A. Tang, *J. Power Sources*, **449**, 227503 (2020).

11. X. Liu, H. Zhang, Y. Duan, Z. Yuan, and X. Li, *ACS Appl. Mater. Interfaces*, **12**, 51573–51580 (2020).

12. M. Mousavi, H. Dou, H. Fathiannasab, C. J. Silva, A. Yu, and Z. Chen *, *Chem. Eng. J.*, **412**, 128499 (2021).

13. C. Xie, Y. Liu, W. Lu, H. Zhang, and X. Li, *Energy Environ. Sci.*, **12**, 1834–1839 (2019).

14. S. Ito, M. Sugimasa, Y. Toshimitsu, A. Orita, M. Kitagawa, and M. Sakai, *Electrochim. Acta*, **319**, 164–174 (2019).

15. J. D. Jeon, H. S. Yang, J. Shim, H. S. Kim, and J. H. Yang, *Electrochim. Acta*, **127**, 397–402 (2014).

16. E. R. Nightingale, *J. Phys. Chem.*, **63**, 1381–1387 (1959).

17. D. W. Smith, *J. Chem. Educ.*, **1**, 1–3 (1977).

18. G. Xie and T. Okada, *J. Electrochem. Soc.*, **142**, 3057–3062 (1995).

19. A. Goswami, A. Acharya, and A. K. Pandey, *J. Phys. Chem. B*, **105**, 9196–9201 (2001).

Chapter 5

Boosting ZIFB performance by introducing NaCl as a supporting electrolyte
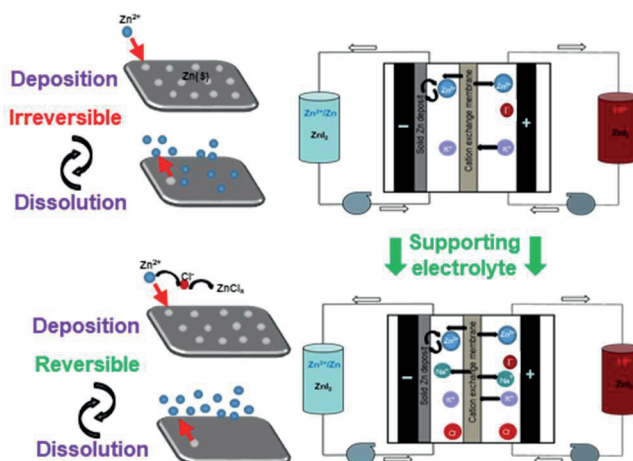
The main parts of this chapter are currently `under peer-review´ in Journal of Power Sources as ¨A long cycle life zinc-iodide flow battery enabled by a multifunctional low cost supporting electrolyte¨ by Monalisa Chakraborty, Teresa Andreu, Maxim Guc, Mohamed Amazian, and Sebastián Murcia-López (submitted on August 2022).

The text and figures (submitted to the journal) have been marginally edited and reorganised for this thesis chapter, and parts of the introduction and experimental part were omitted as that was already introduced in the general introduction (Chapter 1) and experimental methods (Chapter 2) chapters. Additional figures from the Supporting information of the submitted article have been included in the chapter.

5

5.1 Publication abstract

Zinc-iodide flow battery (ZIFB) offers great promise for future grid-scale stationary energy storage attributed to its high energy density and low cost. However, their practical performance is hindered due to critical challenges such as poor cyclability, capacity fading because of irreversible zinc plating and stripping, slow kinetics of the redox reactions, and insoluble iodine (I_2) precipitation. In this study, we report NaCl-supported electrolyte chemistry to address these issues simultaneously. The addition of NaCl improved the redox reversibility of Zn/Zn^{2+}. Experimental results depict that the coordination interactions between Zn^{2+} and Cl^- in the formation of soluble chloride anions, are the key factor for the improvement of Zn/Zn^{2+} redox reversibility. While the formation of soluble I_2Cl^- complex stabilizes the battery from solid I_2 precipitation, participation of Na^+ and K^+ as main charge balance carriers passing through cation exchange membranes, restricts Zn^{2+} migration, thus, blocking the electrolyte crossover. A ZIFB with the improved electrolyte delivers high-energy efficiency, stable discharge capacity, and long cycle life (100 cycles) at 20 mA·cm^{-2} while a conventional ZIFB shows the trend of capacity fade right from 10 cycles. These encouraging results indicate that the addition of a cost-effective salt, NaCl, enlightens great prospects for high-performance ZIFB applications.

5.2 Introduction

5.2.1 Scope of our work based on the current state of the art

Despite, ZIFB being a promising contender for next-generation RFBs,[1–3] several challenges must be addressed before the successful advancement, such as poor cyclability as a consequence of capacity fading over cycling which is mainly due to the irreversible Zn plating/stripping and insoluble solid I_2 precipitation. Also, the low electrolyte conductivity and slow kinetics of redox reactions result in low operating current density, voltage, and energy efficiency.[4,5] Weng et al. reported a ZIFB by the introduction of Br^- ions in the electrolyte as a complexing agent to stabilize I_2 molecules and free up the I^- ions, which leads to increased capacity; however, low operating current density (~5-10 mA·cm^{-2}) and zinc dendrite growth on anode decays the cycling performance.[6] Investigations have been done on various organic and inorganic electrolyte additives to suppress the Zn dendrite.[7–9] For example, Li et al. employed ethanol as the additive in ZIFB to ameliorate the Zn dendrite growth by ligand formation between oxygen and Zn^{2+} ions, which promotes a smoother Zn deposition. However, the addition of organic molecules decreases the ion conductivity of the electrolyte resulting in lower energy efficiency (EE)[9,10]. On the other side, Zn complex formation with inorganic NH_4^+ ions holds great promise so far.[11,12] Jian et al. demonstrated the improvement of electrochemical performance of ZIFB with NH_4Br as a supporting electrolyte by mitigating Zn dendrite formation due to $Zn(NH_3)_x^{2+}$ complexation effect.[11] Goh et al. explained the improvement of the reversibility of the Zn anode in the neutral Zn-air batteries because of the complexation effects of NH_4^+ and Zn^{2+} ions.[12]

5.2.2   Objectives of the chapter

In this work, we propose a ZIFB with improved electrolyte incorporating cost-effective NaCl as an additive to enhance the cell electrochemical performance by addressing the above-discussed issues.

Highlights of the chapter

To obtain the main objectives, the following investigations have carried out:

o   At first, half-cell electrochemical performance evaluation of the effects of NaCl in the Zn/Zn^{2+} and I_3^-/I^- redox reactions by CV analyses.

o   Comparison of ZIFB full-cell cycling performances of electrolytes, without and with NaCl.

o   Assessment of the effects of NaCl on the anode side by electrodeposition and further ex-situ SEM and XRD characterisations for the anode, and Raman spectroscopy for the electrolyte.

o   Evaluation of the effects of NaCl on the catholyte by Raman spectroscopy.

o   Finally, the hypothesis on the improvement of the cell CE (%) by modified cations transfer mechanism through N117 CEM with the addition of NaCl.

A note to the reader:

The `materials and methods´ related to this chapter have already been discussed in the general experimental methods chapter (**Chapter 2**). The component details of ZIFB cell assembling are explained in **section 2.2.1** and **table 2.1**. Here, 1.5 M sodium chloride (NaCl, ≥ 99%, Sigma Aldrich) was added to the electrolyte on both sides as a supporting electrolyte.

Half-cell and ZIFB full-cell electrochemical performance assessments were tested by cyclic voltammetry, galvanostatic electrodeposition, and charge-discharge cycling respectively. Physicochemical characterisations were evaluated by SEM, XRD, and Raman spectroscopy. The experimental settings and parameters of all these above-mentioned techniques implemented in this chapter are thoroughly detailed in **Chapter 2**, **sections 2.3** and **2.4**.

5.3 Results and discussion

5.3.1 Half-cell electrochemical performance

CV tests were firstly investigated between the scan rates 10 to 50 mV·s^{-1}, to understand the effects of NaCl as a supporting electrolyte on the electrochemical performance of both Zn/Zn^{2+} and I$_3^-$/I$^-$ redox reactions.

Figure 5.1a shows the CV curve of Zn/Zn^{2+} redox reactions in electrolytes with and without Cl$^-$ ions. It is seen that the solid Zn began depositing at the surface of the working electrode (GCE) at approximately -1.55 to -1.6 V (vs. Hg/Hg$_2$SO$_4$) at all scan rates in electrolyte without NaCl. In the reverse scan, the anodic peak position, which corresponds to the Zn^{2+} stripping (oxidation reaction) from the anode, shows a clear difference in peak shifting of the electrolytes without and with NaCl. The peak appears at approximately -1.3 V (vs. Hg/Hg$_2$SO$_4$) with a negligible shifting in the further scan rates with the electrolyte with Cl$^-$ ions, whereas, much positive shifting has been observed in the solution without NaCl. Moreover, it is interesting to mention that overall, the reductive and oxidative peaks separation is significantly lower with the introduction of Cl$^-$ ions, by shifting the reductive and oxidative peaks towards positive and negative potentials respectively, which depicts the enhanced reversibility of Zn plating and stripping. The total peak separation (ΔE_p) vs. logarithm of scan rates (**figure 5.1b**) curves summarize the above-discussed observations.

On the other hand, **figure 5.2a** displays the CV results of I$_3^-$/I$^-$ redox reaction. It is evident that the introduction of NaCl in the electrolyte significantly decreases the overpotentials of both oxidation and reduction, respectively. As a result, the anodic and cathodic peak potential difference (ΔE_p) reduces substantially (**figure 5.2b**). Moreover, the oxidation and reduction peak currents are higher than those in the pristine solution, and also exhibit a linear dependence on the square root of scan rates (**figure 5.2c**), implying that the I$_3^-$/I$^-$ redox reaction rate is diffusion-limited. The comparison of diffusion coefficients of I$^-$ and I$_3^-$, calculated based on the Randles-Sevcik equation **(table 5.1)** presents an eye-catching enhancement in the presence of NaCl. To sum up, the presence of NaCl as a supporting electrolyte is beneficial in both, anode and cathode sides redox reactions in terms of reversibility, by showing lower anodic and cathodic polarization as well as improvement in the kinetics of I$_3^-$/I$^-$ redox reaction via enhancement of diffusion coefficients. Therefore, these CV results could provide strong evidence that adopting NaCl as a supporting electrolyte is helpful for the electrochemical performance of ZIFB.
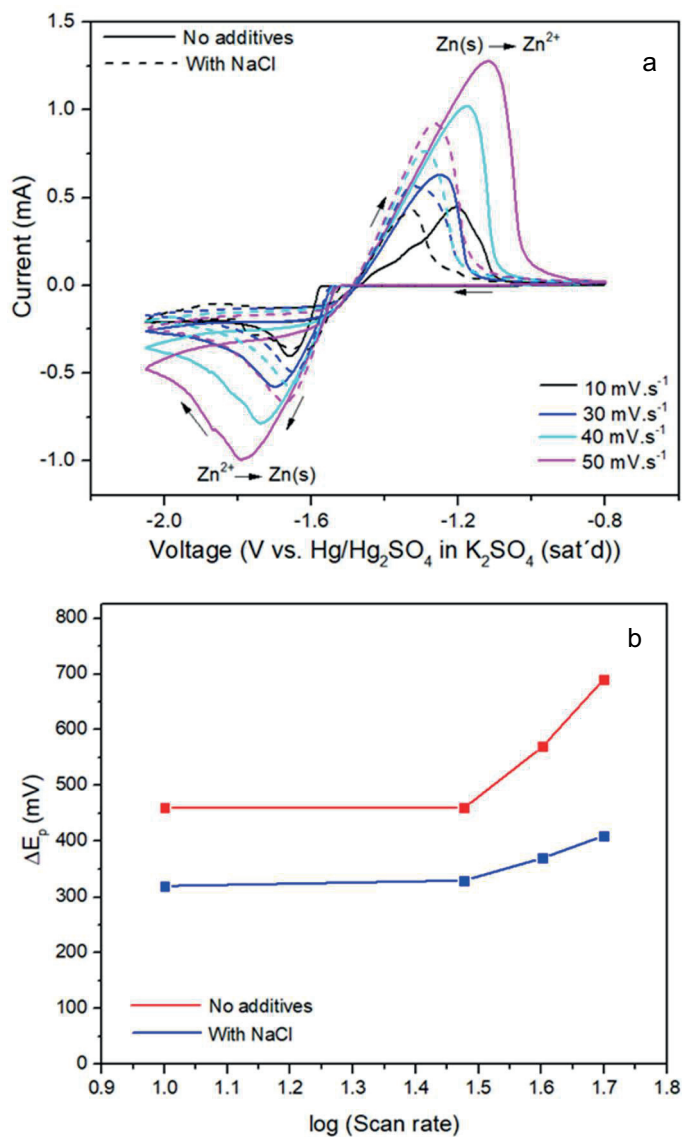
Figure 5.1. (a) Cyclic voltammograms and (b) determination of the peak potential separation vs. logarithm of different scan rates between the oxidation and reduction signal of Zn/Zn^{2+} redox reaction. CV tests were carried out at the scan rates between 10-50 $mV·s^{-1}$ in 25 mM ZnI_2: KI electrolytes with and without NaCl.
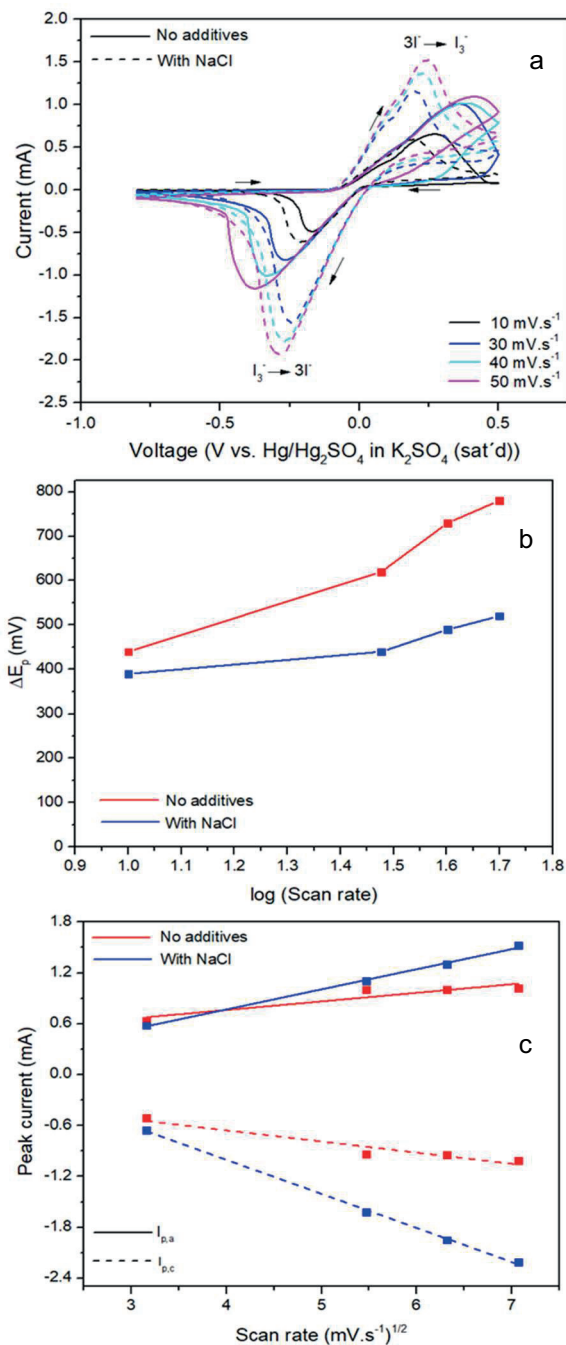
Figure 5.2. (a) Cyclic voltammograms of I_3^-/I^- redox reaction, (b) determination of the peak potential separation between the oxidation and reduction signal of I_3^-/I^- redox reactions vs. logarithm of different scan rates, and (c) anodic and cathodic peak currents of I_3^-/I^- redox reactions vs. square root of different scan rates, of electrolytes with and without NaCl.

Table 5.1. Comparison of diffusion coefficients for I^- and I_3^- ions in catholytes, without and with NaCl obtained by the Randles-Sevcik method (data extracted from **figure 5.2b**).

| Catholyte composition	D_I^-	$D_{I_3}^-$
	Absolute value $(10^{-8}\ cm^2 \cdot s^{-1})$	Absolute value $(10^{-8}\ cm^2 \cdot s^{-1})$
No additives	0.95	0.56
With NaCl	9.00	3.00

5.3.2 Electrochemical performance of ZIFB

To investigate the effect of NaCl supporting electrolyte on the full cell cycling performance, ZIFB single cells were assembled to perform the traditional galvanostatic cycling at a current density of 20 mA·cm^{-2}. **Figure 5.3a** displays the cycling efficiencies of cells assembled with and without NaCl. A sudden drop in the coulombic efficiency (CE) and discharge capacity (**figure 5.3b**) after a few cycles is observed in the cell without NaCl in the electrolyte, which follows a continuous degradation of CE. Moreover, the representation of capacity retention with cycling (**figure 5.4a**) displays a clear image of dramatic capacity loss throughout the cycling. The optical image of cycled anode after disassembling the cell in **figure 5.4b** shows that a high amount of Zn deposition remained on the electrode, which enlightens the reason for capacity degradation. The voltage profile of the cell cycled at 40 mA·cm^{-2} (**figure 5.4c**) exhibits a high polarisation loss. In contrast, the battery with NaCl media could be cycled stably for 100 cycles without significant capacity decay and 77% capacity retention at the end of 100 cycles, which finally does not affect the excellent EE. The voltage profile (**figure 5.3b**) demonstrates stable behaviour, almost all the curves overlap with each other, suggesting decent cycling stability of the battery in the presence of NaCl. After certain long cycling (from the 70th cycle onwards), the charge and discharge capacity of the battery experienced a slow decrease (also could be seen in the charge-discharge curve of the 100th cycle in **figure 5.3b**), which might be ascribed to unavoidable losses during the long cycling associated to the crossover of active species through the membrane. As shown in the photograph in **figure 5.4d**, the anode of the cell, cycled in the presence of NaCl unveils that no Zn remains on the electrode, proving improved stability and reversibility of the Zn plating/stripping process in the NaCl media. The small accumulation in the top part of the electrode can be attributed to the effect of non-favourable fluid hydrodynamics in the vicinity of the sealing gasket. Furthermore, the voltage profile at 40 mA·cm^{-2} (**figure 5.4c**) suggests stable and well-coincided curves with each other upon repeated cycling along with lower polarisation loss compared to the battery cycled without NaCl. The enhancement of the discharge voltage of the battery with NaCl-containing electrolyte can be seen in the discharge polarisation and power density curves (**figure 5.4e**),

which exhibit an increment of the peak power density of 36 mW·cm^{-2} at the maximum current density of 60 mA·cm^{-2}.
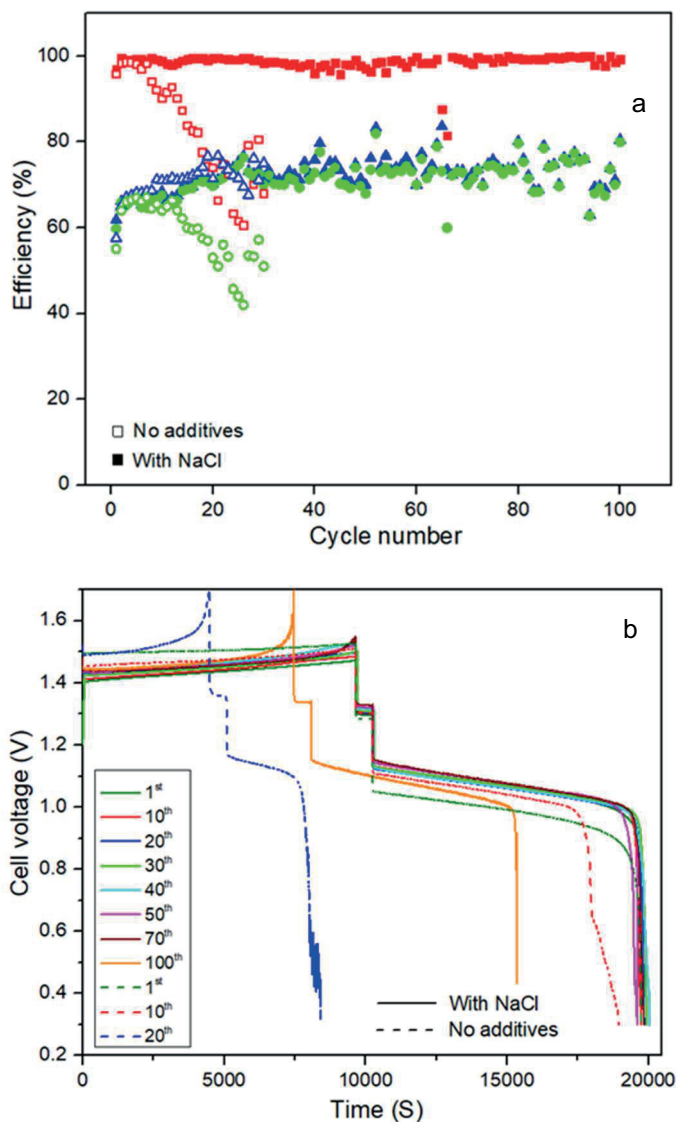
Figure 5.3. Comparison of cycling performance of ZIFB with and without NaCl at a current density of 20 mA·cm^{-2}. (a) coulombic, voltage, and energy efficiencies, (b) charge-discharge curves.
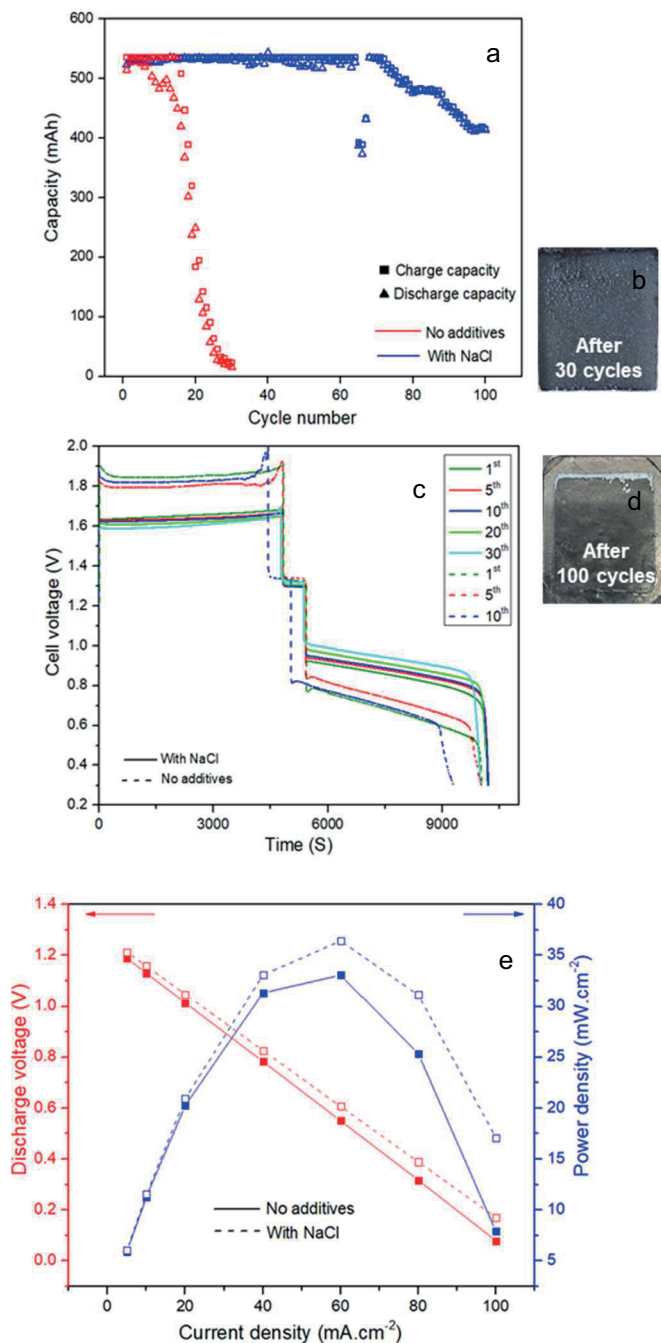
Figure 5.4. (a) Comparison of charge-discharge capacity cycled at 20 mA·cm⁻², (b) cycled anode without NaCl, (c) charge-discharge curves of ZIFB with and without NaCl at 40 mA·cm⁻² (d) cycled anode with NaCl, (e) discharge polarisation curves and calculated power density curves of the ZIFB with and without NaCl in the electrolyte at a SOC of 50%.

To sum up, these results confirm that NaCl is an effective supporting electrolyte for offering reversible Zn plating and stripping, thus improving the cyclability of ZIFB

104

5.3.3 Effect of NaCl as an additive on the anode side
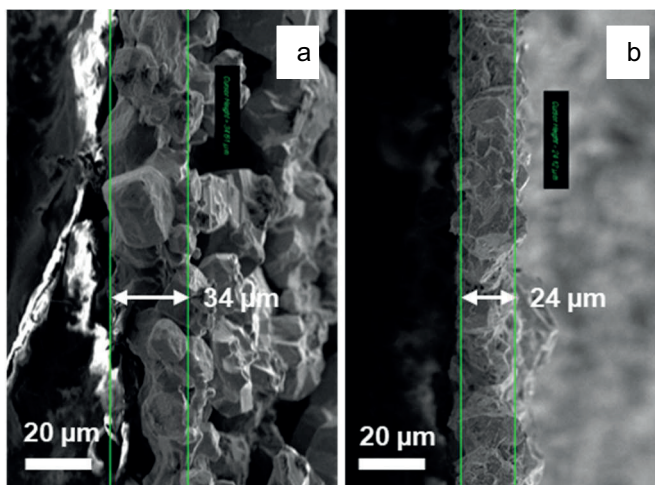
Figure 5.5. Cross-sectional morphologies of Zn deposited on FTO substrate at 20 mA·cm^{-2} with an areal capacity of 30 mA·h·cm^{-2} in 1.5 M ZnI$_2$:KI electrolyte of (a) without and, (b) with 1.5 M NaCl.

For assessing the role of NaCl in the efficient Zn plating in a half-cell mode, the characterisation of electrodeposited Zn on planar FTO substrate has been performed. **Figure 5.5** represents the SEM images of cross-sectional morphology and thickness of electrodeposited Zn after a charge for 90 min at 20 mA·cm^{-2} with the pristine and NaCl added electrolyte respectively. These images depict that the Zn deposition with the NaCl-supported electrolyte is compact and densely packed, showing lower thickness compared to the deposition of the larger size of clusters in the case of pristine electrolyte. The mass of the deposition corresponding to the total applied charge is further validated by the theoretical calculation based on Faraday´s law (see below **calculation** section) and it shows a very close value to the actual weight of the Zn deposition in NaCl-supported electrolyte.

Calculation of the mass of electrodeposited zinc

A comparison of the actual weights of FTO electrodes before and after electrodeposition indicates that the deposited layers weighed 0.035g.

As of SEM images of electrodeposited Zn shown in **figure 5.5**, the total charged capacity for electrodeposition is 30 mA·h.

Based on Faraday´s law:

$$30 \text{ mA·h} = \frac{96485 \times 2 \times n \text{ (mol)}}{3600} = 5.6 \times 10^{-4} \text{ mol}$$

Now, mass of deposited Zn: (considering the atomic weight of Zn: 65.38 g·mol^{-1})

$$5.6 \times 10^{-4} \text{ mol} = \frac{m \text{ (g)}}{65.38 \text{ g·mol}^{-1}} = 0.036 \text{ g}$$

105

This denser and more packed pattern of Zn deposition morphology by the introduction of Cl⁻ ions have also been reported in the previous studies.[13–15] Additionally, XRD patterns of deposited Zn on graphite foil substrate in the electrolyte with and without NaCl (**figure 5.6**) depict only metallic Zn (JCPDS 041–1487) without any impurities along with a peak of weak intensity, which belongs to the graphite (JCPDS 004-0831). For both electrolytes, deposited Zn belongs to the hexagonal crystalline group and exhibits a certain predominant orientation towards the [101] reflection plane. The average crystallite sizes of the Zn deposition, estimated from the FWHM of the [101] plane using Scherrer´s formula are 115 and 72 nm of electrolyte without and with NaCl, respectively. This lower crystallite size in the presence of Cl⁻ ions justifies the densely packed elemental Zn, while the more intense graphite peak observed from the graphite foil substrate justifies the thinner Zn layer, observed in the SEM image.
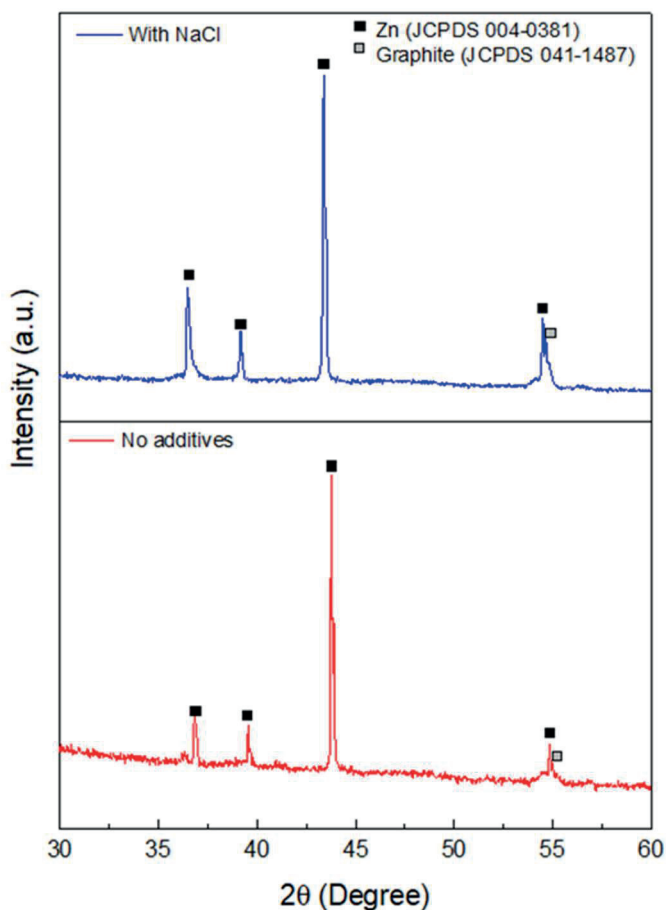
Figure 5.6. XRD patterns of the Zn deposited in electrolytes with and without NaCl.

As a quick summary of the results, we have pointed out so far that introduction of NaCl leads to significant improvements in the electrochemical performance of the Zn/Zn^{2+} half-cell. For instance, the CV results have revealed that NaCl enhances the reversibility of Zn/Zn^{2+} redox reactions, which further reflects through the excellent cyclability and capacity retention in the ZIFB cycling, following reversible Zn plating/de-plating on the anode. Moreover, Cl^- ions in the electrolyte facilitate a smooth, densely packed, and properly oriented Zn plating on the anode.
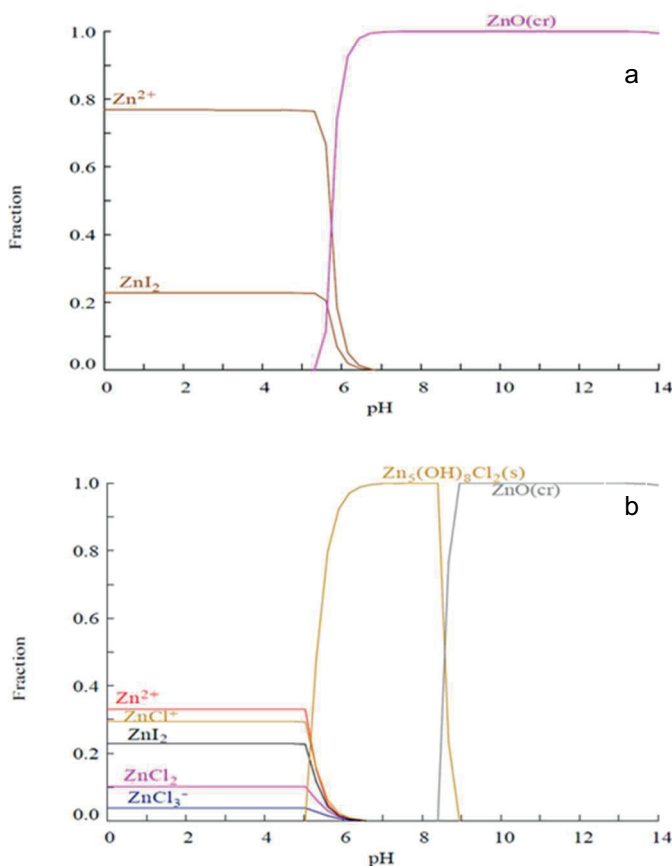
Figure 5.7. Total fraction of zinc species as a function of pH (1 through 14) in the anolytes (a) without NaCl containing $[Zn^{2+}]$ = 1.5 mol·L^{-1}, $[I^-]$ = 4.5 mol·L^{-1} and (b) with NaCl containing $[Zn^{2+}]$ = 1.5 mol·L^{-1}, $[I^-]$ = 4.5 mol·L^{-1} and $[Cl^-]$ = 1.5 mol·L^{-1}.

Next, to better interpret the equilibrium chemistry of these two electrolytes, chemical equilibrium diagrams were calculated using the Hydra-Medusa software and the equilibrium database. **Figure 5.7** shows the distribution of zinc species as a function of pH in the two anolytes of without and with NaCl, when total concentrations of ion are $[Zn^{2+}]$ = 1.5 mol·L^{-1}, $[I^-]$ = 4.5 mol·L^{-1} and $[Cl^-]$ = 1.5 mol·L^{-1} respectively. It is found that the amount of free Zn^{2+} decreases with the introduction of Cl^- ions in the solution, as a large number of zinc species consisting of $ZnCl_x^{(2-x)}$ (x = 1, 2, 3, 4) appear in the

NaCl added electrolyte between pH range from 1 to 6 (**figure 5.7b**). These results of forming soluble chloride salts within these lower pH ranges are in good agreement with the previously reported literatures on zinc-chloride media.[14,16–18] In fact, the correlation of Zn morphology, crystal size, nucleation mode, and concentration of Zn^{2+} and Cl^- species has been addressed in the literature concerning Zn electroplating[14]. An instantaneous nucleation mechanism is dominant under Zn^{2+} and Cl^- concentrations above certain critical values, leading to the formation of denser and more compact layers, as observed by us.
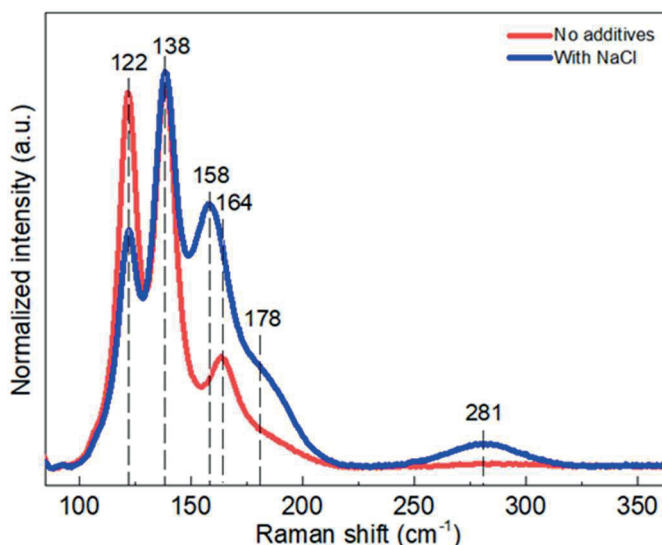
Figure 5.8. Raman spectroscopic investigation of electrolyte of 1.5 M ZnI_2:KI (at 0% SOC), red and blue colour represents electrolyte composition without and with 1.5 M NaCl supporting electrolyte.

For practical insights into the functionality of Cl^- ions in the solution chemistry, the electrolyte solutions, with and without NaCl, were studied by Raman spectroscopy. As illustrated in **figure 5.8**, the Raman spectrum of the solution, without NaCl contains three distinctive bands at 122, 138, and 164 cm^{-1} respectively. These three bands observed are in good agreement with the previous works reported in the literatures,[10,19] and can be assigned to the A1 symmetry modes, which correspond to the symmetric stretching vibrations of the $[ZnI_4]^{2-}$, $[ZnI_3]^-$ and $[ZnI_2]$ complexes, respectively. Additionally, a shoulder at 178 cm^{-1} can be assigned to the T_2 symmetry mode of the $[ZnI_4]^{2-}$ complex.[19] The addition of NaCl in the solution leads to the appearance of a new peak at 281 cm^{-1} which can be assigned to the stretching mode of $[ZnCl_4]^{2-}$ complex[20]. This correlates with the significant decrease in the intensity of the peak associated to the $[ZnI_4]^{2-}$ complex in relation to the other peaks, allowing us to conclude that namely inside this complex chloride substitutes iodide. Additionally, the peak related to the $[ZnI_2]$ complex shifts to the lower energies to 158 cm^{-1} in the Cl^- media, which might be related to the influence of the Cl atoms, and the

appearance of more complex Cl⁻-I⁻ vibrations. Overall, this comparison of Raman spectra of NaCl-based electrolyte with the standard electrolyte confirms the coordination interactions between Zn^{2+} and Cl⁻ ions results in the formation of $ZnCl_4^{2-}$ anions.

5.3.4 Effect of NaCl as an additive on the cathode side

Apart from the improvements in the electrochemical performance of Zn/Zn^{2+} half-cell by the introduction of NaCl, in parallel, CV results also reveal the enhancements of I_3^-/I^- redox reaction in terms of kinetics and reversibility. Hence, to understand the role of Cl⁻ ions in the solution chemistry of cathode half-cell, Raman spectroscopy was performed on fully charged catholyte (67% SOC), without and with NaCl (**figure 5.9**).

As shown in the Raman spectrum of NaCl-free electrolyte, two intense bands related to the polyiodides appear at 111 and 156 cm⁻¹, which can be assigned to the symmetric stretch of triiodide (I_3^-) and outer symmetric stretch of pentaiodide (I_5^-), respectively[10,21]. Besides, a weak band appears at 235 cm⁻¹, attributed to the polyiodide species. With the addition of NaCl to the solution, a new band appears at 230 cm⁻¹ which represents the formation of the soluble I_2Cl^- complex in the catholyte.

This result of the formation of I_2Cl^- complex is in good agreement with the report published by M. Mousavi et al.[22] This observation agrees with the statement made by M. Mousavi et al, about the stabilisation of free iodine and freeing up the I⁻ ions by the formation of I_2Cl^- [22] and I_2Br^- [6] complexes during charging. In fact, other interhalide species such as ICl and $[ICl_2]^-$ have been identified to be electrochemically formed in mixed I⁻ and Cl⁻ systems, although at higher [Cl⁻]/[I⁻] ratios.[23] In addition, the calculation of the chemical equilibrium diagrams (**figure 5.10**) exhibits the the formation of I_2Cl^- complex and availability of more free I⁻ ions with the NaCl-supported catholyte (**figure 5.10d**), adding another parallel justification. Finally, this Cl⁻ ions complexation with I_2, hinders I_2 precipitation thus enhancing the ZIFB performance by withholding the battery capacity and CE (**figure 5.3a** & **5.4a**).

5
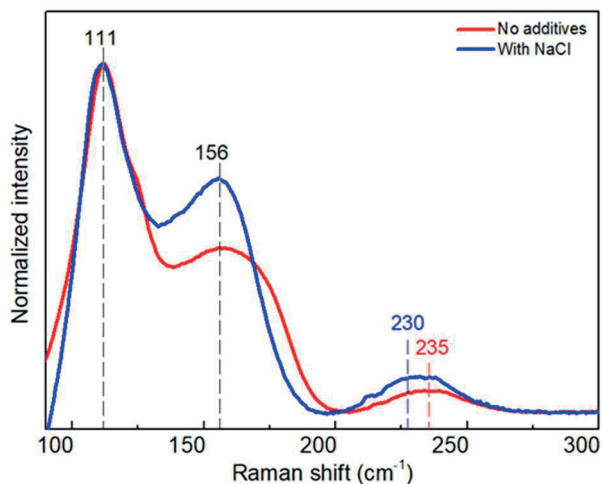
Figure 5.9. Raman spectra of the charged (67% SOC) catholytes consisting with and without NaCl.
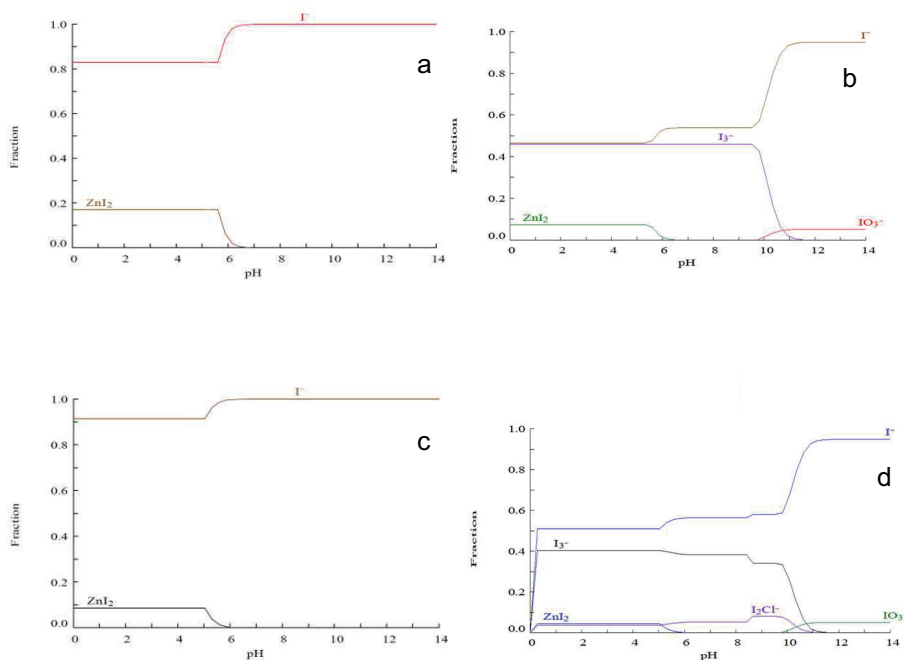
Figure 5.10. Total fraction of I^- species as a function of pH (1 through 14) in the catholytes. Without NaCl containing $[Zn^{2+}]$ = 1.5 mol·L^{-1}, $[I^-]$ = 6.5 mol·L^{-1} at (a) 0% SOC, (b) 67% SOC, and with NaCl containing $[Zn^{2+}]$ = 1.5 mol·L^{-1}, $[I^-]$ = 6.5 mol·L^{-1} and $[Cl^-]$ = 1.5 mol·L^{-1} at (c) 0% SOC, (d) 67% SOC.

In another angle, this observed excellent and stable coulombic efficiency of the ZIFB with NaCl supported electrolyte (**figure 5.3a**) can also be associated to the preferential monovalent cation transfer across the N117 CEM. The similar ions and water transport analysis we had discussed in **Chapter 4**. In fact, the volume comparison between the cycled and fresh catholytes (**figure 5.11**) shows no change of volume with NaCl-based catholyte even after 100 cycles, whereas a decrement has been observed in the NaCl-free catholyte. Water transport is associated to cation diffusion along the ionic exchange membrane. As summarized in literature, divalent cations such as Zn^{2+} ions, possesses higher charge density, hydration enthalpy, and water uptake capacity, therefore carrying more water molecules through the membrane. Although these divalent cations have lower self-diffusion coefficient and lower mobility than monovalent cations such as K^+ and Na^+,[24–27] in the absence of NaCl, after initial diffusion of K^+ through the N117 CEM, Zn^{2+} is prone to transfer from catholyte to anolyte, in order to compensate differences in the ionic strength. In the presence of NaCl, the K^+ and Na^+ are the dominant migrating carriers through the membrane, thus, restricting the mobility of Zn^{2+} and the water transfer from catholyte to anolyte, thus suppressing volume imbalance during cycling. This explanation adds another angle to the positive impact of NaCl-based solution chemistry in the long-term ZIFB cycling with excellent capacity retention.

5
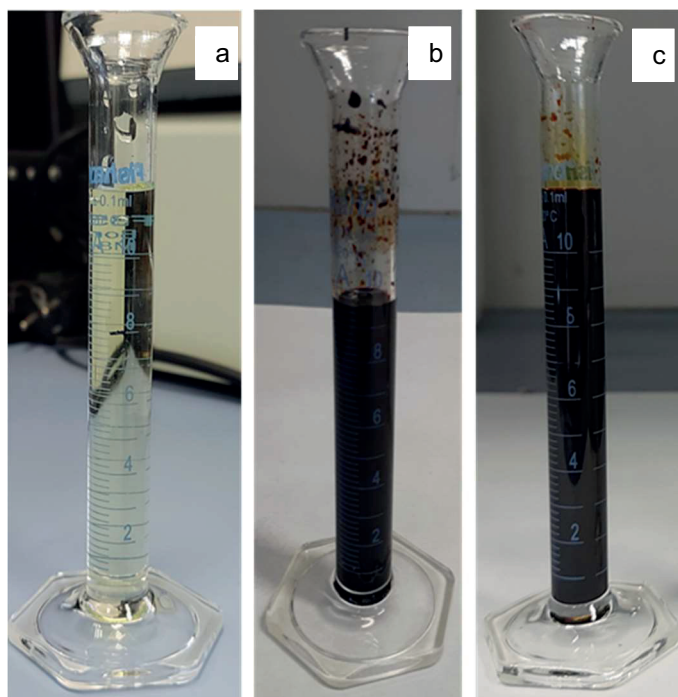
Figure 5.11. Optical images of volume variations of catholytes (picture taken after reverse flow) (a) before cycling; (b) after 15th charge-discharge cycle without NaCl; (c) after 100th charge-discharge cycle with NaCl.

5.4 Conclusion

In summary, NaCl is proposed as an effective supporting electrolyte for ZIFBs long-term cycling. Inspired by the CV results of improved redox reversibility of Zn/Zn^{2+} in the presence of Cl$^-$ ions, accordingly, this electrolyte enables the ZIFB to achieve a stable cycling performance for 100 cycles with 77% of capacity retention, along with highly reversible Zn plating and stripping. In addition, SEM image and XRD results reveal the densely packed morphology of Zn plating in the presence of Cl$^-$ ions. Moreover, the prediction of the coordination interactions between Zn^{2+} and Cl$^-$ ions by chemical equilibrium diagrams, further confirmed by Raman spectroscopy and proves the formation of soluble, ZnCl$_4{}^{2-}$ anions, which are responsible for stabilization of Zn^{2+}, hence improving the Zn/Zn^{2+} redox electrochemical reaction. On the positive half-cell side, Cl$^-$ ions complexation with I$_2$, frees up the I$^-$ ions and blocks solid I$_2$ precipitation thus enhancing the ZIFB performance by retaining the battery capacity. Last but not the least, participation of Na$^+$ ions in catholyte solution chemistry, restricts the mobility of large, hydrated Zn^{2+}, thus blocking water migration from catholyte to anolyte by showing no volume change after 100 cycles, greatly reflects on the excellent capacity retention throughout the cycling.

5

5.5   References

1. B. Li, J. Liu, Z. Nie, W. Wang, D. Reed, J. Liu, P. McGrail, and V. Sprenkle, *Nano Lett.*, **16**, 4335–4340 (2016).

2. H. Pan, B. Li, D. Mei, Z. Nie, Y. Shao, G. Li, X. S. Li, K. S. Han, K. T. Mueller, V. Sprenkle, and J. Liu, *ACS Energy Lett.*, **2**, 2674–2680 (2017).

3. C. Xie, H. Zhang, W. Xu, W. Wang, and X. Li, *Angew. Chemie - Int. Ed.*, **57**, 11171–11176 (2018).

4. J. Zhang, G. Jiang, P. Xu, A. G. Kashkooli, M. Mousavi, A. Yu and Z. Chen, *Energy Environ. Sci.*, **11**, 2010–2015 (2018).

5. C. Xie, Y. Liu, W. Lu, H. Zhang, and X. Li, *Energy Environ. Sci.*, **12**, 1834–1839 (2019).

6. G. M. Weng, Z. Li, G. Cong, Y. Zhou, and Y. C. Lu, *Energy Environ. Sci.*, **10**, 735–741 (2017).

7. S. J. Banik and R. Akolkar, *Electrochim. Acta*, **179**, 475–481 (2015).

8. D. P. Trudgeon, K. Qiua, X. Lia, T. Mallick, O. O. Taiwob, B. Chakrabarti, V. Yufit, N. P. Brandonb, D. C-Garciac, A. Shah, *J. Power Sources*, **412**, 44–54 (2019).

9. S. Hosseini, S. J. Han, A. Arponwichanop, T. Yonezawa, and S. Kheawhom, *Sci. Rep.*, **8**, 1–11 (2018).

10. B. Li, Z. Nie, M. Vijayakumar, G. Li, J. Liu, V. Sprenkle and W. Wang, *Nat. Commun.*, **6**, 1–8 (2015).

11. Q. P. Jian, M. C. Wu, H. R. Jiang, Y. K. Lin, and T. S. Zhao, *J. Power Sources*, **484**, 229238 (2021).

12. F. W. Thomas Goh, Z. Liu, T. S. A. Hor, J. Zhang, X. Ge, Y. Zong, A. Yu, and W. Khoo, *J. Electrochem. Soc.*, **161**, A2080–A2086 (2014).

13. D. J. Mackinnon, J. M. Brannen, and V. I. Lakshmanan, *J. Appl. Electrochem.*, **10**, 321–334 (1980).

14. G. Trejo, R. Ortega B, and Y. Mecis V, *J. Electrochem. Soc.*, **145**, 4090–4097 (1998).

15. K. Amini and M. D. Pritzker, *Electrochim. Acta*, **268**, 448–461 (2018).

16. K. Ogle and S. Morel, *EUROCORR 2004 - Eur. Corros. Conf. Long Term Predict. Model. Corros.*, 1–5 (2004).

17. W. Miao, I. S. Cole, A. K. Neufeld, and S. Furman, *J. Electrochem. Soc.*, **154**, C7 (2007).

18. S. Thomas, N. Birbilis, M. S. Venkatraman, and I. S. Cole, *Corrosion*, **68**, 1–9 (2012).

19. H. Wakita, G. Johansson, M. Sandström, P. L. Goggin, and H. Ohtaki, *J. Solution Chem.*, **20**, 643–668 (1991).

20. G. Pulletikurthi. M. S. Ghazvini, T. Cui, N. Borisenko, T. Carstens, A. Borodin and F. Endres, *Dalt. Trans.*, **46**, 455–464 (2017).

21. P. H. Svensson and L. Kloo, *Chem. Rev.*, **103**, 1649–1684 (2003).

22. M. Mousavi, G. Jiang, J. Zhang, A. G. Kashkooli, H. Dou, C. J. Silva, Z. P. Cano, Y. Niu, A.Yu, and Z. Chen., *Energy Storage Mater.*, **32**, 465–476 (2020).

23. C. L. Bentley, A. M. Bond, A. F. Hollenkamp, P. J. Mahon, and J. Zhang, *Anal. Chem.*, **88**, 1915–1921 (2016).

24. E. R. Nightingale, *J. Phys. Chem.*, **63**, 1381–1387 (1959).

25. D. W. Smith, *J. Chem. Educ.*, **1**, 1–3 (1977).

26. G. Xie and T. Okada, *J. Electrochem. Soc.*, **142**, 3057–3062 (1995).

27. A. Goswami, A. Acharya, and A. K. Pandey, *J. Phys. Chem. B*, **105**, 9196–9201 (2001).

5

Thesis: Part II

Unbiased photocharging of redox flow batteries: Solar RFBs

Part II of this thesis is dedicated to the solar powered RFBs. This part is arranged with two chapters: Chapter 6, where solar powered VRFB has discussed and the solar powered ZIFB has discussed in the Chapter 7. In these two chapters, we have worked with two different solar cells materials by keeping in mind the tackling some sort of challenges in the solar RFBs prospects as well as environmental concerns. Reader will get in detail description in the respective chapters.

Chapter 6

Solar VRFB powered by CIGS photovoltaics
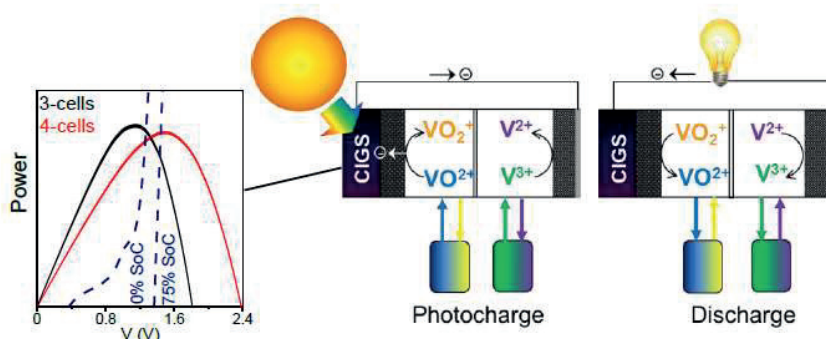
The main parts of this chapter have been published in Sustainable Energy & Fuels as ¨Adaptation of Cu(In, Ga)Se$_2$ photovoltaics for full unbiased photocharge of integrated solar vanadium redox flow batteries¨ by Sebastián Murcia-López, Monalisa Chakraborty, Nina M. Carretero, Cristina Flox, Joan Ramón Morante, and Teresa Andreu (Sustainable Energy Fuels, 2020, 4,1135).

The published text and figures have been marginally edited and reorganised for this thesis chapter, and parts of the introduction were omitted as that was already introduced in the general introduction chapter (Chapter 1). Additional figures from the Supporting information of the article have been included in the chapter.

A note to the reader:

It is important to mention that the main focus of this thesis is to optimise the RFBs part, towards achieving a successful integration with the solar cell. Therefore, no in depth description about the solar cells used in this thesis, has been briefed.

The schematic illustration with electrochemical reactions of VRFB has already been described in the general introduction chapter (**Chapter 1-section 1.3**). Afterward, the general working scheme, history and current state of the art, backlogs, and open questions related to SRFB have also been discussed in **Chapter 1** section **1.4**.

6

6.1 Publication abstract

The integration of photovoltaics and vanadium redox flow batteries (VRFBs) is a promising alternative for the direct conversion and storage of solar energy in a single device, considering their inherent higher energy density versus other redox pairs. However, this integration is not seamless unless the photovoltaic system is customised to the voltage needs of the battery, which, unlike artificial photosynthesis, continuously increases with the state of charge. We have developed an integrated solar VRFB with adapted low-cost Cu(In, Ga)Se$_2$ modules of 3 and 4 series-connected cells (solar efficiency of the mini-solar module 8.1%), and considering the voltage requirements (1.3–1.6 V), we have evaluated the influence of the photovoltaic operation region on the final efficiency of the solar VRFB. Full unbiased photocharge under 1 Sun illumination has been achieved resulting in high energy (77%), solar-to-charge (7.5%), and overall round trip energy conversion efficiencies (5.0%) exceeding the values reported in the literature for other solar VRFBs, thus demonstrating the feasibility and intrinsic potential of adapting low-cost commercial photovoltaics to such energy storage systems.

6.2 Introduction

6.2.1 Scope of our work based on the current state of the art

Chalcopyrite Cu(In, Ga)Se$_2$ (CIGS) light absorbers are a promising alternative to other thin-film PV technologies[1] and even to crystalline silicon, given their higher absorption coefficient that allows using smaller amounts of active material.[2,3] Therefore, CIGS-based PVs have been commercialised and become more cost competitive (see **table 6.1** for comparison with other technologies) with efficiency values of ~16% (world record higher than 20%)[1,4,5] and an additional advantage: CIGS can be directly grown on flexible substrates like metal foil, which can facilitate the integration into electrochemical cells. Moreover, several studies on photoelectrochemical water splitting using CIGS[6,7] are good examples of how they can be properly customized to solar VRFBs. Recently Bae et al. theoretically correlated several parameters of solar RFBs with single photo-absorbers and found that with low electrolyte resistance, commercial PV materials such as c-Si, GaAs, and CIGS are promising alternatives[8]. Though this is not a straightforward task for achieving unbiased photocharge, the PV must properly match the energy requirements of the VRFB, considering also that the cell voltage varies with SOC, while the overpotential available for photocharge (or the photocurrent) decreases at high SOC.[9] Therefore, unlike systems coupling, PVs and energy storage systems counting on power electronic devices for tracking the PV maximum power point (MPP) and controlling the charge of the battery, the main challenge to be solved for the integrated system is matching the PV MPP and the RFB considering the inherent potential shift of the latter.[10] This is a critical aspect at high SOC, especially in systems with single photoabsorbers,[8] but must be carefully considered even in devices using two photoelectrodes or PV configurations with tandem or multi-junction approaches.

Very recently, an organic solar RFB based on viologen and ferrocene-derived redox couples with c-Si photoelectrodes has achieved a promising stable performance and solar round-trip energy efficiency of 5.4%,[11] attributed to the proper matching between the photoelectrodes and the redox pairs, moving a step forward into the development of more efficient systems.

Table 6.1. Comparison of fabrication cost for different thin film PV technologies versus multi-crystalline Si.

Photovoltaic technology	Cost
Multicrystalline Silicon	Levelised cost of energy: 0.51 US$/$W_{DC}$[a]
	Minimum sustainable pricing: 0.27-0.36 US$/$W_{DC}$[b]
CIGS	Levelised cost of energy: 0.4 US$/$W_{DC}$[a] with a potential decrease to 0.22 US$/$W_{DC}$ in next-generation fabrication (larger area).
	Minimum sustainable pricing: 0.4-0.5 US$/$W_{DC}$[b]
CdTe	Minimum sustainable pricing: 0.35-0.45 US$/$W_{DC}$[b]

6

---

[a]White Paper for CIGS Thin Film Solar Cell Technology, Zentrum für Sonnenenergie- und Wassersroff Forschung Baden-Württemberg, Stuttgart (2015).
Available at: http://cigs-pv.net/wortpresse/wp-content/uploads/2015/12/CIGS-WhitePaper.pdf
[b]NREL: An Analysis of the Cost and Performance of Photovoltaic Systems as a Function of Module Area.
Technical Report NREL/TP-620-67006 (2017).
Available at: https://www.nrel.gov/docs/fy17osti/67006.pdf
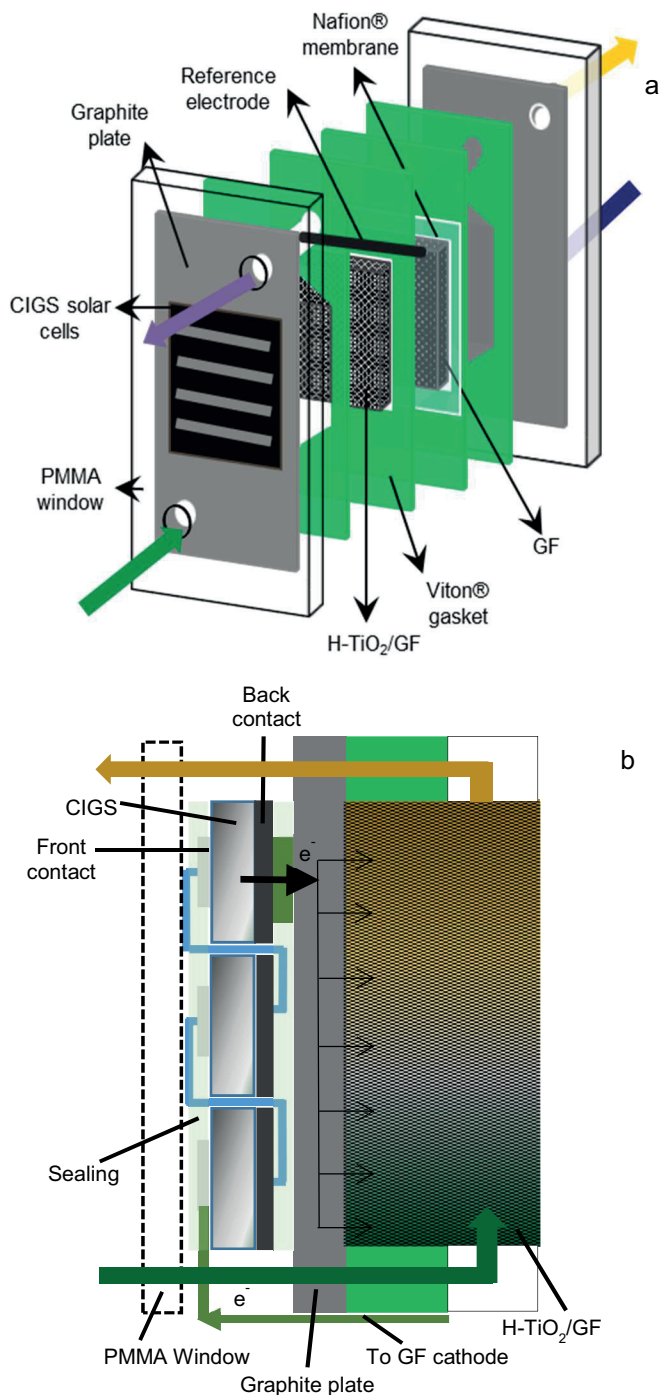
Figure 6.1. Schematic of the integrated solar VRFB with the CIGS solar cells (a) the cell was assembled with a reference electrode in the negative side, close to the H–TiO$_2$/GF. Cross-sectional view (b) of the electron transfer between the PV mini-module and the anode side.

6.2.2 Objectives of the chapter

Based on this, we have carried out the integration of adapted CIGS (as "embedded" photoelectrodes) into VRFBs without additional power electronics (**figure 6.1**), by evaluating two mini-modules fabricated from commercial thin-film PVs in two different battery configurations (symmetric V4/V4 and asymmetric V4/V3).

Highlights of the chapter

To obtain the main objectives, the following investigations have carried out:

- ○ At first, the evaluation of CIGS mini-modules to determine the MPPs and selection of the VRFB operation regimes.

- ○ Adaptation for the integration of the mini-modules towards achieving proper matching of the operating conditions during photocharge of the battery.

- ○ Assessment of the influence of different charging conditions (constant and variable charge power) on the final performance of the solar VRFB with these mini-modules.

6

6.3 Materials preparation and experimental methods

6.3.1 CIGS PV module preparation
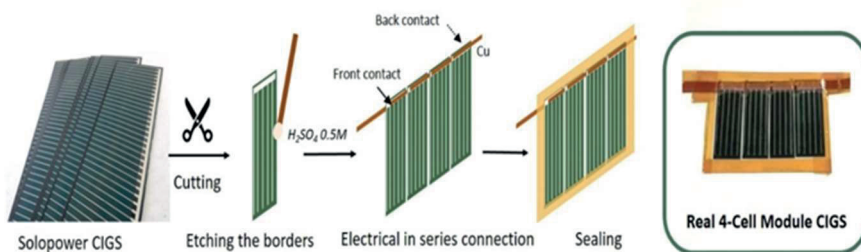
Figure 6.2. Schematic of the procedure for the CIGS mini-modules preparation.

A thin film photovoltaic based on $Cu(In, Ga)Se_2$ (CIGS) supported on stainless steel was purchased from SoloPower®. For the preparation of the PV modules, commercial CIGS foil was cut into small cells of 5.1–5.3 cm^2 geometric area, after which the borders were etched with 0.5 M H_2SO_4 to dissolve the metal oxides and eliminate electrical shunts. The series-connected photovoltaic cells were wired with a conductive Cu sheet and Ag electrically conductive transfer tape (ECATT 9703, 3MTM). Hence, 3 and 4-cell PV modules (namely, 3CM and 4CM) were prepared, attaining different open circuit potentials and current densities. The PV modules were sealed to avoid contact with the electrolyte, with optically clear double-sided adhesive tape (THORLABS) and kapton® adhesive tape (Dupont). A scheme showing the different steps is included in **figure 6.2**. The final geometric areas of the 3CM and 4CM were 15.3 and 20.4 cm^2, respectively. The i–V characteristic curves of the CIGS modules were recorded at 30 mV·s^{-1} using a VMP3 BioLogic potentiostat and a PEC-L01 solar simulator (PECCELL Technologies, Inc.) with an AM 1.5G filter and 1 Sun irradiation.

6.3.2 Preparation of carbon electrodes

Hydrogenated rutile TiO_2 nanorods were directly grown over commercial graphite felt (GF, of 6 mm thickness purchased from Mersen S.A., Spain), to be used as the negative electrode of the VRFB cell. First, GF was pre-treated in plasma device with O_2 atmosphere for 10 min for each face, to activate the carbon-based and increase its active surface area, labelled as GF-HT (**figure 6.3a**). Hydrogenated TiO_2-GF electrode (labelled as TiO_2:H coated GF) was prepared by following a previously reported hydrothermal synthesis procedure by our research group.[12–14] The titania precursor, 5 ml of titanium butoxide, was added into 60 ml of 1:1 (v:v) (HCl:H_2O) solution. The obtained mixed precursor solutions and GF were placed in a Teflon-sealed autoclave (100 ml, Parr Instrument Co.) and heated up at 100ºC for 14 hours. After the synthesis, a white solid precipitate was observed over the surface of GF. The as-prepared samples were cleaned by immersion in water and dried in a vacuum oven at 60ºC overnight. Afterwards the sample was annealed in oxygen atmosphere

for 4 hours at 500ºC in order to remove chlorine impurities. Finally, a thermal treatment in Ar/H$_2$ atmosphere at 500ºC for 4 hours was applied to the sample, showing the original white colour. This sample was labelled as TiO$_2$:H coated GF electrode. These electrodes have previously shown a good performance for the V^{3+}/V^{2+} side reaction in VRFBs, associated with the combination of (i) higher surface hydroxylation leading to a higher presence of active sites for V^{3+} reduction, (ii) HER inhibition, and (iii) partial hydrogenation improving the charge transfer at the electrode/electrolyte interface.[12] On the positive side of the VRFB cell, O$_2$-plasma etched graphite felt was used. The geometric area of the electrodes was 10 cm^2.
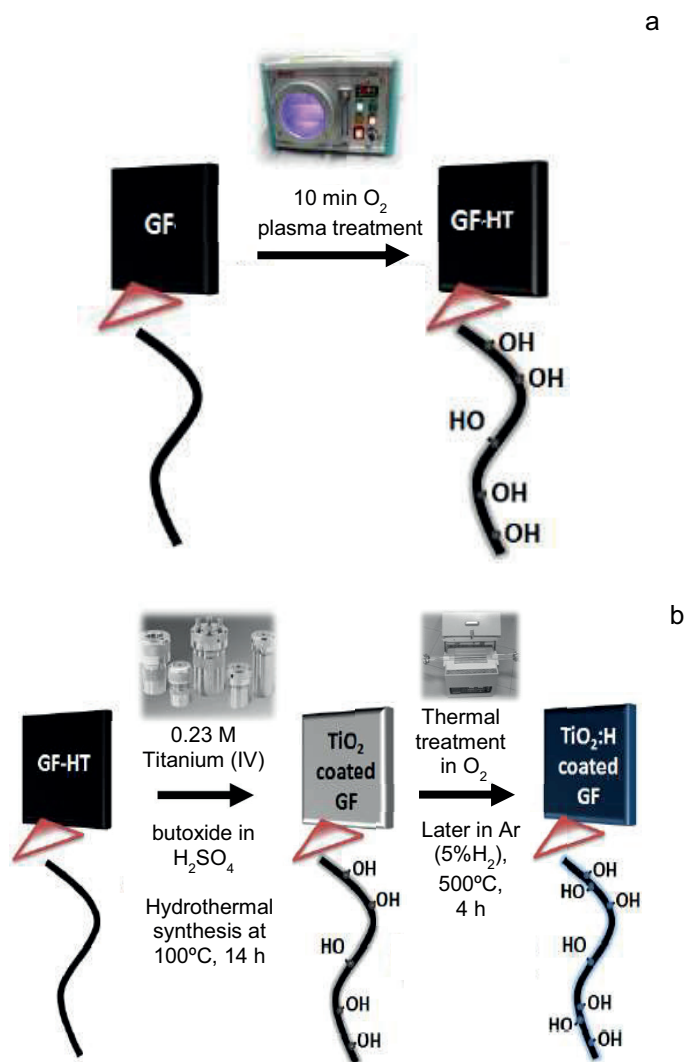
Figure 6.3. Scheme of the GF electrode synthesis process. (a) oxygen plasma treatment, (b) steps to implement hydrogenated TiO$_2$ coated on GF.[12]

6.3.3 VRFB cell preparation

A note to the reader:

The general cell assembling followed a similar procedure that was described in the Lab-scale ZIFB single cell preparation (**Chapter 2**, **section 2.2.1**). Except for components such as electrodes, current collectors are different in this vanadium chemistry from the Zn-I⁻ chemistry. The details about the VRFB cell preparation are briefed below:

A lab-scale adapted electrochemical cell with the following components: a poly (methyl methacrylate) (PMMA) window on one side, two graphite plates as current collectors (Electrocell), pre-treated Nafion 117 CEM (the treatment procedure has been mentioned in the general experimental **Chapter 2**, **section 2.2.1**) and the treated graphite felts, TiO_2:H coated GF on the negative side and GF-HT on the positive side in the corresponding compartments, were used to assemble the flow cell. The electrolyte was circulated by a peristaltic pump with a flow rate of 13 mL·min⁻¹ and an estimated linear flow velocity of ~8.1 cm·min⁻¹, for a 16% felt compression and a porosity of 0.8 (under compression). The "embedded" CIGS module was integrated by coupling on the negative side of the cell, between the PMMA window and the graphite current collector. Additionally, a reference electrode (Ag/AgCl) was inserted into the negative side of the cell and the individual potentials vs. reference were followed during tests (**figure 6.1a**). The individual potentials have been referenced to the standard hydrogen electrode (SHE) by means of the expression:

$$V_{SHE} = V_{Ag/AgCl} + 0.059\,pH + 0.199\,V.$$

Electrogeneration

Before performing the cycling, the V^{3+} anolyte was electrogenerated through a galvanostatic charge (30 mA·cm⁻²) using 0.5 M $VOSO_4$ in 3 M H_2SO_4 electrolyte on both sides (twice the volume of catholyte than anolyte), after which V^{2+} and VO_2^+ were obtained in the negative and positive sides, respectively. Afterward, half of the volume was extracted from the catholyte and a galvanostatic discharge (30 mA·cm⁻²) was performed to obtain V^{3+} and VO^{2+} as the starting catholyte and anolyte for the actual charge/discharge tests. Different volumes in the range of 7.5–15 mL in each compartment were used during the different tests.

6.3.4 Full VRFB tests

Galvanostatic charge-discharge experiments

Prior to the integration with the photovoltaic modules, electrochemical tests with the full cell were conducted, to validate the galvanostatic charge-dischargep process and determine the operating voltages of the system. The cycling was conducted at constant current densities (10 and 20 mA·cm⁻²) and the cell voltage was followed in order to control the charge-discharge of the battery. Additionally, a reference

electrode was put inside the cell so that the individual voltages in the positive (E_p) and negative (E_n) sides could be followed.

Finally, an additional test by charging up to several SOC values and performing linear scan voltammetry (LSV) in the two-electrode configuration at 40 mV·s⁻¹ was carried out.

Photocharge experiments

During the photocharge experiment, the CIGS modules were illuminated at 0 V with a PEC-L01 solar simulator (PECCELL Technologies, Inc) equipped with a 300 W Xe arc lamp and AM 1.5G filter. A cross-sectional view with the PV mini-module configuration and the electron transfer to the anolyte can be found in **figure 6.1b**. The irradiance was adjusted to 100 mW·cm⁻² (1 Sun) using a silicon diode (XLPF12-3S–H2-DO; Gentec-EO). Both the photocurrent generated at the PV system and the open circuit potential in the cell were followed with a VMP3 BioLogic potentiostat.

Although the potential depends on specific conditions such as temperature and concentration of active species, in general terms, the cell voltage in VRFBs varies between 1 and 1.55 V from the thermodynamic point of view and as predicted by the Nernst equation (**eqn. 6.1**), where C_x is the given concentration of the vanadium ions involved in the overall reaction on the positive and negative sides. Under real operation, these values are expected to increase because of intrinsic overpotential and ohmic losses.

$$E = E^0 + \frac{RT}{nF} \cdot \ln \frac{[C_{VO_2} + C_{V2} + C_{H^+}^2]}{[C_{VO2+} + C_{V3+}]} \qquad (6.1)$$

Therefore, after reaching OCP values of 1.5–1.6 V and by considering the theoretical charge capacity and the colouration of the electrolytes, the battery was considered fully charged, the illumination was stopped and the galvanostatic discharge at a selected current density was carried out up to a cell voltage limit of 0.7 V, corresponding to a fully discharged battery under our established conditions.

6.3.5 V4/V4 VRFB test

Several solar rechargeable flow batteries have already been proposed in the literature, combining different vanadium species, which adapt the overall redox potential to the photovoltage provided by the photoactive material. In particular, symmetrical configurations such as $VO_2^+,VO^{2+}\|VO^{2+},V^{3+}$ (V4/V4) and $VO^{2+},V^{3+}\|$ V^{3+},V^{2+}, have been successfully photocharged with TiO_2[15] and CdS/CdSe[16] materials. However, these battery configurations do not possess the overall potential compared to the full VRFB, as seen from the electrochemical reactions of full VRFB (see **eqn. 1.3 – 1.4** in **Chapter 1**), and the following reactions for V4/V4 VRFB:

Positive Electrode:

$$VO_2{}^+ + 2H^+ + e^- \leftrightarrow VO^{2+} + H_2O \qquad E^0 = 1.0 \text{ V vs. SHE} \qquad (6.2)$$

Negative Electrode:

$$V^{3+} + H_2O \leftrightarrow VO^{2+} + 2H^+ + e^- \qquad E^0_{VO^{2+}/V^{3+}} = 0.34 \text{ V vs. SHE} \qquad (6.3)$$
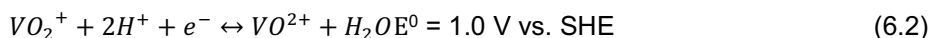
$$\leftarrow \text{charge} \qquad \rightarrow \text{discharge}$$

Overall V4/V4 battery:

$$VO_2{}^+ + V^{3+} \leftrightarrow 2VO^{2+} \qquad E^0 = 0.66 \text{ V vs. SHE} \qquad (6.4)$$

Besides the measurements performed under normal conditions with a full VRFB (V3/V4), a preliminary test with a symmetrical configuration using the same parent active species on both sides (VO^{2+}, namely V4/V4) was carried out with the 3CM module. In this kind of RFB, the same parent molecule is oxidised and reduced on each half-cell[17,18]. Thus, the charge parameters were evaluated by following the same photocharge procedure: initially, 10 mL of fresh VO^{2+} electrolytes (0.5 M $VOSO_4$ in 3 M H_2SO_4) were added into each compartment (without electrogeneration), after which the PV was illuminated under the same conditions as those in the full cell test. This way, the thermodynamic overall cell voltage decreased to around 0.66 V and the photocharge was completed after obtaining V^{3+} and $VO_2{}^+$ in the negative and positive reaction sides, respectively.

A note to the reader:

The efficiency calculations of the PV cell following the solar RFBs can be found in the general experimental chapter (**Chapter 2, section 2.3.5, Figures of merit of SRFBs).**

6

6.4 Results and discussion

6.4.1 VRFB performance evaluation under galvanostatic conditions
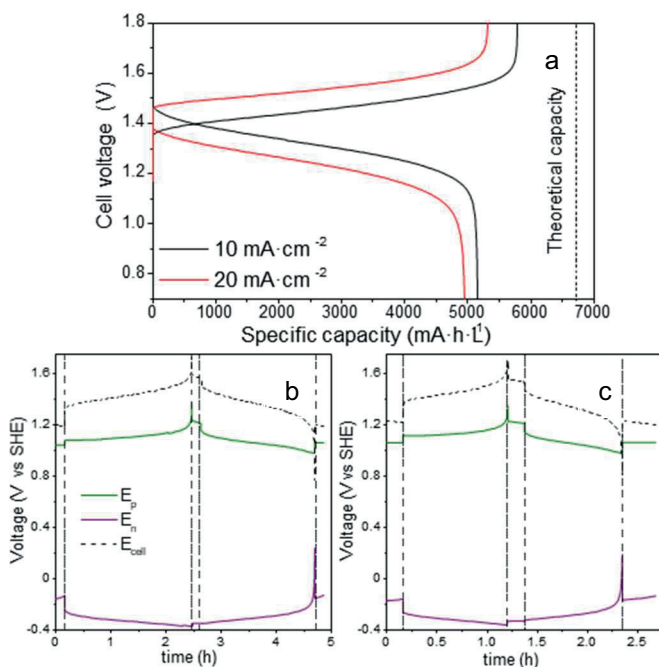
Figure 6.4. Charge-discharge profiles during the full cell measurements under galvanostatic conditions. (a) Variation of the cell potential vs. capacity during charge-discharge at different current densities; individual potentials in the positive (E_p) and negative (E_n) sides (V vs SHE), and estimated E_{cell} (V), during charge-discharge at (b) 10 and (c) 20 mA·cm^{-2}.

The obtained curves during galvanostatic cycling are presented in **figure 6.4**, including the E_p, E_n, and E_{cell} during the charge-discharge at different current densities. Despite the small decrease in the capacity seen at higher current densities, the battery provides acceptable efficiency and electrolyte utilization values (**table 6.2**). As expected, the voltage efficiency decreases with the increase in the current density, although the coulombic efficiency is positively affected. The individual half-cell potentials, however, show a certain unbalance between both sides: during charge, the E_p increases indicating the positive side is fully charged, so that all available VO^{2+} has been oxidized to VO_2^+ and parasitic reactions such as oxygen evolution might start, while the potential in the negative side, E_n, is still decreasing, indicating that unreacted V^{3+} species are still present. The opposite situation is observed during the cell discharge: the non-fully charged negative side is discharged before the positive as seen by the steep decrease in the E_n. A more detailed analysis of these potentials shows, for instance, that the negative side starts to charge at ~-0.26 V_{SHE}, which is in good agreement with the thermodynamic potential for this half-reaction. The positive side, on the contrary, starts charging at ~1.12 V_{SHE}, which

implies overpotentials that might be associated to ohmic losses in the cell, especially in the membrane.

Table 6.2. Estimated efficiencies values and electrolyte utilisation for the galvanostatic cycling of the cell.

Current density (mA·cm^{-2})	Coulombic efficiency (%)	Voltage efficiency (%)	Energy efficiency (%)	Electrolyte utilisation (%)
10	89	90	80	77
20	93	82	76	74

Energy efficiencies of 80-76% are obtained for the galvanostatic charge at 10 and 20 mA·cm^{-2}, respectively. Although slightly higher values have been reported for other VRFB with TiO_2:H coated GF electrodes on the negative side and evaluated at similar current density,[5] the lower vanadium concentration used in the present study and some fluidic aspects regarding the use of different cell configurations account for the minor efficiency decrease. Besides the efficiency values, as seen by the potential profile during the charge, at lower current density, the cell potential varies between 1.3 V in the discharged cell up to 1.8 V for the fully charged one. At higher current densities, the voltage efficiency decreases and the initial charging potential increases up to around 1.45 V. Clearly, as previously stated, an unbiased photocharge can only be achieved with a PV system providing these voltages working at similar current densities.

6.4.2   CIGS characterisation

The single selected CIGS cell displays a V_{OC} of 0.6 V and short circuit current of 35 mA·cm^{-2} (**figure 6.5a**), leading, in our case, to an estimated solar cell efficiency of 10.3%. Considering these values and the cell voltages observed in the charge-discharge cycling of the VRFB, we determined that modules of at least 3 or 4 series-connected cells (namely 3CM and 4CM) were necessary for full unbiased photocharge. As seen in the J–V curves in **figure 6.5a,** we obtained the expected V_{OC} values: 1.8 and 2.4 V for the 3 and 4-cell modules, respectively (**table 6.3**). However, slightly lower fill factors were obtained and the solar cell efficiencies in the multi junctions decreased to around 8.4–8.1%. This can be attributed to additional shunt resistances introduced during the preparation of the modules. Alternative interconnection strategies such as monolithic interconnection[19] could probably lead to better solar cell efficiencies than the tabbing method used in the present work. Although the V_{OC} values of the series-connected modules are high enough to accomplish the unbiased photocharge, it is also necessary to consider the potential variation of the battery cell voltage with the SOC, leading to a constant shift in the operation point of the PV system as shown in **figure 6.5b**. The significant photocurrent decrease (**figure 6.5a**) in the 3CM (from 21% in the 4CM to around 59%

in the 3CM) clearly illustrates that the operation point in this system is not optimum, so this probably might limit the photocharge of the VRFB.
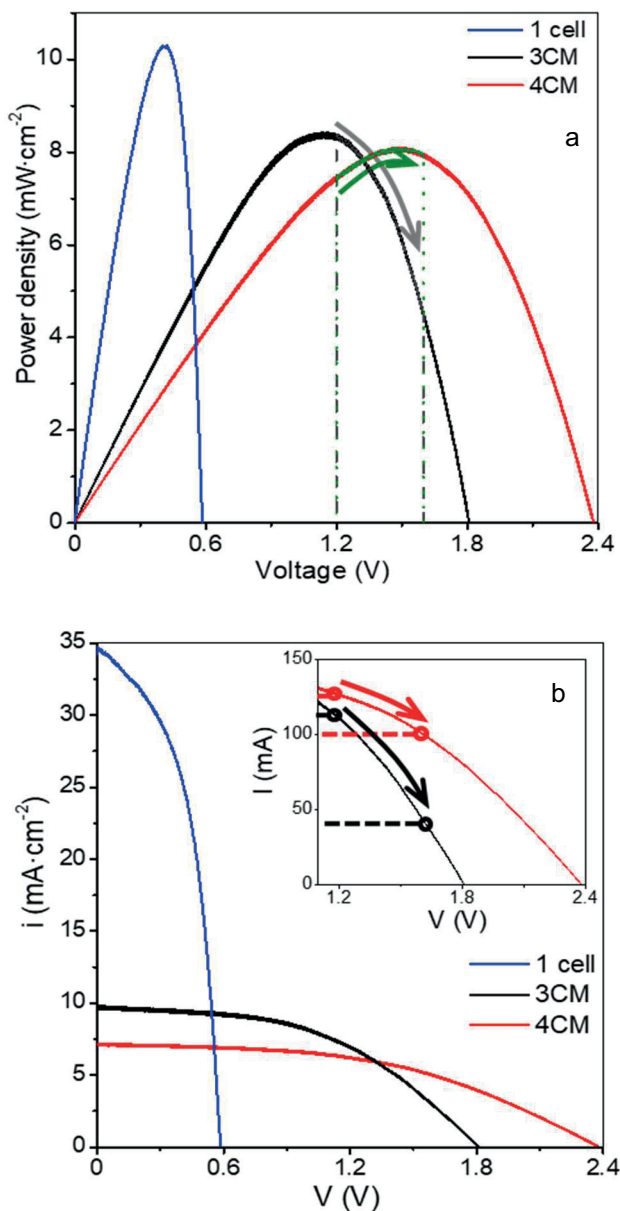
Figure 6.5. Characteristics curves of CIGS modules under 1 sun illumination. (a) J-V curves. In the inset, the operation region during the photocharge (1.2 – 1.6 V), and (b) P-V curves. The marked areas indicate the voltage window during the photocharge step.

Table 6.3. Estimated solar cell efficiencies, fill factors, open circuit voltages, and voltages at maximum power point under AM1.5G illumination at 1 Sun, with the different CIGS modules.

CIGS Module	η (%)	FF (%)	V_{oc} (V)	V_{mp} (V)
1 cell	10.3	50.0	0.6	0.4
3CM	8.4	48.0	1.8	1.2
4CM	8.1	48.0	2.4	1.5

6.4.3   3CM evaluation: V4/V4 and full VRFB

As a proof of concept, the 3CM was first evaluated in a RFB with a symmetrical $VO_2^+,VO^{2+}||VO^{2+},V^{3+}$ (V4/V4) configuration, because of the lower standard redox potential between these two vanadium pairs (E^0= 0.66 V, **eqn. 6.4**).[17] For this purpose, the same starting VO^{2+} electrolyte was used in both compartments. The charge profile and the photocurrent density are shown in **figure 6.6**. The full charge was completed after ~2.3 h of illumination, as indicated by the steep increase in the cell potential. At this point, the irradiation was stopped and the system remained in that open-circuit condition, reaching ~0.8 V. Besides the colour change of the electrolytes, the calculated capacity attained under photocharge (~6700 mA·h·L^{-1}) indicates that a SOC of around 98.5% was reached (namely, VO_2^+ and V^{3+} formed on the positive and negative sides, respectively). Therefore, the suitability of the 3CM for Unbiased photocharge of the V4/V4 system was demonstrated, although certainly, this configuration has limited practical interest given its lower energy density versus a full VRFB. Additionally, further optimization for specific reaction kinetics (in particular for the V^{3+}/VO^{2+} half-reaction) would be necessary, as seen from the relatively high charge overpotential observed in this system, and probably justified by the use of an electrode enhanced for the V^{3+}/V^{2+} reactions on the anode side.

6
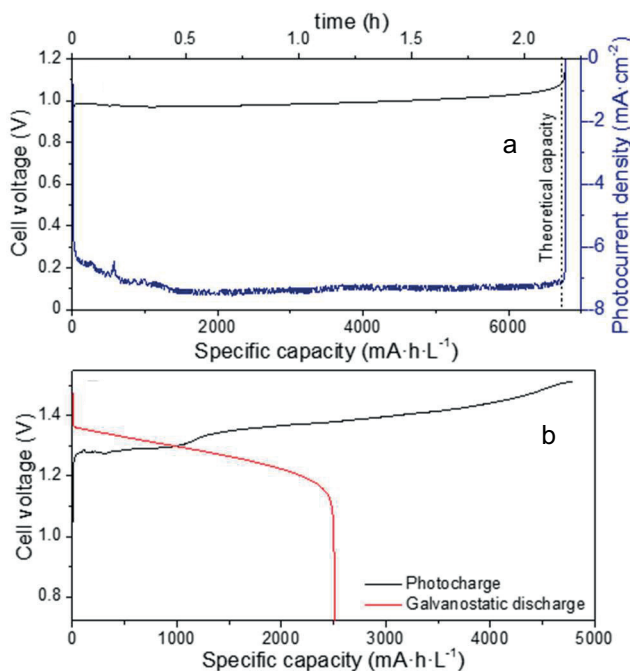
Figure 6.6. 3CM results: (a) photocurrent density and cell voltage evolution during the unbiased photocharge of the integrated V4/V4 configuration, (b) photocharge/discharge curves of the full VRFB configuration, the galvanostatic discharge was carried out at 10 mA·cm^{-2}.

Once the V4/V4 configuration was assessed, the electrolytes were substituted by fresh VO^{2+} and V^{3+} solutions in the catholyte and anolyte, respectively, in a regular full VRFB configuration. The cell was assembled as described in **figure 6.1** and the photocharge/discharge was evaluated. As seen in **figure 6.7,** the variation of the cell potential during the photocharge remarkably matches the photocurrent of the PV system, which continuously drops with time as the SOC (i.e., cell potential) increases. The cell voltage slowly increased until reaching 1.5 V and remained practically constant afterward, with a photocurrent below 1.0 mA·cm^{-2}. After reaching a photocurrent of 0.5 mA·cm^{-2} with a cell voltage of ~1.52 V and considering the slow capacity increase (inset of **figure 6.7**), the photocharge was stopped and the galvanostatic discharge started.
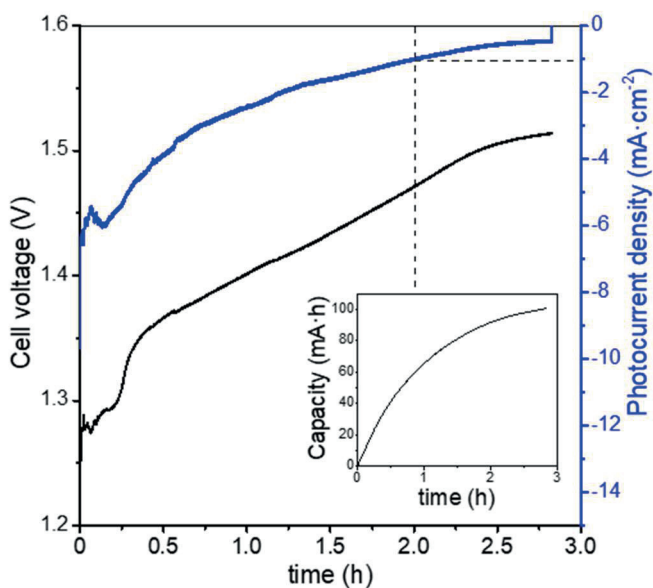
Figure 6.7. Cell voltage (black) and photocurrent density (blue) evolution during the photo-charge of the full VRFB with the integrated 3CM under 1 Sun illumination. The battery was cycled with 10 mL of catholyte and anolyte.

The fact that no steep increment was observed in the cell potential suggests two features, different from the galvanostatic charge or the photocharge with 4CM (as discussed later): (1) the 3CM is not able to provide enough voltage for other parasitic reactions such as water splitting to occur and (2) the photocurrent of the 3CM has such a significant decrease after a certain SOC, that the photocharge stops being effective and the overall cell potential (i.e. SOC) is not affected. Indeed, the galvanostatic discharge (**figure 6.6b**) also reflects the difference between the photocharge and discharge capacities, resulting in poor coulombic and energy efficiencies (52 and 47%, respectively) and electrolyte utilization of only 37.5%.
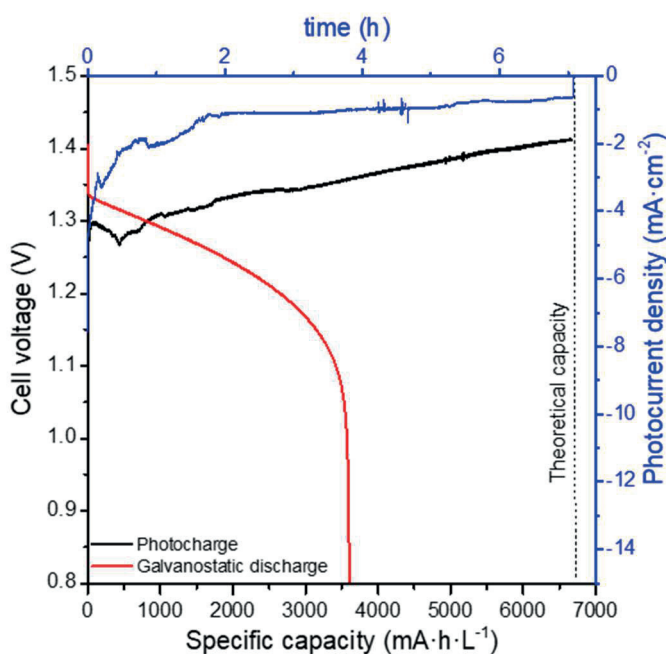
Figure 6.8. Cell voltage (black) and photocurrent density (blue) evolution during the photocharge of the full VRFB with the integrated 3CM under ~0.5 Sun illumination. The battery was cycled with 10 mL of catholyte and anolyte.

An additional test with the 3CM under lower irradiation (50 mW·cm^{-2}, in order to work at ~1 mA·cm^{-2}) and by leaving the battery to fully attain the maximum charge capacity is shown in **figure 6.8**. Despite reaching the theoretical capacity after more than 7 h of photocharge, the cell voltage remained lower than 1.4 V. Moreover, the battery only reaches half of the capacity during discharge, with a coulombic efficiency and electrolyte utilization of ~54%. Interestingly, the solar-to-charge (η_{STC}) and overall round trip energy conversion (η_{RT}) efficiencies[20,21] calculated for the battery with the integrated 3CM under both conditions show very similar values. This way, average η_{STC} and η_{RT} of 3.2 and 1.5–1.6% are respectively obtained, which, compared to the solar efficiency of 8.4%, evidences the limited power attained by the 3CM, inadequate for fully charging the VRFB. As observed in **figure 6.5b**, assembling the system with this module implies that the photocharge starts at the PV MPP and moves towards a lower power direction (patterned zone). Interestingly, the η_{STC} for the V4/V4 configuration with the 3CM leads to a higher value of 7.0%, demonstrating its suitability for photocharging a symmetrical V4/V4.

6.4.4 4CM evaluation in a full VRFB
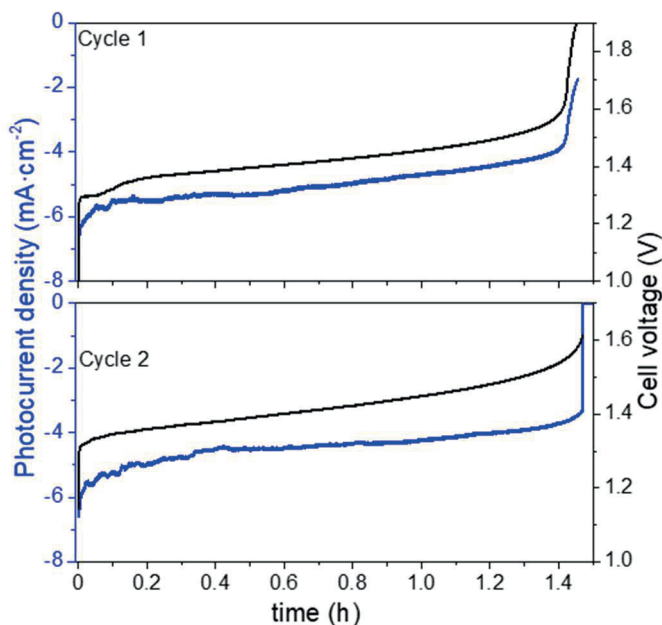
Figure 6.9. Variation of the photocurrent density and cell voltage during unbiased photocharge (cycles 1 and 2) with the 4CM.

Considering the limited operation of the 3CM, the battery was assembled with the 4CM in the full VRFB configuration. As seen in **figure 6.9**, the photocurrent of the PV module slightly varied between 6 and 4 mA·cm^{-2}, while the ones reached by the 3CM drastically dropped from 6 to 1 mA·cm^{-2}. In fact, the profiles of the curves were more stable with this module and the cell potential steeply increased after reaching high SOC. This way, full photocharges were achieved, leading to capacities close to the theoretical value. Thereafter, the galvanostatic discharges were carried out, leading to discharge capacities of ~5000 mA·h·L^{-1} as shown in **figure 6.10.** In general, except for a minor imbalance observed during the first cycle, the battery shows a stable behavior during cycling, attaining very similar efficiencies and capacities with successive photocharges/discharges. Furthermore, the energy efficiency reached (77%) is similar to that of the galvanostatically charged VRFB (**table 6.4**).
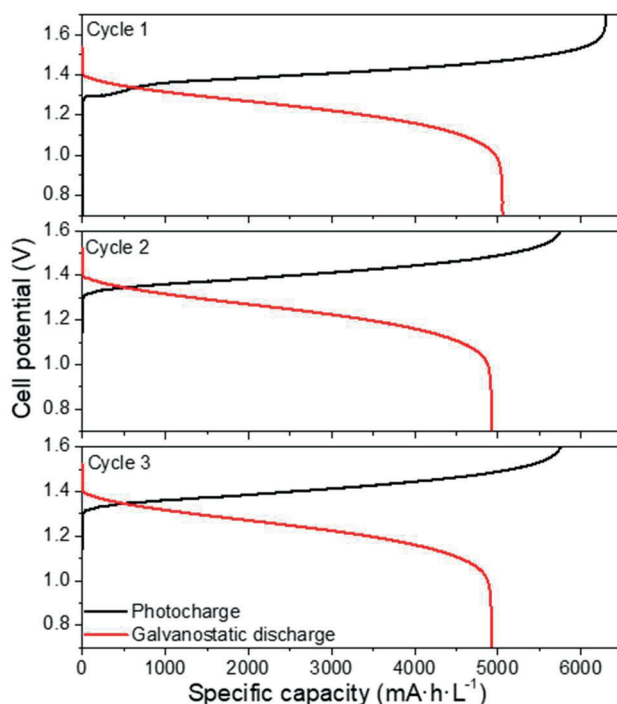
Figure 6.10. Photocharge/discharge curves of the VRFB with the 4CM. The galvanostatic discharge was carried out at 10 mA·cm^{-2} (5 mA·cm^{-2} per PV area).

Table 6.4. Estimated efficiencies and discharge electrolyte utilisation for the different VRFBs.

Configuration	CE (%)	VE (%)	EE (%)	Electrolyte utilisation (%)
3CM	52	90	47	38
4CM (cycle 2)	85	90	77	74
Galvanostatic @10 mA·cm^{-2}	89	90	80	77

As in galvanostatic cycling, the individual electrode potentials on the positive (E_p) and negative (E_n) sides were simultaneously recorded by using a reference electrode (**figure 6.11a**). A similar behavior is found regarding the evolution of the individual potentials of the galvanostatic charge-discharge: during photocharge, the E_p varies between 1.1 and 1.25 V$_{SHE}$, close to the thermodynamic potential of the VO^{2+}/VO_2^+ redox reaction and seems to more promptly increase after all the available VO^{2+} is oxidised, while the E_n steeply increases during discharge, after all the V^{2+} is re-oxidised to V^{3+}. These results suggest that a minor imbalance also observed in the galvanostatic measurements is only related to the VRFB performance, rather than to

136

the photovoltaics. However, as seen by the reached OCP of ~1.5 V and by the electrolyte colouration before and after photocharge (**figure 6.11b**), both compartments reach a high SOC.
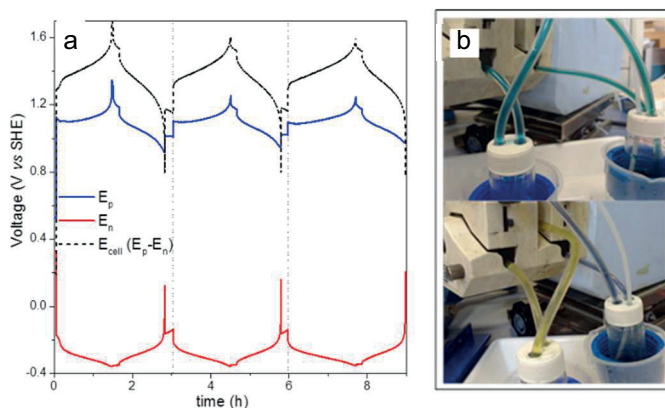
Figure 6.11. (a) Evolution of the E_p, E_n, and E_{cell} (followed by the reference electrode) during the photocharge/discharge with the 4CM, and (b) variation of the electrolytes' colours before (up) and after (down) photocharge.

An additional comparison in terms of the power density gained during charge is included in **figure 6.12a**, where we compare the photocharge with 3CM, 4CM, and galvanostatic conditions. While the power density constantly increases in the galvanostatic charge operating at a constant current with a concomitant voltage increase, the power density with the 3CM continuously decreases (the photocharge starts at the MPP) and the one by the 4CM remains almost constant before reaching high SOC. In the 4CM, the minor photocurrent decrease is compensated by the continuous increase of the cell voltage in the battery. Ultimately, the specific energy density during the photocharge with the 4CM is even higher than that of the galvanostatic charge (845 versus 887 mW·h·cm^{-2}·L^{-1}). For comparison, the power density during the V4/V4 experiment with the 3CM is also included, showing a constant value. Despite the lower power, explained by the lower cell voltage under this configuration, the 3CM is again demonstrated to be suitable for photocharging a V4/V4 VRFB.

Linear scan voltammetry (LSV) was carried out on the battery at different SOCs, and the comparison of the i–V curves of the two modules is shown in **figure 6.12b**. At 0% SOC, the crossing point between the VRFB and the 3CM curves already overpasses the MPP of the PV, and a maximum photocurrent of 100 mA can be expected (~6.5 mA·cm^{-2} per PV area). For the 4CM, however, the MPP is not overpassed below a 75% SOC. This fact confirms that from the point of view of operation conditions, the 4CM properly matches the working voltage of the VRFB.
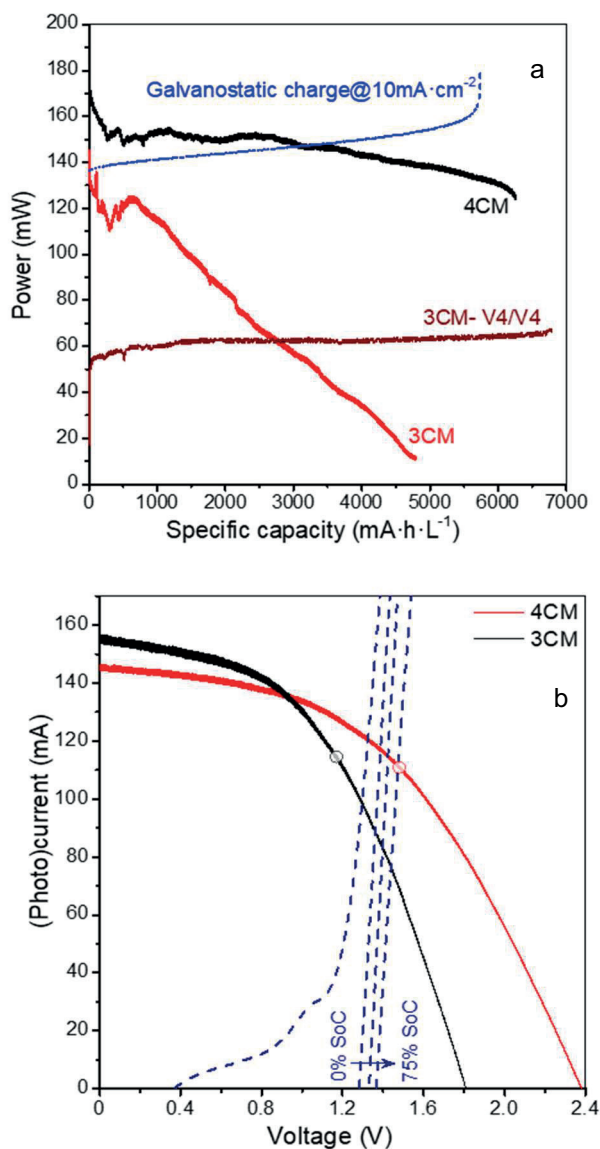
Figure 6.12. In (a), calculated evolution of the power during photocharge under different conditions: galvanostatic charge at 10 mA·cm^{-2} and photocharge with the 3CM (for a full VRFB and V4/V4 configurations) and 4CM PV system under 1 Sun illumination. In (b), comparison of i–V and LSV curves for PV modules and the VRFB at different SOC.

Besides the electrochemical efficiencies, we estimated the average η_{STC} at high SOC (for instantaneous evolution, see **figure 6.13**) and η_{RT} for the 4CM, obtaining values of 7.5 and 5.0%, respectively. In particular, the η_{RT} obtained with the 4CM is, to our knowledge, among the highest values reached for solar-driven redox flow batteries. Actually, Abruña et al.[21] and Liao et al.[20] have respectively obtained 2.8 and 1.0% efficiencies in organic/inorganic solar flow batteries providing a lower energy density than VRFBs, while the highest value has been reported by Li et al.[22], with a η_{RT} of 14.1%. Regarding solar-driven VRFBs, on the other hand, Liu et al.[19] have reported 0.6% efficiency (comparative values are collected in **table 6.5**). In fact, considering the ratio between the overall round-trip energy and the photovoltaic efficiencies, our solar VRFB with the 4CM recovers around 62% of the solar energy converted into the PV, during the discharge, which in fact confirms the suitability of this adapted module for integration in the solar VRFB.

After considering the results we have obtained, the integration of multi junctions based on commercial photovoltaic systems has been demonstrated to be the most straightforward alternative for the deployment of solar redox flow batteries, from efficiency and cost perspectives. Additional effort must be devoted to the proper fabrication of such solar modules, but also a careful consideration of the operating performance before final integration is necessary. Although the energy storage system can also be adapted, as demonstrated by our results with the 3CM and the symmetric V4/V4 configuration, the technological development of such systems probably should go in the other direction, through the adaptation of the photovoltaic system to the needs of higher power density redox flow batteries. Besides the adaptation, alternative solutions such as using solar concentration might also contribute to advance in attaining more realistic devices.

6
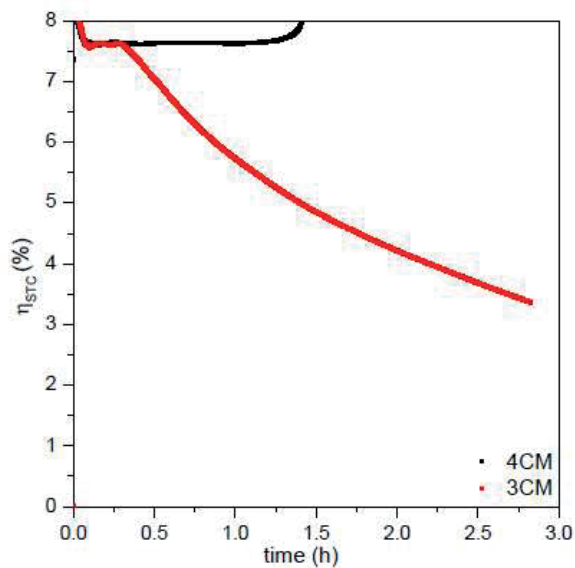
Figure 6.13. Variation of the η_{STC} during the photocharge of the full VRFB configuration with the 3CM and 4CM.

Table 6.5. Comparative table of several solar RFBs.

Type of battery	Photoelectrode/ photovoltaics	η (%)	η_{RT} (%)	Energy
[20]Organic/inorganic (AQS-iodide)	WSe$_2$	-	2.8	Discharge cell V: 0.355 V ~0.06 mW·h[a]
[23]Organic/inorganic (AQS-bromide)	c-Si	-	3.2	Discharge cell V: 0.78 V ~0.36 W·h·L^{-1}[a]
[3]Organic (4-OH-TEMPO/MVCl$_2$)	III-V tandem cell	26.1	14.1	Cell V: 1.25 V ~0.3 W·h·cm^{-2}·L^{-1}[a]
[24]Organic (DHAQ/K$_4$Fe(CH)$_6$)[b]	Ta$_3$N$_5$-GaN/Si	-	3.0[c]	0.2 W·h·L^{-1}
[25]VRFB	TiO$_2$ photoanode	-	0.6[d]	-
[26]VRFB	Triple junction TF Si	13.5[e]	8.5[a,e]	23 W·h·L^{-1} [e]
VRFB (This work)	Commercial CIGS (4 junctions)	8.1	5.0	6.25 W·h·L^{-1}

6.5 Conclusion

The integration of thin film photovoltaic modules and a full vanadium redox flow battery (VRFB) in a single straightforward device has been successfully assessed, and the influence of the intrinsic photovoltaic module on the performance has been determined. This way, a strong correlation between the photovoltaic maximum power point and the VRFB has been demonstrated, for two different Cu (In, Ga)Se2 mini-modules with 4 and 3-series-connected cells with two VRFB configurations: a symmetrical V4/V4 and full VRFB. Additionally, some simple tools for correlating the performance of the photovoltaics and the battery might be found in this work.

The mini-module with 4 series-connected cells achieves full battery photocharge with round-trip energy efficiencies (~5%) among the highest ones for solar VRFBs. In the case of the 3-cell module, a full dependence on the open-circuit potential of the battery was observed, leading to excellent performance for a symmetrical V4/V4 configuration (constant power density) and poor efficiency values in a full VRFB (decreasing power density). Finally, we have demonstrated the tremendous potential of this kind of energy storage system by customizing commercial thin film photovoltaics for the first time, which might shed light on the road for the future development of such solar batteries based on more simple configurations by using already existing technology.

6.6 Future work

From this chapter, despite the demonstration of successful unbiased photocharging of both well-established and commercialised systems: CIGS photovoltaics and VRFB, there are still some remaining challenges, which could let the further ongoing research in the solar RFBs field. The concerned issues are:

   i.   High operating voltage of VRFB.
   ii. Limited solubility of vanadium ions restricts to enhance the cell energy density.
   iii. Last by not the least, limited resources of vanadium.

These above-mentioned issues could be tackled by studying on alternative RFB chemistry, which has discussed in the next chapter (**Chapter 7**).

6.7 References

1. P. D. Matthews, P. D. McNaughter, D. J. Lewis, and P. O'Brien, *Chem. Sci.*, **8**, 4177–4187 (2017).

2. P. Reinhard, A. Chiriiii, P. Blasch, F. Pianezzi, S. Nishiwaki, S. Buecheler, and A. N. Tiwari, *IEEE J. photovoltaics*, 1–9 (2013).

3. J. Ramanujam and U. P. Singh, *Energy Environ. Sci.*, **10**, 1306–1319 (2017).

4. J. Jean, P. R. Brown, R. L. Jaffe, T. Buonassisi, and V. Bulovic, *Energy Environ. Sci.*, **8**, 1200–1219 (2015).

5. M. Powalla, S. Paetel, D. Hariskos, R. Wuerz, F. Kessler, P. Lechner, W. Wischmann, and T. M. Friedlmeier, *Engineering*, **3**, 445–451 (2017).

6. C. Ros, T. Andreu, S. Giraldo, Y. Sánchez, and J. R. Morante, *Sol. Energy Mater. Sol. Cells*, **158**, 184–188 (2016).

7. M. Chen, Y. Liu, C. Li, A. Li, X. Chang, W. Liu, Y. Sun, T. Wang, and J. Gong, *Energy Environ. Sci.*, **11**, 2025–2034 (2018).

8. Dowon Bae, G. M. Faasse, G. Kanellos, and W. A. Smith, *Sustain. Energy Fuels*, **3**, 2399 (2019).

9. K. Wedege, D. Bae, W. A. Smith, A. Mendes, and A. Bentien, *J. Phys. Chem. C*, **122**, 25729–25740 (2018).

10. A. Gurung and Q. Qiao, *Joule*, **2**, 1217–1230 (2018).

11. W. Li, E. Kerr, M-A. Goulet, H-C Fu, Y. Zhao, Y. Yang, A. Veyssal, Jr-H. He, R. G. Gordon, M. J. Aziz, and S. Jin, *Adv. Energy Mater.*, **9**, 1–8 (2019).

12. J. Vázquez-Galván, C. Flox, C. Fàbrega, E. Ventosa, A. Parra, T. Andreu, and J. R. Morante, *ChemSusChem*, **10**, 2089–2098 (2017).

13. C. Fàbrega, T. Andreu, A. Tarancon, C. Flox, A. Morata, L. C-Barrio, and J.R. Morante, *Int. J. Hydrogen Energy*, **38**, 2979–2985 (2013).

14. C. Fàbrega, D. M-Satoca, S. Ampudia, A. Parra, T. Andreu, and J. R. Morante, *J. Phys. Chem. C*, **117**, 20517–20524 (2013).

15. J. Lobato, E. Mena, and M. Millán, *ChemistrySelect*, **2**, 8446–8450 (2017).

16. J. Azevedo, T. Seipp, J. Burfeind, C. Sousa, A. Bentien, J. P. Araújo, and A. Mendes, *Nano Energy*, **22**, 396–405 (2016).

17. W. Duan, B. Li, D. Lu, X. Wei, Z. Nie, V. Murugesan, J. P. Kizewski, A. Hollas, D. Reed, V. Sprenkle, and W. Wang, *J. Energy Chem.*, **27**, 1381–1385 (2018).

18. R. A. Potash, J. R. McKone, S. Conte, and H. D. Abruña, *J. Electrochem. Soc.*, **163**, A338–A344 (2016).

19. Z. Wei, Y. Shen, D. Liu, and F. Liu, *Sci. Rep.*, **7**, 1–9 (2017).

20. S. Liao, X. Zong, B. Seger, T. Pedersen, T. Yao, C. Ding, J. Shi, J. Chen, and C. Li, *Nat. Commun.*, **7** (2016).

21. J. R. McKone, F. J. DiSalvob, and H. D. Abruña, *J. Mater. Chem. A*, **5**, 5362–5372 (2017).

22. W. Li, H. C. Fu, Y. Zhao, J. H. He, and S. Jin, *Chem*, **4**, 2644–2657 (2018).

23. M. Yu, W. D. McCulloch, D. R. Beauchamp, Z. Huang, X. Ren, and Y. Wu., *J. Am. Chem. Soc.*, **137**, 8332–8335 (2015).

24. W. D. McCulloch, M. Yu, and Y. Wu, *ACS Energy Lett.*, **1**, 578–582 (2016).

25. E. Mena, R. López-Vizcaíno, M. Millán, P. Cañizares, J. Lobato, and M. A. Rodrigo, *Int. J. Energy Res.*, **42**, 720–730 (2018).

26. T. Shibata, T. Kumamoto, Y. Nagayoka, K. Kawase, and K. Yano, *IEEE Electr. Insul. Mag.*, **30**, 48–50 (2014).

6

6

Chapter 7

A cost-effective solar-powered zinc-iodide flow battery
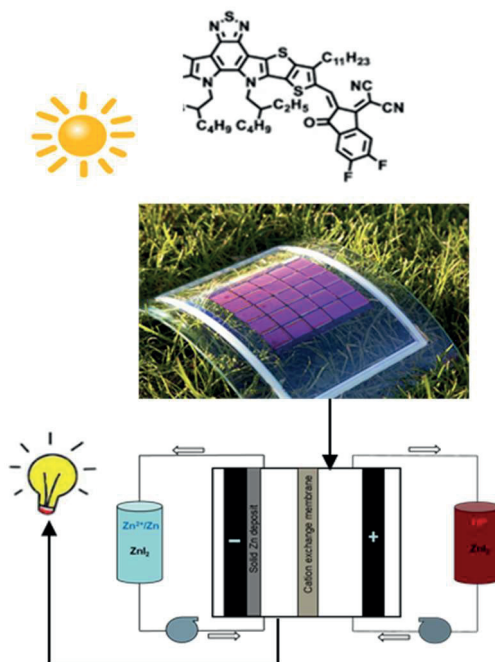
This chapter is mainly written for this thesis. A manuscript will be prepared based on the part of the results discussed in this chapter to communicate in a peer-reviewed journal in near future.

This work was performed in collaboration with Organic Nanostructured Photovoltaics Group, ICFO, Barcelona. The fabrication of the organic solar cell was done by that group in the ICFO, and the solar ZIFB experiments were carried out at the IREC facilities.

7

7.1 Introduction

The purpose of this chapter is to address the remaining issues from **Chapter 6** (discussed in **section 6.6**). As an alternative RFB chemistry, the ZIFB, we have optimised in **Part I** of this thesis (**Chapters 3 – 5**) could be a good fit to couple with the photovoltaic modules, to corroborate the lower operating voltage of ZIFB compared to VRFB. Moreover, the improved electrolyte performance after the addition of NaCl as supporting electrolyte, and another interesting point is the presence of cost-effective and hazard free, near neutral electrolyte solution made of zinc and NaCl.

A note to the reader

This chapter is focused on the device-level integration of the optimised ZIFB with the solar cells to achieve bias-free solar charging. Few optimisations were done for adapting the proper integration of the ZIFB with organic solar cell (OSC). Such as, to match the respective photocurrent density, contributed by the OSC, the size of the ZIFB active cell area has been miniaturised from 10 cm^2 (this is the size of the cell which was used for evaluating the electrochemical performances of ZIFB in the previous chapters of **Part I** of this thesis) to 1 cm^2. Apart from decreasing the cell area, to match the respective photocurrent of OSC, optimisation has been done on the electrolyte concentration and volume of ZIFB. The assembling details along with all the parameters of this new ZIFB cell are discussed later in the `Materials preparation´ part (**section 7.2.2**).

To evaluate the photocharge-discharge performance of this newly optimised ZIFB, prior to the integration with OSC, the first trial was performed with the 3 cell-modules (3CM) CIGS (the one already discussed in **Chapter 6**). Afterwards, the final integration was performed with the OSC.

As the continuation of chapter 6, no general introduction has been given here. Also, all the calculations related to the figures of merit of SRFBs followed the same as stated in the general experimental chapter (**Chapter 2, section 2.3.5, Figures of merit of SRFBs**). As a new addition to this chapter, a short overview of the current state of the art of OSC, and based on that, the scope of our work is discussed in the next section.

7.1.1   Scope of our work based on the current state of the art

OSCs show unique advantages such as light-weight, semi-transparent, low-cost solution processability, and flexible device fabrication.[1–6] Compared with inorganic-based solar cells, OSCs are made of environment friendly photoabsorber materials thus avoiding critical raw materials which are present in commercial, thin-film solar cells. For high-performance OSCs, the active layer adopts a bulk heterojunction (BHJ) architecture, where a donor and an acceptor are mixed to form a bicontinuous network.[7] Before 2015, acceptor materials were dominated by fullerenes due to their unique performance in terms of high electron affinity and mobility. However, several

shortcomings of fullerenes derivatives such as weak absorption in the visible region, and limited tunability of energy levels, resulted in the PCE still falling behind the commercialisation benchmark value of ~13%.[8,9] Afterwards, the non-fullerene acceptors (NFAs) were strongly investigated to solve these problems and effectively overcome the trade-off between the short circuit current (J_{SC}) and open circuit voltage (V_{OC}).[10–12] Past three years, the development of electron-deficient-core-based NFAs (Y6 and its derivatives) has made a breakthrough in the field of OSCs. As the classic donor and acceptor material, PM6:Y6-constructed devices have attracted a lot of studies. Due to effective exciton dissociation, suppressive charge recombination and excellent charge extraction of the OSCs containing PM6:Y6, outstanding PCEs of over 17% have been attained.[7,13]

7.1.2 Objectives of the chapter

By keeping in mind the booming era of OSCs as a promising technology for clean energy due to the advantage of non-use of critical raw materials such as indium and gallium in CIGS (critical raw materials according to European Commission), herein, we have chosen a side-by-side PM6:Y6-based OSC to integrate with the miniaturised ZIFB (discussed in `**A note to the reader**´ section) to reach an unbiased photocharge.

Highlights of the chapter

To obtain the main objectives of bias-free photocharging of ZIFB, the following investigations were conducted:

> o At first, to determine the photocharge-discharge performance of the newly optimised, miniature ZIFB, integration was done with the 3CM CIGS mini-module.
>
> o Afterwards, integration with the side-by-side PM6:Y6-based OSC was carried out.
>
> o Finally, a comparison of the solar ZIFB efficiencies was assessed with galvanostatic charge-discharge.

7.2 Materials preparation

7.2.1   Side-by-side OSC fabrication

Figure 7.1 explains the scheme of PM6:Y6-based OSC fabrication. The polymer donor PM6 and the non-fullerene acceptor Y6 (purchased from 1-Material Inc.) were used as received without any additional purification. MoO_3 and Ag pellets (Kurt J. Lesker Company) were used as received. 0.15 M of sol-gel ZnO (SG-ZnO) precursor solution was prepared by dissolving zinc acetate dihydrate (Sigma-Aldrich, 99 mg) and ethanolamine (Sigma-Aldrich, 27 mg) in 2-methoxyethanol (Sigma-Aldrich, 3 mL) and the solution was stirred at 60 °C for 2 h to complete the hydrolysis reaction in air and then stirred at room temperature for 12 h. Photoactive layer solution of PM6:Y6 (1.0:1.2) with a total concentration of 16 mg/mL was prepared in chloroform and stirred at room temperature overnight in a N_2-filled glovebox and additive 1-chloronaphthalene (CN Sigma-Aldrich, 0.5% by volume) was added 40 min prior to spin-coating.
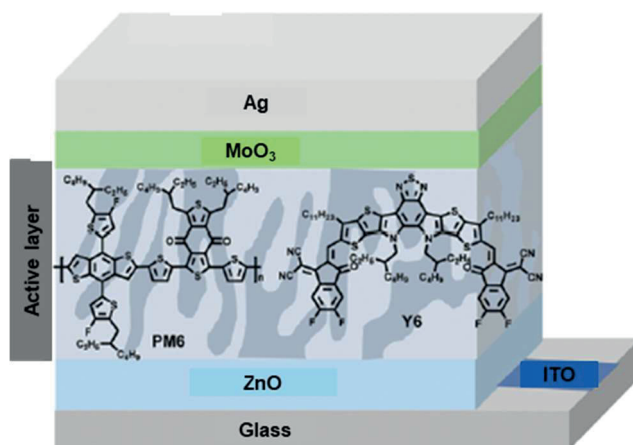
Figure 7.1. Schematic diagram of PM6:Y6 based organic solar cell. (Adapted from Guo et al.).[7]

The ITO patterned substrates (LUMTEC, 15 Ω) were pre-cleaned sequentially under a sonication bath with acetone and isopropyl alcohol. Afterwards, a ~20 nm SG-ZnO electron-transporting layer was deposited and the resulting layer was thermally annealed at 150 ºC in air for 30 min. The ZnO-coated samples were transferred into a N_2-filled glovebox for spin-casting the PM6:Y6 photoactive layer. Blend solution was deposited at 3000 rpm to achieve ~100 nm of active layer thickness. Subsequently, a 5 nm thick MoO_3 layer (0.6 Å/s) followed by 100 nm of Ag (1 Å/s) was deposited sequentially by thermal evaporation ($<5 \times 10^{-6}$ mbar) through a shadow mask. The device area, defined by the overlap between ITO and top thin Ag electrodes, was 0.12 cm^2. For the experiments performed, the cells were encapsulated with glass and sealed with a UV curable adhesive (Norland Optical Adhesive 73, 1.5 min curing) before testing.

7.2.2 ZIFB cell preparation and assembling
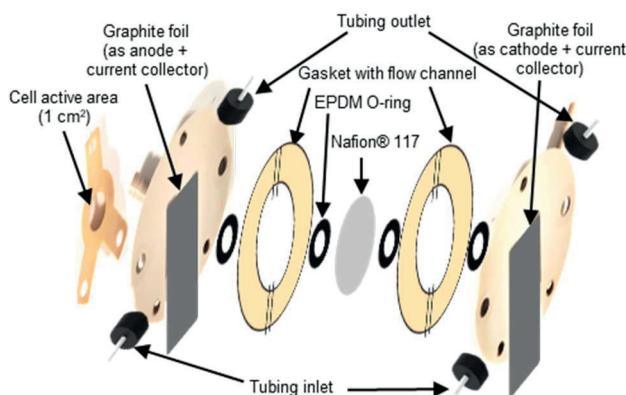
Figure 7.2. Assembling of ZIFB cell for photobattery measurements (not to scale).

A commercial photo-electrochemical cell (**figure 7.2**) made up of polyether ether ketone (PEEK) was purchased from redox.me. The horizontally mounted cell consists of 1 cm^2 of electrode active area, simple flow channel gaskets, and EPDM O-rings. Graphite foils were used as anode, cathode and current collectors, respectively. Pre-treated Nafion 117 CEM (the treatment procedure has been mentioned in the general experimental **Chapter 2**, **section 2.2.1**) was used. Electrolyte was prepared at room temperature by mixing 0.5 M ZnI_2 (≥ 98.0%, Aldrich), KI (≥ 99.5%, Merck) and sodium chloride (NaCl, ≥ 99%, Sigma Aldrich) (1:1:1) in aqueous solution (milli-Q ultrapure, deionised water). The cell was connected to 3 mL of electrolyte reservoirs on each side. Electrolyte was circulated to the cell by a peristaltic pump (Masterflex L/S series) through Microfluidic® tubing (0.1 mm of ID) at a fixed flow rate of 13 mL·min^{-1}.

The corresponding 3CM CIGS and OSC were coupled with the electrochemical cell by the wired connection for building the photobattery set-up (see **figure 7.3.a** with CIGS PV and **figure 7.3.b** with OSC).

In case of OSC, a band pass filter (RG400, THORLABS) is placed in front of the solar simulator and before the OSC, to attenuate the UV-region and pass from 400 nm only.
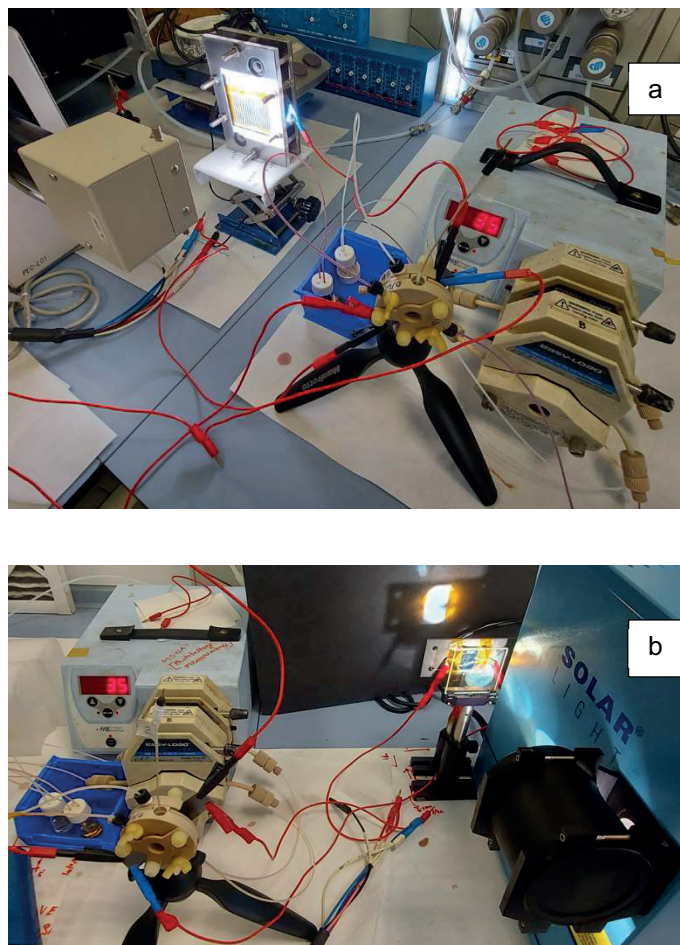
Figure 7.3. Digital photograph of running solar ZIFB. Integrated with (a) 3CM CIGS mini-module, (b) Side-by-side OSC.

As of the literature report, this PM6:Y6 photoactive material degrades in the UV region under continuous illumination.[14] Moreover, from the absorption spectra (**figure 7.4**), it could be seen that the absorption mostly happens in the visible region (for PM6 donor) and the NIR region (for Y6 acceptor). Therefore, attenuating the UV region does not interfere with the absorption region of this material.

The J–V characteristic curves of the solar cells were recorded at 20 mV·s^{-1} using a VMP3 BioLogic potentiostat and a PEC-L01 solar simulator (PECCELL Technologies, Inc.) with an AM 1.5G filter and 1 Sun irradiation. As described in the general experimental methods chapter (**Chapter 2, section 2.3.4**), the photocharge experiments were performed in the same way with the two channels from potentiostat, one connected from the solar cell to the battery to follow the photocurrent density generated upon shining, and the other was connected to the battery in open-circuit condition, to follow the battery voltage during photocharge.
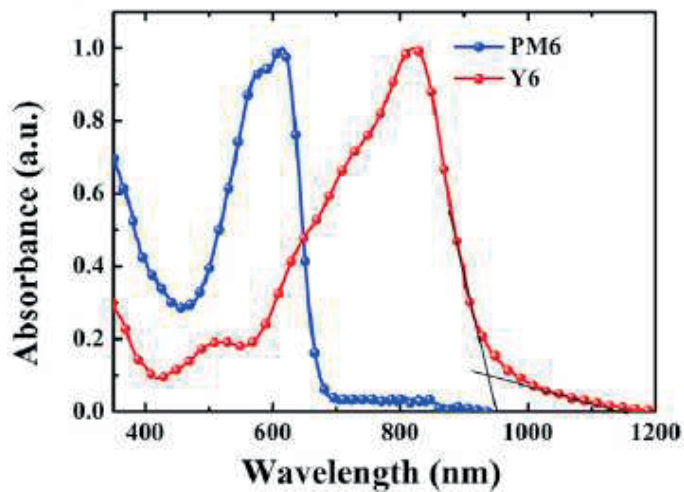
Figure 7.4. Absorption spectra of thin films of PM6 and Y6.[5]

The corresponding galvanostatic charge-discharge was carried out by keeping the same condition of upper and lower voltage cut-off that was already discussed in **Part I** of the thesis.

7.3 Results and discussion

7.3.1 ZIFB evaluation coupled with 3CM CIGS

A note to the reader:

The 3CM CIGS module was used to perform the experiments with VRFB chemistry (discussed in **Chapter 6, 6.3.3**). The same was chosen to be coupled with the ZIFB here. The idea of this experiment was to give the first trial of this newly optimised ZIFB towards achieving an unbiased photocharge.

CIGS characterisation
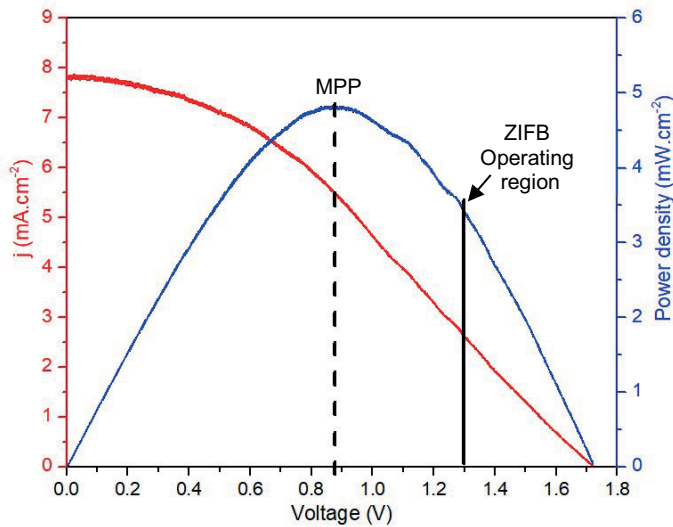
Figure 7.5. P, J-V curves of 3CM CIGS module under 1 sun illumination.

Table 7.1. Estimated solar cell efficiency, fill factor, open circuit voltage, and voltage at maximum power point under AM1.5G illumination at 1 Sun, with 3CM CIGS module.

Solar cell	η (%)	FF (%)	V_{oc} (V)	V_{mp} (V)
3-cell module (3CM)	8.40	62.30	1.72	0.86

153

Here, J-V curve characteristics (**figure 7.5**) shows partial degradation of the CIGS module. The V_{OC} and V_{MP} are 1.72 V and 0.86 V respectively (**table 7.1**). On the other side, improvement in the fill factor from 48% (**Chapter 6**) to 62.3%, could be attributed to the improved conductivity as a result of enhanced compression* of the CIGS module. The solar cell efficiency (8.4%) is the same as the former one. Due to the degradation in the MPP voltage, it could be seen that the ZIFB operating region is lying in the lower photocurrent regime (see the marked area in **figure 7.5**). Unlike the VRFB, the stable plateau nature of ZIFB charge voltage even with higher SOC (see **Chapter 3, figure 3.1**), could explain a justification to try the first trial of photocharging of ZIFB with this 3CM CIGS.

(Photo) charge-discharge

Figure 7.6 exhibits the photocharge-discharge performance of integrated 3CM-CIGS with ZIFB. The charge profile and photocurrent density are shown in **figure 7.6**. The full charge was completed ~5 h of illumination, with a pretty stable increase of the cell voltage. At this point, the illumination was stopped and the system remained in rest mode (at OCV). Besides the colour change of the catholyte into dark brown, the calculated capacity attained under photocharge (~18 Ah·L^{-1}), indicates that the ZIFB reached up to 67% SOC, which is the optimum SOC to be achieved from the ZIFB chemistry (see **Chapter 2, section 2.2.2**). The variation of the photocurrent during charging exactly matched with the photocurrent of the PV system (**figure 7.5).** Although the cell voltage does not show any steep increment throughout the charging, it slowly increased until the photocurrent reached ~0.5 mA·cm^{-2} (photocurrent density is calculated based on the area of the 3CM-CIGS. See **Chapter 6**, **section 6.3.1**), afterwards, the cell voltage was increasing stably. Once the cell reached the calculated capacity, the photocharge was stopped and the galvanostatic discharge was started at 10 mA·cm^{-2}. The discharge capacity (**figure 7.7**) depicts that the cell was completely discharged showing coulombic efficiency close to 100%, as well as very good voltage and energy efficiencies of ~82% (**table 7.2**). The low solar to charge efficiency (η_{STC}) and overall round trip efficiency (η_{RT}) are due to a mismatch between the optimum operation conditions of the battery and the PV. Nonetheless, this approach of integrating the 3CM CIGS module with this newly optimised ZIFB cell of 1 cm^2 active area, could be highlighted as a proof of concept of unbiased photocharging of ZIFB with this commercially available PV system.

---

*A note to the reader: The CIGS module was placed inside a filter-pressed Electrocell configuration with a transparent PMMA window for accessing the illumination.
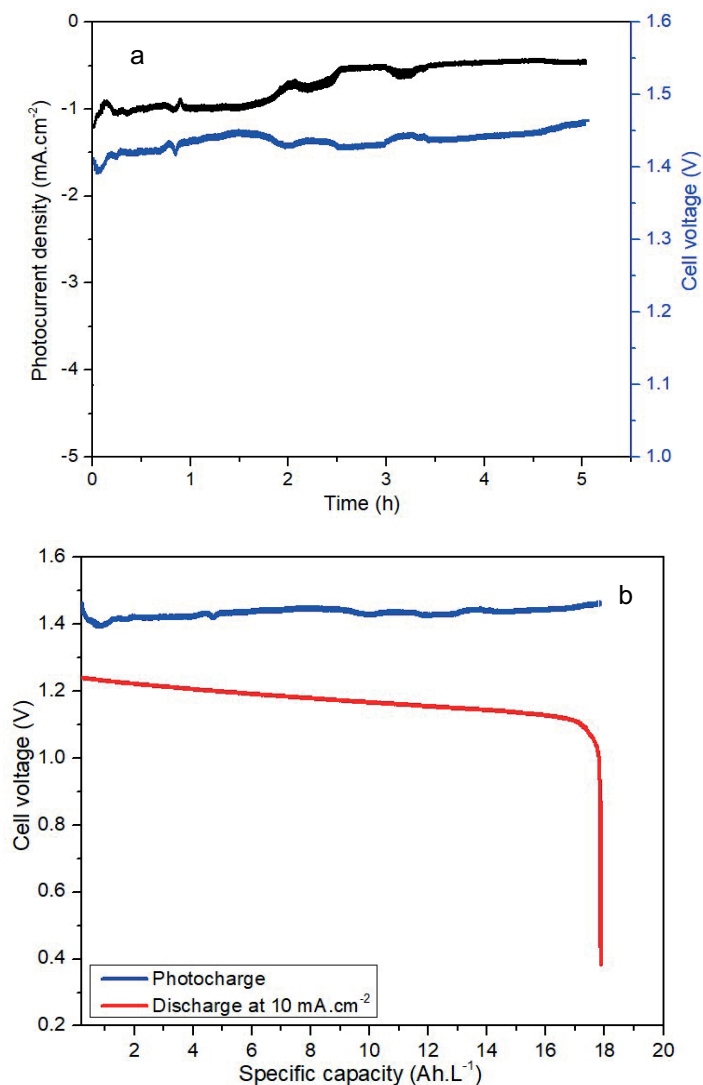
Figure 7.6. Integrated 3CM CIGS-ZIFB results: (a) photocurrent density and cell voltage evolution during the unbiased photocharge, (b) photocharge/discharge curves, the galvanostatic discharge was carried out at 10 mA·cm^{-2} (0.5 mA·cm^{-2} per PV area). Photocurrent density is calculated based on the area of the 3CM CIGS.

Table 7.2. Estimated efficiencies values of the CIGS coupled ZIFB cell.

Configuration	Coulombic efficiency (%)	Voltage efficiency (%)	Energy efficiency (%)	η_{STC} (%)	η_{RT} (%)
3CM-CIGS	99.50	81.90	81.50	1	0.82

155

7.3.2 ZIFB evaluation coupled with Side-by-side OSC

Next, to fulfil the main approach of this chapter, integration of side-by-side PM6:Y6-based OSC with ZIFB was carried out.

OSC characterisation

The P, J–V curves (**figure 7.7**) of OSC provide the V_{OC} and V_{MP} of 1.51 V and ~1.0 V respectively (**table 7.3**). Likewise, in the state-of-the-art, this PM6:Y6 based OSC exhibits a fill factor of 70.4% and an excellent efficiency (20.4%). Despite the low MPP voltage to charge the ZIFB (thermodynamically charging voltage ~1.3 V), the integration was performed for photocharge, as the photocurrent of OSC seems well enough in the ZIFB operating voltage regime, especially when comparing the low photocharging current density in the CIGS coupled ZIFB (**figure 7.6**).
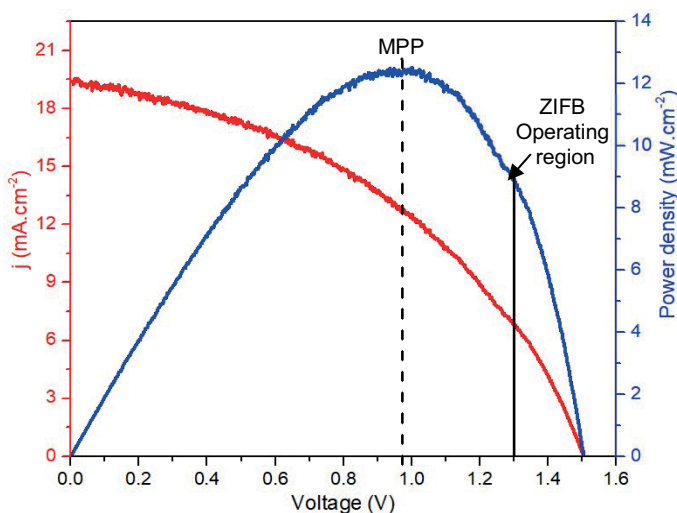
Figure 7.7. P, J-V curves of OSC under 1 sun illumination.

Table 7.3. Estimated solar cell efficiency, fill factor, open circuit voltage, and voltage at maximum power point under AM1.5G illumination at 1 Sun, with the organic solar cell.

Solar cell	η (%)	FF (%)	V_{oc} (V)	V_{mp} (V)
Side-by-side organic solar cell (OSC)	20.40	70.40	1.51	0.98

(Photo) charge-discharge
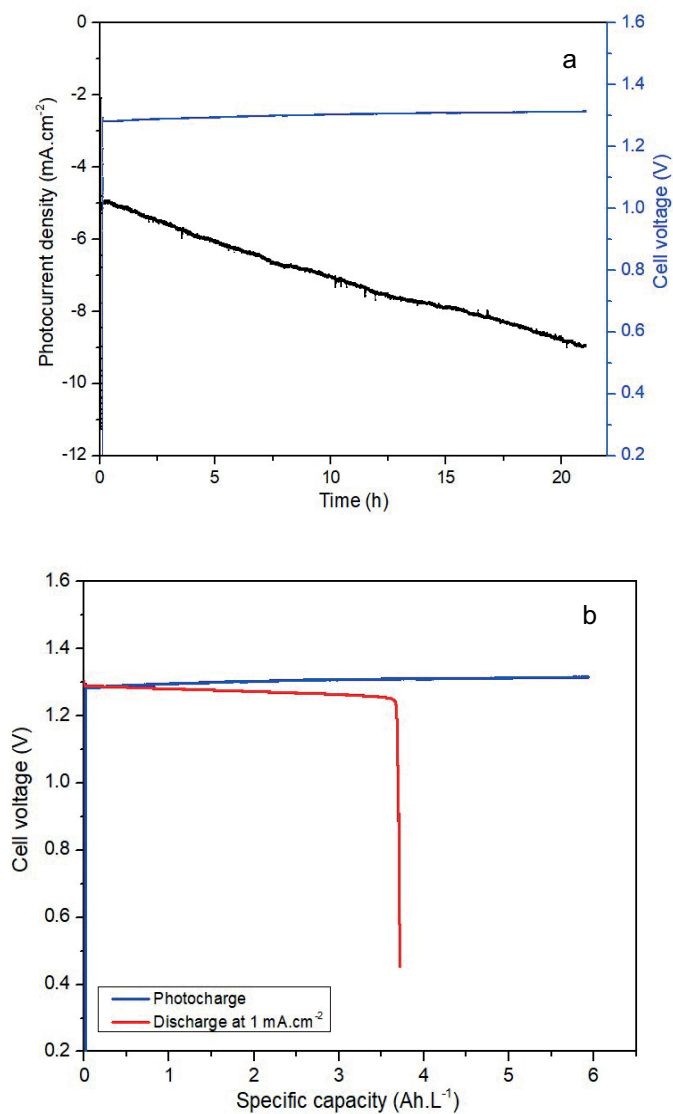
Figure 7.8. Integrated OSC-ZIFB results: (a) photocurrent density and cell voltage evolution during the unbiased photocharge, (b) photocharge/discharge curves, the galvanostatic discharge was carried out at 1 mA·cm^{-2} (7.5 mA·cm^{-2} per PV area). Photocurrent density is calculated based on the area of the OSC.
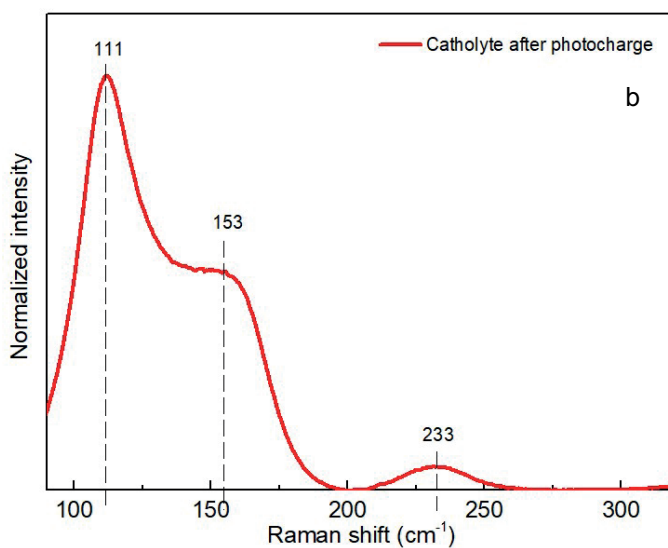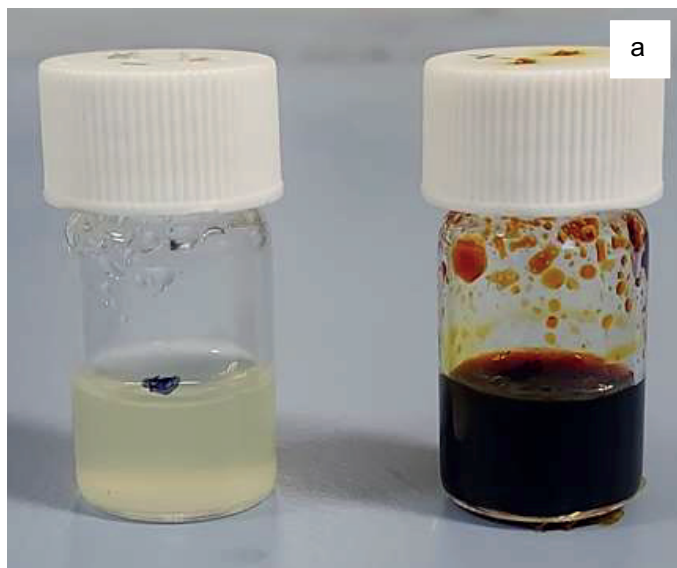
Figure 7.9. Photocharged electrolyte: (a) Raman spectrum of charged catholyte; (b) Optical images of charged anolyte (left) and catholyte (right).

The charge profile and corresponding photocurrent density are shown in **figure 7.8**. The charge was carried out until 21 h of constant illumination. Afterwards, the illumination was stopped and the battery remained at open-circuit conditions until the galvanostatic discharge had started at a current density of 1 mA·cm^{-2}. The charge voltage shows a highly stable plateau within the range of ~1.29 V to 1.31 V, reached the calculated capacity of (~6 Ah·L^{-1}), attained under photocharge, indicating that a SOC of ~ 30% was reached for 21 h of illumination. Apart from the colour change of the catholyte from transparent to dark brown (**figure 7.9a**), the charged state was confirmed by Raman spectroscopy. Raman spectrum of the photocharged catholyte (**figure 7.9b**) confirms the presence of the charged species such as the triiodide (I_3^-) and pentaiodide (I_5^-) and the soluble I_2Cl^- complex at wavenumbers of 111, 153 and 233 cm$^{-1}$ respectively. These assigned peaks are properly matching with the explanation we discussed in **Chapter 5** (**figure 5.9** in **section 5.3.4**).

Interestingly, the photocurrent density exhibits a gradual increment upon illumination. This observation confirms the state of the art organic solar cell consists of PM6:Y6-based photoabsorbers. Based on the literature report,[15] PM6-based polymer donor photoactive blends tend to increase the photocurrent density while decreasing the V_{OC} under constant illumination. The enhancement of the photocurrent is mostly among the donor absorption ranges due to the improvement in hole mobility. This hole mobility enhancement is due to an increase in the polymer donor crystallinity, thus, blend morphology. However, unlike the VRFB chemistry, here, the very `flat´ charge voltage plateau does not correlate with this increasing photocurrent density. Although we might hypothesise that the uprising behaviour of photocurrent with illumination helped the ZIFB to keep increasing the SOC.

To get idea about what happened with the OSC after longer illumination, J-V characteristics was compared before and after photocharge (**figure 7.10**). Despite the degradation of the V_{OC} from 1.51 V to 1.35 V after illumination, the J_{SC} increased from 19 to 21 mA·cm^{-2}.

7
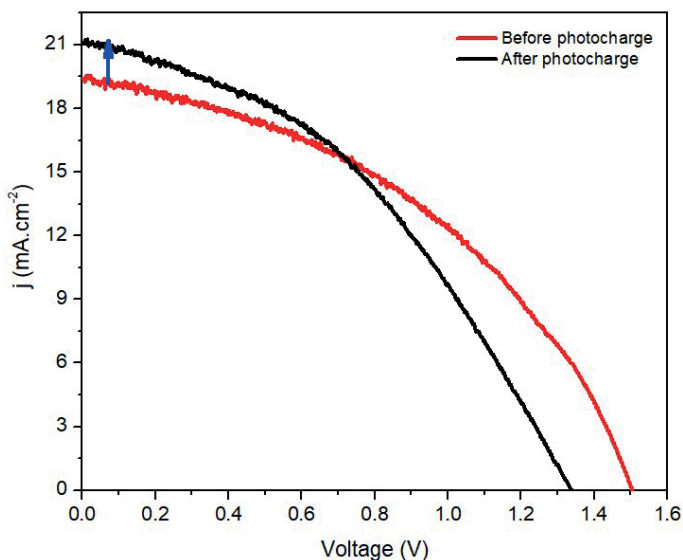
Figure 7.10. P, J-V curves of OSC under 1 sun illumination.

The galvanostatic discharge reflects a clear difference between photocharge and discharge capacities (**figure 7.8b**), resulting in poor coulombic efficiency of 62.8% (**table 7.4**), which could be attributed to the active species crossover as a consequence of operating at a very low current density.[16] Worthwhile, the overall energy efficiency reached a good value of 61% because of an excellent voltage efficiency of 97%. Besides the electrochemical efficiencies, we estimated the solar to charge (η_{STC}) and overall round trip efficiency (η_{RT}), which provides 9.22% and 5.63% respectively.

ZIFB performance evaluation under galvanostatic conditions
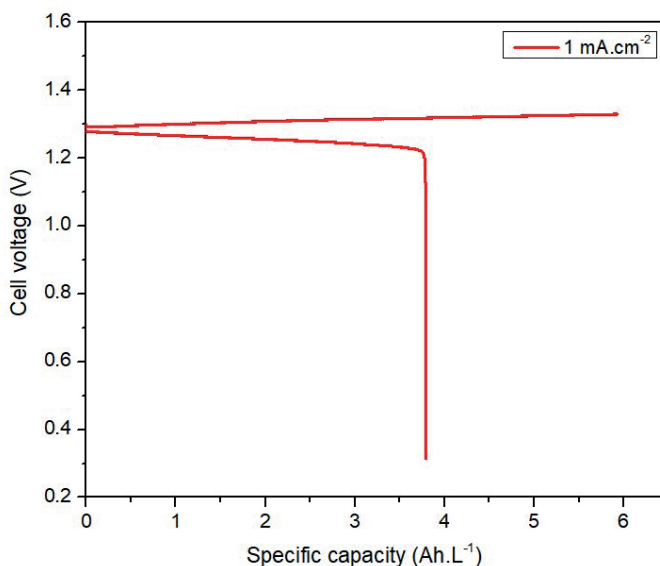
Figure 7.11. Charge-discharge profile of ZIFB under galvanostatic conditions at 1 mA·cm^{-2}.

Table 7.4. Estimated efficiencies values of the OSC coupled ZIFB and comparison with the galvanostatic cycling.

Configuration	Coulombic efficiency (%)	Voltage efficiency (%)	Energy efficiency (%)	η_{STC} (%)	η_{RT} (%)
OSC	62.80	97.20	61.00	9.22	5.63
Galvanostatic @ 1 mA.cm^{-2}	64.00	96.20	61.60	-	-

Furthermore, to compare the electrochemical efficiencies from photocharge and discharge profiles, galvanostatic charge-discharge was performed at a current density of 1 mA·cm^{-2} (**figure 7.11**). Interestingly, the coulombic, voltage and overall energy efficiencies are nearly the same values, which were obtained after photocharge-discharge (**table 7.4**). Coulombic efficiencies are the same within the range of ~63-64%, justifying that most probably crossover is the underlying reason for the capacity fade in discharge. While the enhanced voltage efficiency is mainly because of the low applied current density, which results in lower polarisation resistances.

7.4 Conclusion

The integration of the thin film CIGS mini-module and the optimised ZIFB has been successfully executed. A bias-free charging has achieved up to the maximum SOC, with an excellent discharge capacity. Afterwards, the ZIFB integration with the high-efficiency, organic solar cell (OSC) powers the battery up to ~22% SOC (as of discharge capacity) in bias-free mode, along with promising battery electrical efficiencies. Thanks to the `flat´ nature of the ZIFB charge profile, which dragged then ZIFB to charged solely by solar power despite operating in the region lower than the MPP of the PV.

In summary, this new approach of OSC powered ZIFB has resolved a major issue of operating in a lower and stable voltage of ~1.3 V, and 1.4 – 1.45 V in CIGS coupled ZIFB compared to the CIGS powered VRFB (which reached ~1.7 V, see **Chapter 6**). Despite the successful integration of a cost-optimised solar ZIFB system towards unbiased photocharge without any need of external power source, our approach could only be used as a proof of concept. Several challenges still remain open which should be explored in future research direction of this system. Such as, the small area of the OSC we have used (0.12 cm^2), almost 10 times lower the active area of the ZIFB (geometric area of ZIFB is 1 cm^2), restricted with the low photocurrent. Hence, a longer and unrealistic photocharging time was needed to reach a certain SOC%. This very low operating current density magnified other vital issues such as, possible species crossover between anode and cathode compartments results limited discharge capacity following lower coulombic efficiency. Furthermore, to match the short circuit current (J_{sc}) provided by the OSC, the solar ZIFB cycling were conducted at a lower molar concentration of electrolyte (0.5 M), which limits the battery capacity. Therefore, these open questions should be considered in further research for this kind of photovoltaics system.

On a final note, this very new device-level approach of solar charged ZIFB, using cost-optimised ZIFB redox chemistry as well as an OSC consisting of environment-friendly and highly efficient photoabsorber materials, could enlighten a new path in the research of next generation solar flow battery.

7.5 References

1. S. Dai and X. Zhan, *Adv. Energy Mater.*, **8** (2018).

2. P. Cheng, G. Li, X. Zhan, and Y. Yang, *Nat. Photonics*, **12**, 131–142 (2018).

3. C. Yan, S. Barlow, Z. Wang, H. Yan, A. K-Y. Jen, S. R. Marder and X. Zhan, *Nat. Rev. Mater.*, **3**, 1–19 (2018).

4. G. Zhang, J. Zhao, P. C. Y. Chow, K. Jiang, J. Zhang, Z. Zhu, J. Zhang, F. Huang, and H. Yan, *Chem. Rev.*, **118**, 3447–3507 (2018).

5. J. Yuan, Y. Zhang, L. Zhou, G. Zhang, H-L. Yip, Tsz-K. Lau, X. Lu, C. Zhu, H. Peng, P. A. Johnson, M. Leclerc, Y. Cao, J. Ulanski, Y. Li, and Y. Zou, *Joule*, **3**, 1140–1151 (2019).

6. W. Yang, Z. Luo, R, Sun, J. Guo, T. Wang, Y. Wu, W. Wang, J. Guo, Q. Wu, M. Shi, H. Li, C. Yang, and J. Min, *Nat. Commun.*, **11**, 1–10 (2020).

7. Q. Guo, Q. Guo, Y. Geng, A. Tang, M. Zhang, M. Du, X. Sun and E. Zhou, *Mater. Chem. Front.*, **5**, 3257–3280 (2021).

8. X. Guo, C. Cui, M. Zhang, L. Huo, Y. Huang, J. Hou, and Y. Li, *Energy Environ. Sci.*, **5**, 7943–7949 (2012).

9. Y. Li, *Chem. An Asian J.*, **8**, 2316–2328 (2013).

10. H. W. Luo and Z. T. Liu, *Chinese Chem. Lett.*, **27**, 1283–1292 (2016).

11. J. Liu, S. Chen, D. Qian, B. Gautam, G. Yang, J. Zhao, J. Bergqvist, F. Zhang, W. Ma, H. Ade, O. Inganäs, K. Gundogdu, F. Gao, and H. Yan, *Nat. Energy*, **1**, 1–8 (2016).

12. Y. Q. Pan and G. Y. Sun, *ChemSusChem*, **12**, 4570–4600 (2019).

13. Z. C. Wen, H. Yin, and X. T. Hao, *Surfaces and Interfaces*, **23**, 100921 (2021).

14. Y. Zhao. Z. Wu, X. Liu, Z. Zhong, R. Zhu and J. Yu, *J. Mater. Chem. C*, **9**, 13972–13980 (2021).

15. L. Zhan, S. Li, Tsz-K. Lau, Y. Cui, X. Lu, M. Shi, C-Z. Li, H. Li, J. Hou, and H. Chen, *Energy Environ. Sci.*, **13**, 635–645 (2020).

16. Y. Yao, J. Lei, Y. Shi, F. Ai, and Y. C. Lu, *Nat. Energy*, **6**, 582–588 (2021).

7

7

Chapter 8

Conclusions and future work

8

Conclusions

This thesis is focused on the optimisation of a cost-effective, corrosion-free alternative RFB chemistry, ZIFB, to be integrated with the photovoltaic cells for the development of a next-generation solar flow battery. Thereby, the thesis is divided into two parts. In **Part I (Chapters 3** - **5)**, the electrochemical performance evaluation of ZIFB has been studied and resolved few backlogs related to this redox chemistry. The improvement was mainly done to the anode material and electrolyte solution chemistry. Most of these investigations were conducted at low current densities, to be able for a proper matching between the battery and the photovoltaics. **Part II (Chapters 6** - **7)** has been focused on the device-level approach for the integration of the RFBs with photovoltaics. Thereby, the focus of the research activities were mainly on the optimisation of the SRFB cell design, understanding the most important parameters from both ends, RFBs as well as photovoltaics, such as optimum photobattery operating points: photocurrent and voltage needed for achieving unbiased photocharge. Firstly, the integration between the widely investigated RFB and photovoltaic system, VRFB and CIGS PV, was performed to achieve unbiased photocharging. The idea was to get a preliminary idea of the crucial parameters as well as the challenges of this bias-free approach without the use of any external power source. Finally, this thesis concludes with the integration of the optimised ZIFB (from **Part I**) with the high-efficiency OSC.

The main conclusions and important findings of **Part I**: Electrochemical performance evaluation of ZIFB, are:

- It has been demonstrated that the planar, hydrophilic and highly graphitised graphite foil anode showed best voltage efficiency, lowest internal loss and finally, highest energy efficiency (~80%) for a ZIFB cell due to the efficient Zn metal plating/stripping compared with the use of porous electrodes. Furthermore, the morphology of Zn electrodeposition depends on the several factors, such as physical structure of anodes, electrolyte wetting behaviour and electrical conductivity.

- The cycling results with a Zn foil anode revealed that Zn is a limiting element affecting the cell capacity while having a porous structure is not a requirement for reaching high efficiencies.

- It has been revealed that the reason behind the electrolyte volume imbalances during cycling is the differential ions concentrations between half-cell charged electrolytes dragged the water from the chamber of lower ionic concentration (catholyte) to the higher (anolyte) via the electro-osmotic drag mechanism.

- Balancing the total ions concentrations in both chambers was done by the addition of extra solute (KI) to the catholyte. This proposed model was

validated experimentally by comparing the volume variations of post-charged and post-cycled electrolytes (of both: standard and tuned). 1/3 times of water migration was suppressed with the tuned electrolyte.
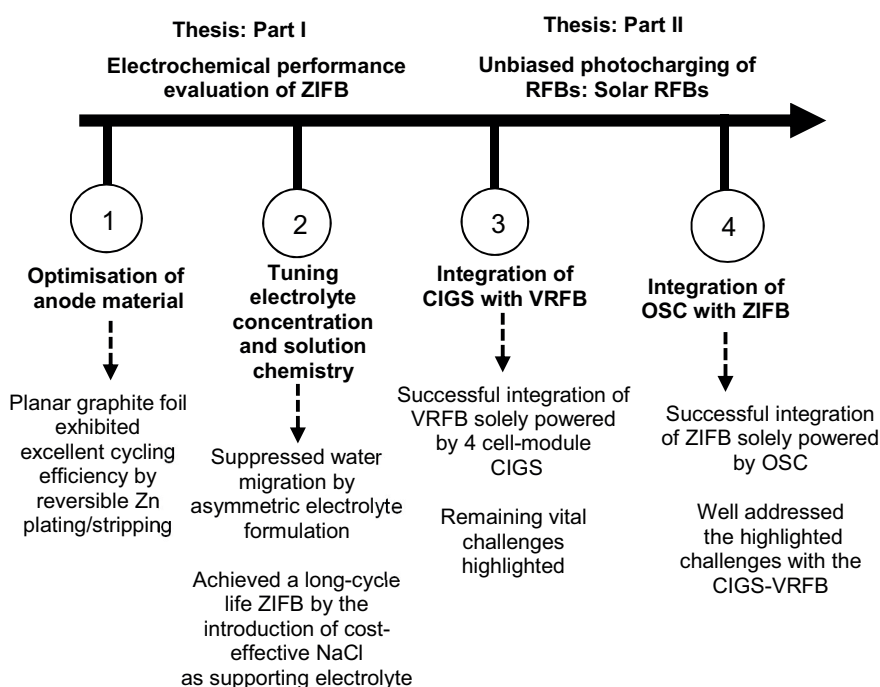
- ICP-OES analysis of water and ions transport mechanism through Nafion 117 showed that solvated K^+ ions were the dominant migrating ion. The addition of extra KI reduced the passage of large solvated Zn^{2+} ions (~50%), reason for a higher portion of water transfer. Finally, this proposed approach of ZIFB cycling with tuned electrolyte showed improved cell electrical conductivity due to the lowest cell ohmic resistance, consequently, better charge-discharge profile.

- To further improve the kinetics, the introduction of a low-cost supporting electrolyte, NaCl, showed the improved redox reversibility of Zn/Zn^{2+} and I_3^-/I^- reactions, which enabled the ZIFB to achieve a stable 100 cycles with 77% of capacity retention, along with a highly reversible Zn plating and stripping (observed from the post-cycled pictures of the anodes).

- SEM and XRD results showed a uniform and densely packed morphology of Zn plating in the presence of Cl^- ions. Coordination interactions between Zn^{2+} and Cl^- ions to the formation of soluble, $ZnCl_4^{2-}$ anions, responsible for stabilisation of Zn^{2+}, hence, improving the Zn/Zn^{2+} redox reaction was confirmed by the chemical equilibrium diagram and Raman spectroscopy.

- On the positive half-cell side, Cl^- ions complexation with solid I_2 as I_2Cl^-, frees up the I^- and blocks solid I_2 precipitation thus enhanced the ZIFB performance with excellent capacity retention. Finally, no volume change of post-100 cycled catholyte was observed, which made our hypothesis about the participation of Na^+ ions as another free migrating ion along with K^+, restricts the mobility of large, solvated Zn^{2+}, thus blocking the water migration from catholyte to anolyte, greatly reflects on the excellent capacity retention throughout the cycling.

The main conclusions and important findings of **Part II.** Unbiased photocharging of redox flow batteries: Solar RFBs, are:

- It was achieved a successful integration of the CIGS PV module with the VRFB. VRFB with 4CM CIGS achieved full battery bias-free photocharge with good battery electrical efficiencies and round-trip energy efficiency of 5%, which is among the highest ones for solar VRFBs.

- A strong correlation between the PV MPP and the VRFB was demonstrated. With 3CM CIGS, full dependence on the battery OCV was observed, leading to excellent performance for the symmetrical V4/V4 configuration and poor efficiency values in a full VRFB.

- Some remaining challenges from this integrated approach were highlighted, such as the necessity of high VRFB cell voltage, the use of critical raw materials in CIGS as well as VRFB. These challenges were attempted to address by the integration of the ZIFB (optimised in **Part I)** with the high-efficiency, OSC. This solar ZIFB was achieved unbiased charge up to 22% SOC.

- Despite this successful coupling of a cost-optimised solar ZIFB for charging in an unbiased mode, there are still several challenges because of what our demonstrated approach could only be used as a proof of concept. These challenges have discussed in the next **section** of **Future work**.

The main achievements of this thesis are shortly summarised below:

Thesis: Part I

Electrochemical performance evaluation of ZIFB

Thesis: Part II

Unbiased photocharging of RFBs: Solar RFBs

1

Optimisation of anode material

Planar graphite foil exhibited excellent cycling efficiency by reversible Zn plating/stripping

2

Tuning electrolyte concentration and solution chemistry

Suppressed water migration by asymmetric electrolyte formulation

Achieved a long-cycle life ZIFB by the introduction of cost-effective NaCl as supporting electrolyte

3

Integration of CIGS with VRFB

Successful integration of VRFB solely powered by 4 cell-module CIGS

Remaining vital challenges highlighted

4

Integration of OSC with ZIFB

Successful integration of ZIFB solely powered by OSC

Well addressed the highlighted challenges with the CIGS-VRFB

Figure 8.1. Thesis roadmap and main achievements.

8

Future work

Based on the work done in this thesis, there are further remaining investigations to be done and challenges to overcome for boosting the ZIFB performance:

- An in-depth understanding of porous anode materials, such as core engineering on the anode, and tuning the wettability could facilitate reversible Zn plating/stripping.

- Exploration of the cathode materials with the electrocatalytic approach for the improvement of the kinetics and reversibility of I_3^-/I^- redox reactions.

- Exploration of the membrane material, from the standard Nafion to other low-cost polymer materials to decrease the ohmic losses and species crossover, without compromising the high selectivity and mechanical stability.

- In the OSC-ZIFB integration demonstrated in this thesis, a few remaining challenges should be addressed before utilising its full potential. Such as, the lower photocurrent could be overcome by coupling with an OSC of a larger photoactive area, thus matching the charging time with the practical duration of the sunlight. Working with a larger PV area could resolve the species crossover issue associated to low current operation, as well as enable the higher electrolyte molar concentrations, to enhance the battery capacity.

On a final note, this optimised ZIFB showed promising performance, which, after carefully addressing the above-mentioned recommendations, could enlighten a new path in the future research of next-generation solar flow batteries.

8

Curriculum vitae

Monalisa Chakraborty

Personal information

Date of birth: 21.02.1990
Nationality: Indian
Email: chakraborty.mona@gmail.com
          mchakraborty@irec.cat
ORCID: 0000-0001-5268-9733
Web of Science Researcher ID: A-2539-2019

Education

2018 – present	**Doctorate in Material Science** Thesis: Zinc-iodide redox flow battery for next generation of solar energy storage Autonomous University of Barcelona (UAB) Barcelona, Spain
2014 – 2017	**Master of Science in Energy Science and Technology** Ulm University Thesis: Cathode/Electrolyte Interphase on $LiNi_{0.5}Mn_{1.5}O_4$ studied by *in situ* Attenuated total-reflectance Fourier transform infrared spectroscopy (ATR-FTIRS) Ulm, Germany Grade: 1.5 – Summa cum laude, Excellent
2007 – 2011	**Bachelor of Engineering in Applied Electronics & Instrumentation** University of Burdwan Burdwan, India Grade: 81.6% - First Class Honours

Professional experience in Academics

2018 – present	**Pre-Doctoral researcher** Catalonia Institute for Energy Research (IREC) Barcelona, Spain

02/2017–09/2017	**Student research assistant**
	Ulm University
	Ulm, Germany

06/2016 – 08/2016	**Laboratory Tutor**
	Ulm University
	Ulm, Germany

01/2016 – 07/2016	**Student research assistant**
	Helmholtz Institute Ulm
	Ulm, Germany

Internships

2021	**Visiting PhD student**
	ICFO (Institut de Ciències Fotòniques)
	Castelldefels, Spain

2010	**Intern student**
	ESBI Electronics Pvt. Ltd., Kolkata, India
	Kolkata, India

2009	**Intern student**
	Durgapur Projects Limited
	Durgapur, India

Awards and scholarships

| 2019 | Graduate Student Award in EMRS Fall Meeting Warshaw, Poland |

| 2018 | Marie Skłodowska-Curie Early Stage Researcher Grant under the framework of DOC-FAM H2020-MSCA-COFUND-2016, to carry out full-time doctoral research in Barcelona, Spain |

| 2017 | Master scholarship for completing the master thesis, from DAAD (German Academic Exchange Service; Ulm University, Germany |

2015	Master scholarship from the DAAD (German Academic Exchange Service) within the "Scholarship and Support Program for International Students" (STIBET) Ulm University, Germany
2011	First class with Honours in Bachelor of Engineering University of Burdwan, Burdwan, India
2005	First class with Distinction in Secondary State Board Examination West Bengal, India

Publications from PhD thesis

M. Chakraborty, T. Andreu, B. Molinari, J. R. Morante and S. Murcia-López, Suppressing water migration in aqueous Zn-Iodide flow batteries by asymmetric electrolyte formulation, Electrochimica Acta, submitted (in review).

M. Chakraborty, T. Andreu, M. Guc, M. Amazian and S. Murcia-López, A long cycle life zinc-iodide flow battery enabled by a multifunctional low cost supporting electrolyte, Journal of Power Sources, submitted (in review).

M. Chakraborty, S. Murcia-López, J. R. Morante and T. Andreu, Structural Influence of the Anode Materials towards Efficient Zn Deposition/Dissolution in Aqueous Zn-Iodide Flow Batteries, Journal of The Electrochemical Society, **2021**, 168, 040532.

S. Murcia-López, **M. Chakraborty**, N. M. Carretero, C. Flox, J. R. Morante, and T. Andreu, Adaptation of $Cu(In,Ga)Se_2$ photovoltaics for full unbiased photocharge of integrated solar vanadium redox flow batteries, Sustainable Energy Fuels, **2020**, 4, 1135-1142.

Other publication

Weber, B. Wang, C. Bodirsky, **M. Chakraborty**, M. Wachtler, T. Diemant, J. Schnaidt, and R. J. Behm, Model Studies on Solid Electrolyte Interphase Formation on Graphite Electrodes in Ethylene Carbonate and Dimethyl Carbonate II: Graphite Powder Electrodes, ChemElectroChem **2020**, 7, 4794–4809.

Conferences *(Contributed talks)*

M. Chakraborty, T. Andreu, M. Guc, J.R. Morante, S. Murcia-López, A long cycle life zinc-iodide flow battery enabled by a low-cost supporting electrolyte, EMRS Virtual Spring Meeting 2022, 30th May - 3rd June.

M. Chakraborty, S. Murcia-López, J.R. Morante, T. Andreu, Strategical tuning of electrolyte design for achieving a highly efficient aqueous zinc-iodide flow battery, EMRS Virtual Fall Meeting 2021, 20th - 23rd September

M. Chakraborty, S. Murcia-López, J.R. Morante, T. Andreu, Design optimization of low cost, highly efficient aqueous zinc-iodide flow battery, 72nd Annual Meeting of the International Society of Electrochemistry 2021, 29th August - 3rd September, Jeju Island, Korea (presented online).

M. Chakraborty, S. Murcia-López, J.R. Morante, T. Andreu, Design optimization of low cost, highly efficient aqueous zinc-iodide flow battery, 2021 Virtual MRS Spring Meeting & Exhibit, 17th - 23rd April (presented online).

M. Chakraborty, S. Murcia-López, J.R. Morante, T. Andreu, Facing water migration issues in aqueous zinc-iodide flow batteries, Online nanoGe Fall meeting 2020, 20th - 23rd October.

M. Chakraborty, Redox flow batteries - promising choice for stationary energy storage, Vermú de nanociencia 2020, Spain, 6th May (presented online).

M. Chakraborty, B. Molinari, S. Murcia-López, J.R. Morante, T. Andreu, Design optimization of low cost, highly efficient aqueous zinc-iodide flow battery, EMRS Fall Meeting 2019, 16th - 19th September, Warshaw, Poland.

M. Chakraborty, B. Molinari, S. Murcia-López, J.R. Morante, T. Andreu, Design optimization of low cost, highly efficient aqueous zinc-iodide flow battery, HYCELTEC 2019, 1st - 3rd July, University of Barcelona, Spain.

Weber, I, J. Schnaidt, **M. Chakraborty**, T. Diemant, R. J. Behm, Spectro-electrochemical Model Studies on Electrolyte decomposition at the Anode|Electrolyte Interphase of Li ion batteries, DIPC School 2017, Photoelectrocatalysis at the Atomic scale, 27th - 30th June, Donostia-San Sebastian, Spain.

Co-Supervision of Master Thesis

Master thesis in ¨Enhancements of electrolytes in vanadium redox flow batteries¨ University of Barcelona, Barcelona (2022).